Spider GAN: Leveraging Friendly Neighbors to Accelerate GAN Training
Supporting Document

Siddarth Asokan
Robert Bosch Center for Cyber-Physical Systems
Indian Institute of Science
Bengaluru - 50012, India
siddartha@iisc.ac.in

Chandra Sekhar Seelamantula
Department of Electrical Engineering
Indian Institute of Science
Bengaluru - 50012, India
css@iisc.ac.in

Part I
Appendix

Table of Contents

Overview of the Supplementary Material

The Supplementary Material comprises this *Supporting Document* of appendices, the source codes of this project, consisting of the implementations of various Spider GAN variants and SID metric, and animations corresponding to (a) Evaluating the signed distance on Gaussain data; and (ii) Interpolation in the input, and intermediate stages of Spider StyleGAN. The appendices contains the additional discussions on identifying the friendly neighborhood in Spider GANs, ablation studies on SID, implementation details, and additional experiments on the Spider GAN variants considered in the *Main Manuscript*. The citations to prior art in the *Supporting Document* are with respect to the references listed herein.

A. Baselines for Identifying the Friendly Neighborhood

Approaches that compute the intrinsic dimensionality $n_{\mathfrak{D}}$ of a dataset are either computationally intensive [1] or do not scale with sample size [2, 3]. Campadelli *et al.* [4] presented a survey of various nearest-neighbor and maximum-likelihood estimators of $n_{\mathfrak{D}}$ for low-dimensional datasets. A well-known approach for computing $n_{\mathfrak{D}}$ is provided in the Davis-Kahan $\sin\Theta$ theorem [5], which provides an upper bound on the distance between two subspaces in terms of the eigen-gap between them. A practically implementable version [6] is based on the sample covariance matrix of the two datasets and their eigenvalues. Along a parallel vertical, multiple works have derived convergence guarantees on the GAN training algorithms, given $n_{\mathfrak{D}}$ [7, 8, 9]. We now discuss the Davis-Kahan $\sin\Theta$ theorem, and compare its performance against the FID, KID and CSID$_m$ approaches in terms of the friendliest neighbors picked by them.

A.1. The Davis-Kahan Theorem

The Davis-Kahan $\sin\Theta$ Theorem [5] upper-bounds the distance between subspaces in terms of the eigen-gap between them. Let $\Sigma_p, \Sigma_q \in \mathbb{R}^{n\times n}$ denote the sample covariance matrices of two datasets $\mathfrak{D}_p$ and $\mathfrak{D}_q$, respectively, with $\lambda_{1_p} \geq \lambda_{2_p} \geq \cdots \geq \lambda_{n_p}$ and $\lambda_{1_q} \geq \lambda_{2_q} \geq \cdots \geq \lambda_{n_q}$ denoting their respective eigenvalues in order. Consider $1 \leq r \leq s \leq n$, and define $d := s - r + 1$, $\lambda_0 := \infty$ and $\lambda_{n+1} := -\infty$. Consider the subspaces $\mathcal{V}_p = \text{span}\left\{v_r^p, v_{r+1}^p, \ldots, v_s^p\right\}$ and $\mathcal{V}_q = \text{span}\left\{v_r^q, v_{r+1}^q, \ldots, v_s^q\right\}$ that are spanned by the eigenvectors of Σ_p and Σ_q, respectively. The Davis-Kahan $\sin\Theta$ theorem bounds the distance between the two subspaces $\mathcal{V}_p$ and $\mathcal{V}_q$ as follows:

$$\|\sin\Theta(\mathcal{V}_p, \mathcal{V}_q)\|_{\text{F}} \leq \frac{\|\Sigma_p - \Sigma_q\|_{\text{F}}}{\delta}, \qquad (1)$$
$$\text{where } \delta = \inf\left\{|\hat{\lambda} - \lambda| : \lambda \in [\lambda_s^q, \lambda_r^q], \hat{\lambda} \in \left(-\infty, \hat{\lambda}_{s-1}^p\right] \bigcup \left[\hat{\lambda}_{r+1}^p, \infty\right)\right\}.$$

As noted by Yu *et al.* [6], evaluating the infimum among all pairs of eigenvalues requires a huge computational overhead, particularly on high-dimensional data. They derived a loose, but computationally efficient upper bound:

$$\|\sin\Theta(\mathcal{V}_p, \mathcal{V}_q))\|_{\text{F}} \leq \frac{2\min\left\{d^{\frac{1}{2}}\|\Sigma_p - \Sigma_q\|_{op}, \|\Sigma_p - \Sigma_q\|_{\text{F}}\right\}}{\min\left\{\lambda_{r-1}^q - \lambda_r^q, \lambda_s^q - \lambda_{s+1}^q\right\}}, \qquad (2)$$

where $\|\cdot\|_{op}$ and $\|\cdot\|_{\text{F}}$ denote the operator and Frobenius norms, respectively. For large n, the operator norm can be approximated by the ℓ_∞ norm of the difference between the eigenvalues of Σ_p and Σ_q [6]. The form of the $\sin\Theta$ distance in Equation (2) replaces the infimum amongst all pairs with the minimum between only two pairs of eigenvalues, which requires less computation.

We now discuss a variant of the $\sin\Theta$ distance between the subspaces spanned by two datasets. Since the intrinsic dimensionality of the data is not known priori, we compute the $\sin\Theta$ distance for various choices of r and s, and pick the *best* amongst them, which we call the $\min\sin\Theta$ distance.

The* $\min\sin\Theta$ *Distance: Consider the space spanned by the (vectorized) images in the datasets. Since the pixel resolution of the images across datasets is not the same, it is appropriate to first rescale them to the same dimension, for instance, using bilinear interpolation. Depending on whether the rescaled image dimension is greater or smaller than the image dimension, there is a trade-off between the image quality (superior at higher resolution) and computational efficiency (superior at lower resolution). We found out experimentally that resizing all images to $32 \times 32 \times 3$ is a viable compromise. We consider $r = 1$ and compute the $\sin\Theta(\mathcal{V}_p, \mathcal{V}_q; s)$, for $s = 3, 4, \ldots \lceil n/10 \rceil$, where $n = 3072 = 32 \times 32 \times 3$. The friendly neighborhood as indicated by the $\min\sin\Theta$ distance is $\min_s\{\sin\Theta(\mathcal{V}_p, \mathcal{V}_q; s)\}$. In other words, the closest source dataset given all s is deemed the friendliest neighbor of the target.

A.2. Comparison of Approaches for Identifying the Friendly Neighborhood

We compare the $\min \sin \Theta$, FID, KID and CSID$_m$ distances in terms of the friendliest neighbor predicted by these methods. FID, KID and CSID$_m$ distances have been defined in Section 3 of the *Main Manuscript*. Table 1 shows the $\min \sin \Theta$ distance for the various datasets considered in Section 3 of the Main Manuscript. We also present KID between the various datasets in Table 3 of this document. Tables 2 and 4 present the remaining combinations between datasets left out from the *Main Manuscript*. The **first**, **second** and **third** *friendly neighbors* are color-coded for quick and easy identification. We observe across all datasets that, FID and KID are highly correlated in terms of the friendly neighbors they identify for a given target. CSID$_m$ is also in agreement with the observations when the target is more diverse, but in scenarios such as TinyImageNet or CIFAR-10, it is able to indicate the less diverse sources as a poor input choice. The experiments on learning Tiny-ImageNet within the Spider GAN framework in Appendix D.2 are more in agreement with the friendly neighbors identified by CSID$_m$.

Across all distances, we observe that the results obtained on MNIST or Fashion-MNIST as the source do not correlate well with the experimental results (cf. Appendix D.2). This is attributed to the limitation of the Inception-Net embedding in handling grayscale images. Inception-Net operates on color images and offers limited performance on grayscale images.

Table 1 shows that the $\min \sin \Theta$ distance is unable to identify the friendliest neighbor accurately and consistently. For instance, the ordering of the top three neighbors on MNIST, CelebA or LSUN-Churches identified by using the $\min \sin \Theta$ distance is not consistent with the ordering suggested by CSID$_m$ and that verified experimentally. However, on the other datasets, $\min \sin \Theta$ is worse than the InceptionNet approaches for identifying the friendliest neighborhood.

Table 1. The best-case $\min \sin \Theta(\cdot)$ distance between the spaces spanned by the eigenvectors of the source and target datasets. The rows represent the sources and the columns correspond to the target datasets. The **first**, **second** and **third** *friendly neighbors* (color coded) of the target is the source with the three lowest $\min \sin \Theta(\cdot)$ values is that column. We observe that the *friendliest neighbor* identified by the $\min \sin \Theta$ distance are generally not in agreement with those identified by FID, KID or CSID$_m$.

Src \ Tar	MNIST	F-MNIST	SVHN	CIFAR-10	T-ImgNet	CelebA	Ukiyo-E	Church
MNIST	0	60.74	63.25	85.73	43.19	27.43	23.79	35.35
F-MNIST	96.68	0	69.01	110.7	53.77	36.69	45.02	48.29
SVHN	79.91	**54.77**	0	57.99	23.62	19.86	25.95	29.55
CIFAR-10	72.16	58.56	**35.97**	0	**7.521**	**14.63**	21.16	**15.89**
T-ImgNet	**70.86**	**55.43**	**30.67**	**14.67**	0	**13.97**	**20.05**	**15.52**
CelebA	72.13	60.62	**41.35**	**45.74**	**22.39**	0	**19.16**	23.48
Ukiyo-E	**54.09**	59.30	43.08	52.75	25.65	**15.29**	0	**22.50**
Church	**66.54**	**57.11**	44.02	**35.55**	**17.81**	16.80	**20.19**	0

Table 2. A comparison of FID between popular training datasets. The rows correspond to the source (Src) and the columns correspond to the target (Tar). The **first**, **second** and **third** *friendly neighbors* (color coded) of the target are the sources with the three lowest FID values. FID fails to detect scenarios where the source possesses lower sample diverse that the target, as in the case of CIFAR-10 and LSUN-Church sources in comparison to the Tiny-ImageNet target.

Tar Src	MNIST	F-MNIST	SVHN	CIFAR-10	T-ImgNet	CelebA	Ukiyo-E	Church
MNIST	1.2491	**175.739**	234.850	258.246	264.250	360.622	398.280	357.428
F-MNIST	**176.813**	2.4936	212.619	188.367	197.057	365.222	387.049	345.011
SVHN	**236.707**	214.262	3.4766	**168.615**	**189.133**	357.193	372.444	356.148
CIFAR-10	**259.045**	**188.710**	**168.113**	5.0724	**64.3941**	305.528	303.694	**256.207**
T-ImgNet	264.309	**197.918**	**188.823**	**64.0312**	6.4845	**251.198**	**257.078**	**203.899**
CelebA	360.773	364.586	357.383	303.490	250.735	2.5846	**301.108**	**265.954**
Ukiyo-E	396.791	387.088	372.557	300.511	254.102	**300.259**	5.9137	267.624
Church	350.708	343.781	**354.885**	**254.991**	**204.162**	**266.508**	**267.638**	2.5085

Table 3. KID between popular training datasets. The **first**, **second** and **third** *friendly neighbors* (color coded) of the target (column) are the sources (rows) with the three lowest KID values. We observe that, akin to FID, the KID measure is also unable to compare the leave diversity between the source and target datasets, as is the case between Tiny-ImageNet and CIFAR-10.

Tar Src	MNIST	F-MNIST	SVHN	CIFAR-10	T-ImgNet	CelebA	Ukiyo-E	Church
MNIST	2×10^{-6}	**0.1587**	0.2428	0.2380	0.2393	0.4284	0.5082	0.4376
F-MNIST	**0.1606**	1×10^{-6}	0.1922	0.1353	0.1578	0.4291	0.4751	0.3963
SVHN	0.2458	0.1943	2×10^{-7}	**0.1377**	**0.1674**	0.4059	0.4393	0.3962
CIFAR-10	**0.2404**	**0.1357**	**0.1377**	6×10^{-6}	**0.0334**	**0.3205**	**0.3229**	**0.2453**
T-ImgNet	**0.2397**	**0.1579**	**0.1667**	**0.0321**	8×10^{-6}	**0.2403**	**0.2595**	**0.1692**
CelebA	0.4388	0.4265	0.4054	0.3165	0.2406	7×10^{-6}	0.3620	**0.2856**
Ukiyo-E	0.5064	0.4746	0.4408	0.3183	0.2568	0.3610	2×10^{-5}	0.3022
Church	0.4379	0.3916	**0.3932**	**0.2408**	**0.1695**	**0.2857**	**0.3019**	3×10^{-5}

Table 4. A comparison of CSID$_m$ between popular training datasets for $m = \lfloor \frac{n}{2} \rfloor$. The rows represent the source (Src) and the columns represent to the target (Tar). The **first**, **second** and **third** *friendly neighbors* (color coded) of the target are the sources with the three lowest positive CSID$_m$ values, respectively. CSID$_m$ is superior to FID or KID, as it assigns negative values to source datasets that are less diverse than the target.

Tar Src	MNIST	F-MNIST	SVHN	CIFAR-10	T-ImgNet	CelebA	Ukiyo-E	Church
MNIST	0.1865	**21.886**	37.227	29.298	9.436	198.714	201.550	205.322
F-MNIST	**162.962**	0.1097	46.938	19.051	-0.5571	167.840	191.010	181.458
SVHN	**212.473**	77.357	-0.0566	**34.534**	**21.668**	195.631	214.507	219.790
CIFAR-10	221.337	**65.426**	**52.051**	-0.1478	-7.109	**180.491**	198.991	**173.655**
T-ImgNet	230.916	75.737	**67.902**	**12.892**	0.6743	**157.520**	**197.447**	**184.977**
CelebA	**204.794**	68.828	65.299	**23.685**	**8.829**	0.6241	**184.170**	191.927
Ukiyo-E	250.226	92.741	82.157	39.792	**18.727**	191.930	0.5494	**180.697**
Church	212.452	**48.676**	**56.136**	-4.655	-23.115	**185.740**	**198.750**	-0.5258

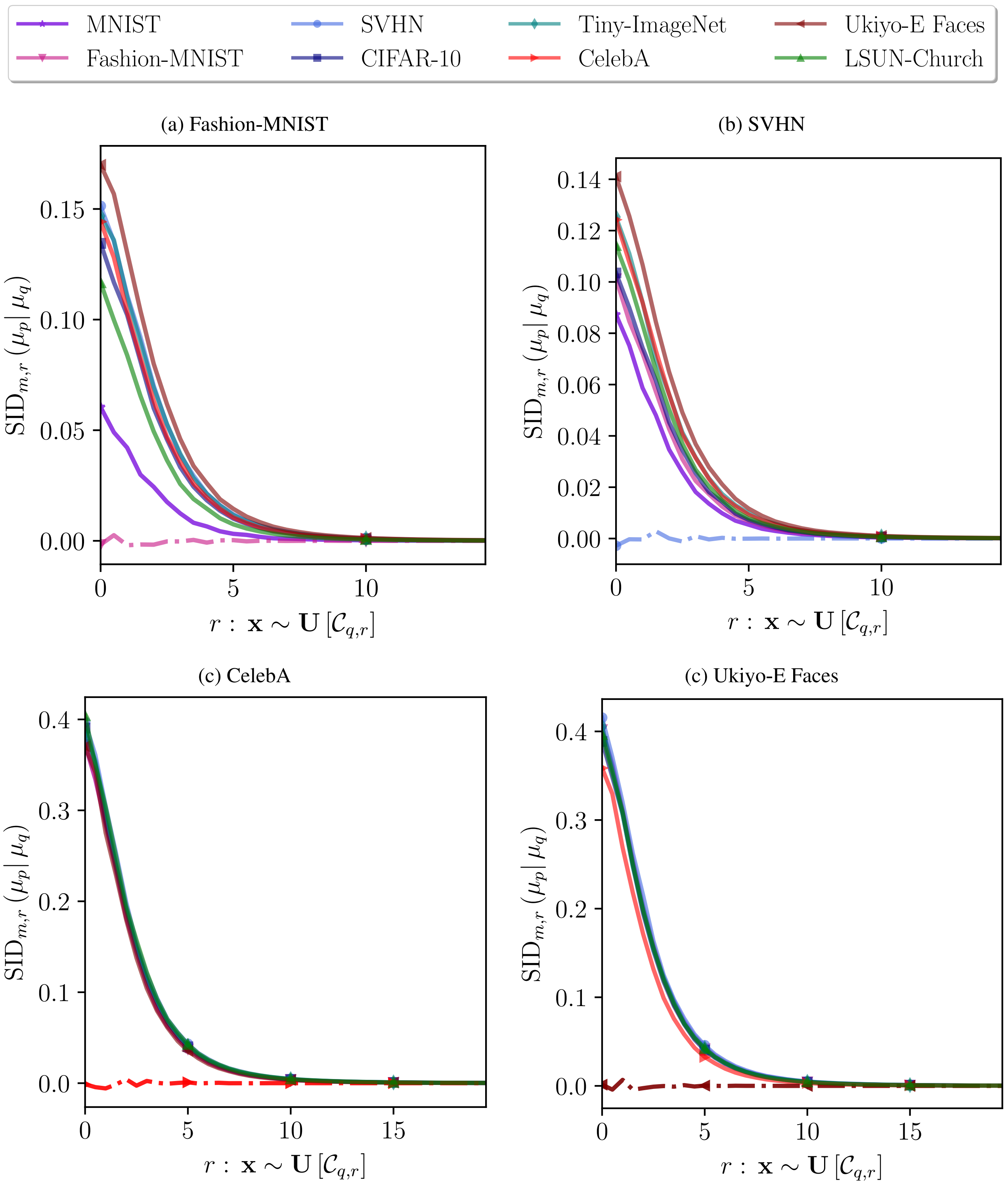

Figure 1. $\mathrm{SID}_{m,r}$ as a function of the hyper-cube length r. We observe that MNIST is the closest neighbor to both Fashion-MNIST and SVHN, while CelebA is marginally closer to Ukiyo-E than the other baselines considered. In scenarios such as case when the target is CelebA or Ukiyo-E Faces, the SID curve alone cannot be used to conclude the *friendliest neighbor* of a target dataset, and the area under the curve, CSID_m is more informative (cf. Table 4) .

B. The Signed Inception Distance (SID)

In this appendix, we derive a favorable theoretical guarantee of the SID metric, discuss the algorithm for the computation of SID with relevant ablation experiments on synthetic Gaussian and image datasets.

B.1. Asymptotic Behavior of the Signed Distance

Without loss of generality, consider the *signed distance* presented in Equation (2) of the *Main Manuscript*:

$$\mathrm{SD}_{m,r}(\mu_p\|\mu_q) = \frac{1}{M_{\boldsymbol{x}}}\sum_{\substack{\ell=1\\ \tilde{\boldsymbol{x}}_\ell\in\mathcal{C}_{q,r}}}^{M_{\boldsymbol{x}}}\left\{\frac{1}{N_q}\sum_{\substack{j=1\\ \boldsymbol{c}_j\sim\mu_q}}^{N_q}\Phi(\boldsymbol{x}_\ell,\boldsymbol{c}_j) - \frac{1}{N_p}\sum_{\substack{i=1\\ \tilde{\boldsymbol{c}}_i\sim\mu_p}}^{N_p}\Phi(\boldsymbol{x}_\ell,\tilde{\boldsymbol{c}}_i)\right\}.$$

Asymptotically, when infinite samples are drawn from the test space, $\mathcal{C}_{q,r}$, we get

$$\begin{aligned}\mathrm{SD}_{m,r}(\mu_p\|\mu_q) &= \lim_{M_{\boldsymbol{x}}\to\infty}\left\{\frac{1}{M_{\boldsymbol{x}}}\sum_{\substack{\ell=1\\ \tilde{\boldsymbol{x}}_\ell\in\mathcal{C}_{q,r}}}^{M_{\boldsymbol{x}}}\left\{\frac{1}{N_q}\sum_{\substack{j=1\\ \boldsymbol{c}_j\sim\mu_q}}^{N_q}\Phi(\boldsymbol{x}_\ell,\boldsymbol{c}_j) - \frac{1}{N_p}\sum_{\substack{i=1\\ \tilde{\boldsymbol{c}}_i\sim\mu_p}}^{N_p}\Phi(\boldsymbol{x}_\ell,\tilde{\boldsymbol{c}}_i)\right\}\right\}.\\ &= \kappa\int_{\boldsymbol{x}\in\mathcal{C}_{q,r}}\left\{\frac{1}{N_q}\sum_{\substack{j=1\\ \boldsymbol{c}_j\sim\mu_q}}^{N_q}\Phi(\boldsymbol{x},\boldsymbol{c}_j) - \frac{1}{N_p}\sum_{\substack{i=1\\ \tilde{\boldsymbol{c}}_i\sim\mu_p}}^{N_p}\Phi(\boldsymbol{x},\tilde{\boldsymbol{c}}_i)\right\}\mathrm{d}\boldsymbol{x},\end{aligned}$$

for some positive constant κ. Similarly, when the number of centers drawn from μ_p and μ_q tends to infinity, the inner summations can be replaced with their corresponding expectations, resulting in

$$\begin{aligned}\mathrm{SD}_{m,r}(\mu_p\|\mu_q) &= \kappa\int_{\boldsymbol{x}\in\mathcal{C}_{q,r}}\lim_{N_q\to\infty}\left\{\frac{1}{N_q}\sum_{\substack{j=1\\ \boldsymbol{c}_j\sim\mu_q}}^{N_q}\Phi(\boldsymbol{x},\boldsymbol{c}_j)\right\} - \lim_{N_p\to\infty}\left\{\frac{1}{N_p}\sum_{\substack{i=1\\ \tilde{\boldsymbol{c}}_i\sim\mu_p}}^{N_p}\Phi(\boldsymbol{x},\tilde{\boldsymbol{c}}_i)\right\}\mathrm{d}\boldsymbol{x}.\\ &= \kappa'\int_{\boldsymbol{x}\in\mathcal{C}_{q,r}}\left(\int_{\boldsymbol{y}}\Phi(\boldsymbol{x},\boldsymbol{y})\mu_q(\boldsymbol{y})\,\mathrm{d}\boldsymbol{y} - \int_{\boldsymbol{y}}\Phi(\boldsymbol{x},\boldsymbol{y})\mu_p(\boldsymbol{y})\,\mathrm{d}\boldsymbol{y}\right)\mathrm{d}\boldsymbol{x}.\\ &= \kappa'\int_{\boldsymbol{x}\in\mathcal{C}_{q,r}}\left(\mathbb{E}_{\boldsymbol{y}\sim\mu_q}\left[\Phi(\boldsymbol{x},\boldsymbol{y})\right] - \mathbb{E}_{\boldsymbol{y}\sim\mu_p}\left[\Phi(\boldsymbol{x},\boldsymbol{y})\right]\right)\mathrm{d}\boldsymbol{x}.\end{aligned}$$

Recall that the samples $\boldsymbol{x}_\ell$ are drawn uniformly at random from $\mathcal{C}_{q,r}$ (cf. Section 3.1 of the *Main Manuscript*). This allows us to replace the outer integral with another expectation, resulting in

$$\mathrm{SD}_{m,r}(\mu_p\|\mu_q) = \mathbb{E}_{\boldsymbol{x}\sim\mathcal{C}q,r,\boldsymbol{y}\sim\mu_q}\left[\Phi(\boldsymbol{x},\boldsymbol{y})\right] - \mathbb{E}_{\boldsymbol{x}\sim\mathcal{C}q,r,\boldsymbol{y}\sim\mu_p}\left[\Phi(\boldsymbol{x},\boldsymbol{y})\right].$$

The above result links the SD to kernel statistics and provides the asymptotic guarantee that when the two distributions μ_p and μ_q coincide, *i.e.*, $\mu_p = \mu_q$, and therefore, $\mathrm{SD}_{m,r}(\mu_p\|\mu_p) := 0$.

B.2. SID Computation

The procedure to compute the signed distance between the samples drawn from two distributions is given in Algorithm 1. While the algorithm is easily implementable for low-dimensional data, an extension to practical settings with images necessitates computing Inception embeddings over batches of samples. The signed distance (SD) computed over Inception embeddings is called SID. To extend the SID computation algorithm for evaluating GANs, we consider $\mathfrak{D}_q$, the target dataset, and $\mathfrak{D}_p$, samples drawn from the generator. We set $|\mathfrak{D}_q| = |\mathfrak{D}_p| = 5000$. For each r, we average $\mathrm{SID}_{m,r}$ over batches of size $N_B = 100$. This allows for efficient computation of the Inception features for high-resolution images. Algorithm 2 presents this modified approach for evaluating GANs with SID. We implement the SID computation atop the publicly available Clean-FID [10] library. Similar to the Clean-FID framework, SID can be computed between any two image folders using the Clean-FID backend. As a result, the InceptionV3 mapping and resizing functions are consistent with the existing Clean-FID approach. Details regarding the public release of the Python + TensorFlow/PyTorch library for SID computation are discussed in Appendix E of this document.

Algorithm 1: Signed distance (SD) between two distributions

```
Input: Source data $\mathfrak{D}_p = \{\tilde{\boldsymbol{c}}_i \mid i = 1, 2, 3, \ldots, N_p;\ \tilde{\boldsymbol{c}}_i \sim \mu_p\}$, kernel order $m$, dimensionality $n$,
       Target data $\mathfrak{D}_q = \{\boldsymbol{c}_j \mid j = 1, 2, 3, \ldots, N_q;\ \boldsymbol{c}_j \sim \mu_q\}$, max radius $r_{\max}$, step size $\eta$,
       batch size $M_{\boldsymbol{x}}$
Compute: $\mu_q = \text{mean}\,(\boldsymbol{c}_j \sim \mathfrak{D}_q)\,; \Sigma_q = \text{covariance}\,(\boldsymbol{c}_j \sim \mathfrak{D}_q)$
for $k = 0, 1, 2, \ldots r_{\max}$ do
    Compute: Hypercube length $r = \eta \times k \times \max(\text{diag}(\Sigma_q))$
    Define: Hypercube $\mathcal{C}_{q,r}$: Center = $\mu_q$
    Sample: $\boldsymbol{x}_\ell \sim \text{Uniform}\,[\mathcal{C}_{q,r}]\,;\ \ell = 1, 2, 3, \ldots, M_{\boldsymbol{x}}$
    Compute: $\text{SD}_{m,r}(\mu_p \| \mu_q)$ based on Equation (2) of the Main Manuscript
Output: Plot of $\text{SD}_{m,r}$ versus $r$
```

Algorithm 2: Signed inception distance (SID) between the generator output and target data

```
Input: Target data $\mathfrak{D}_q = \{\boldsymbol{c}_j \mid j = 1, 2, \ldots, N_q;\ \boldsymbol{c}_j \sim \mu_q\}$, kernel order $m$, dimensionality $n$,
       max radius $r_{\max}$, step size $\eta$, hypercube sample batch size $M_{\boldsymbol{x}}$, Generator G,
       Generator batch size $N_B$, Inception model $\psi$.
Compute: $\mu_q = \text{mean}\,(\boldsymbol{c}_j \sim \mathfrak{D}_q)\,; \Sigma_q = \text{covariance}\,(\boldsymbol{c}_j \sim \mathfrak{D}_q)$
for $k = 0, 1, 2, \ldots r_{\max}$ do
    for Batches $i = 1, 2, \ldots \frac{N_q}{N_B}$ do
        Sample: $\boldsymbol{z}_\ell \sim p_Z(\boldsymbol{z});\ \ell = 1, 2, 3, \ldots, N_B$ – Generator inputs
        Sample: $\tilde{\boldsymbol{c}}_\ell \sim G(\boldsymbol{z});\ \ell = 1, 2, 3, \ldots, N_B$ – Generator outputs
        Sample: $\boldsymbol{c}_j \sim \mathfrak{D}_q;\ \ell = 1, 2, 3, \ldots, N_B$ – Target data samples
        Compute: $\psi(\tilde{\boldsymbol{c}}_\ell)$ and $\psi(\boldsymbol{c}_j)$ – Inception embeddings of generator output and target data.
        Compute: Hypercube length $r = \eta \times k \times \max(\text{diag}(\Sigma_q))$
        Define: Hypercube $\mathcal{C}_{q,r}$: Center = $\mu_q$
        Sample: $\boldsymbol{x}_\ell \sim \text{Uniform}\,[\mathcal{C}_{q,r}]\,;\ \ell = 1, 2, 3, \ldots, M_{\boldsymbol{x}}$
        Compute: $\text{SID}_{m,r}$ between $\psi(\tilde{\boldsymbol{c}}_\ell)$ and $\psi(\boldsymbol{c}_j)$ based on Equation (3) of the Main Manuscript
Compute: $\text{CSID}_m = \sum_r \text{SID}_{m,r}(\mu_p \| \mu_q)$
Output: Plot of $\text{SID}_{m,r}$ versus $r$; Measure $\text{CSID}_m$
```

B.3. Experiments on Gaussian Data

To begin with, we present results on computing the signed distance (SD) for various representative Gaussian and Gaussian mixture source and target distributions.

Figures 2(a)-(c) present the visualization of SD versus r for a Gaussian target distribution with $\mu_q = \mathcal{N}(5.5\mathbf{1}_2, 0.75\mathbb{I}_2)$, where $\mathbf{1}_2$ denotes a 2-D vector with all entries equal to 1. Consider the scenario where the source and target Gaussians possess the same variance, but different means. Consider three different sources $\mu_p = \mathcal{N}(\boldsymbol{m}_p, \Sigma_p)$, given by: (a) $\boldsymbol{m}_p = \mathbf{0}_2$ and $\Sigma_p = 0.75\mathbb{I}_2$; (b) $\boldsymbol{m}_p = 2.5\mathbf{1}_2$ and $\Sigma_p = 0.75\mathbb{I}_2$; and (c) $\boldsymbol{m}_p = 5.5\mathbf{1}_2$ and $\Sigma_p = 0.75\mathbb{I}_2$. We observe that, when the source is far away from the target, SD is positive-valued and gradually approaches zero. When the two distributions are identical, SD is zero for all r. In the context of identifying a friendly neighbor, a closer source dataset is expected to converge faster to zero than one that is far away.

Figures 3(a)-(c) present the results for the other scenario where the mean is fixed, but the variances are different. Consider the same target as before, but with the following source distributions: (a) $\boldsymbol{m}_p = 5\mathbf{1}_2$ and $\Sigma_p = 0.1\mathbb{I}_2$; (b) $\boldsymbol{m}_p = 5\mathbf{1}_2$ and $\Sigma_p = 0.25\mathbb{I}_2$; and (c) $\boldsymbol{m}_p = \mathbf{1}_2$ and $\Sigma_p = \mathbb{I}_2$. We observe that when the spread of the source is smaller than the target, SD initially goes negative, and subsequently converges to zero once the hypercube $\mathcal{C}_{q,r}$ encompasses the source. On the other hand, when the spread of the source is greater than that of the target (as desired for identifying friendly neighbors), SD is always positive, and converges to zero faster if the relative spread between the source and target is smaller.

To evaluate SD on a Gaussian mixture target, consider an 8-component Gaussian mixture model (GMM) with means drawn from $[0, 1] \times [0, 1]$ and identical covariance matrices $0.02\mathbb{I}_2$. Consider three source distributions: (a) A Gaussian with first and second moments matching that of the target; (b) An 8-component GMM distinct from the target; and (c) A 4-component

GMM that has mode-collapsed on to some of the modes of the target. Figures 4(a)-(c) present these three scenarios and the associated SD versus r. For Scenario (a), although the mean and covariance of both the source and target are identical, we observe that SD is negative, as the two distributions do not have a large overlap, preventing the positive and negative charges from cancelling each other. In Scenario (b), SD is able to capture the change in concentration between μ_p and μ_q, indicated by the sudden sign change in SD. When μ_p converges to a few modes of the target μ_q, SD is not zero for all r, which indicates that the two distributions are not identical. In this scenario, however, FID between the two distribution would be close to zero as they have approximately the same first and second moments.

Animations pertaining to these experiments are available at `https://github.com/DarthSid95/clean-sid`.

B.4. Evaluating GANs with SID

We consider evaluating pre-trained models with the SID measure to compare the performance with FID and KID. As a demonstration, we consider StyleGAN2 [11] and StyleGAN3 [12] models with weights trained on 512×512 high-quality Animal Faces (AFHQ) dataset [11]. As a reference/benchmark, we also consider SID of the AFHQ dataset with itself. We consider orders in the range $m = \lfloor \frac{n}{2} \rfloor - 3, \lfloor \frac{n}{2} \rfloor - 2, \ldots \lfloor \frac{n}{2} \rfloor + 2$. Figure 5 shows SID for select orders, comparing StyleGAN2 and StyleGAN3. For positive orders, we flip the sign of SID to maintain consistency with the interpretations developed for the negative order. Across all test cases, we observe that StyleGAN3 outperforms StyleGAN2, as suggested by the FID and KID values [10]. As the order m reduces, GAN models with lower FID/KID/CSID$_m$ approach zero more rapidly, which can be used to quantity the relative performance of converged GAN models. For $m < \lfloor \frac{n}{2} \rfloor - 3$ numerical instability causes SID to approach zero and for $m > \lfloor \frac{n}{2} \rfloor + 2$ numerical instability blows up SID computation. While these experiments serve to demonstrate the feasibility in evaluating pre-trained GAN models with CSID$_m$, comparisons between Spider DCGAN and the corresponding baselines are provided in Section 4 of the *Main Manuscript* and Appendix D.2 of this *Supporting Document*, while comparisons of Spider StyleGANs and baseline StyleGANs on FFHQ and MetFaces is provided in Appendix D.5.

SID can also be used to compare the relative performance of GAN generators. Consider three GANs trained on the MNIST dataset where one generator has learnt the distribution accurately, while the other two have *mode-collapsed* on to a subset of the classes (specifically, digits 0,8,6 and 9) or a single class (digit 4) of the target dataset. Figure 6 presents samples output by these generators and the SID versus r plot for the corresponding pair of generators. We observe that, when the reference generator has learnt the target accurately, the SID of a test generator's output with respect to the reference will always be negative, as the test generator has less diversity. However, the SID between the output of two generators that have mode-collapsed would be positive if there is no overlap between the classes they have collapsed to. This could be used to evaluate GANs with ensemble-generators [13], where each network is trained to learn a different mode/class.

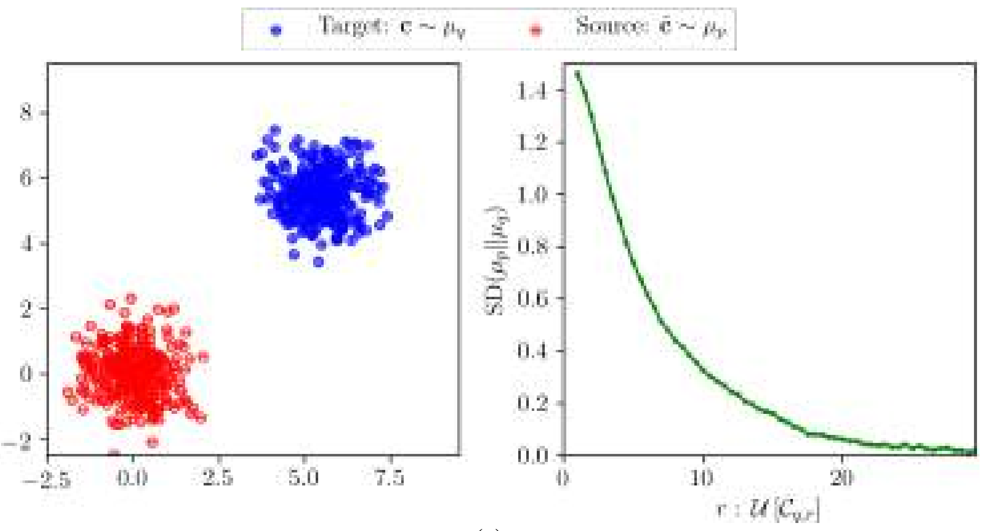

(a)

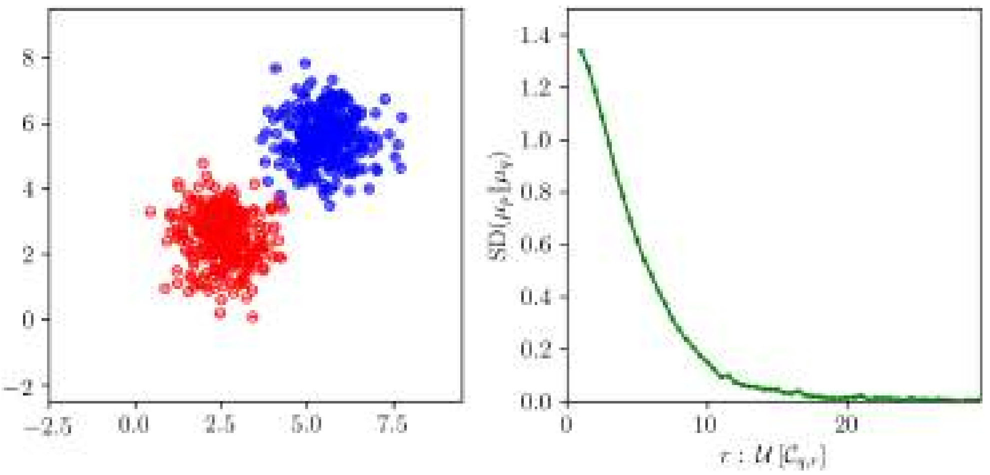

(b)

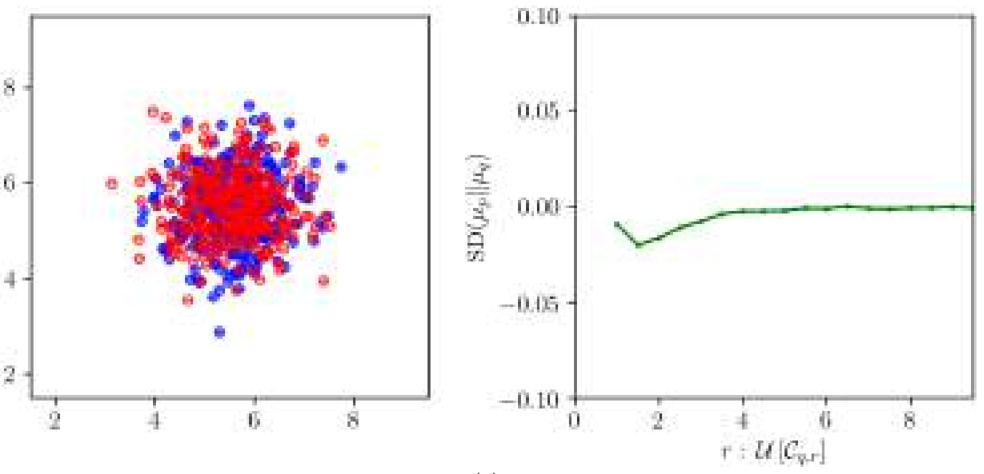

(c)

Figure 2. Plots of the signed distance $\mathrm{SD}_{m,r}$ between a source Gaussian $\mu_p = \mathcal{N}(\boldsymbol{m}, 0.75\mathbb{I}_2)$ from a target Gaussian $\mu_q = \mathcal{N}(5.5\mathbf{1}_2, 0.75\mathbb{I}_2)$ for (a) $\boldsymbol{m}_p = \mathbf{0}_2$; (b) $\boldsymbol{m}_p = 2.5\mathbf{1}_2$; and (c) $\boldsymbol{m}_p = 5.5\mathbf{1}_2$. The closer the source Gaussian is to the target, the faster $\mathrm{SD}_{m,r}(\mu_p\|\mu_q)$ approaches zero. When the two distributions coincide, $\mathrm{SD}_{m,r}(\mu_p\|\mu_q)$ is zero for all r.

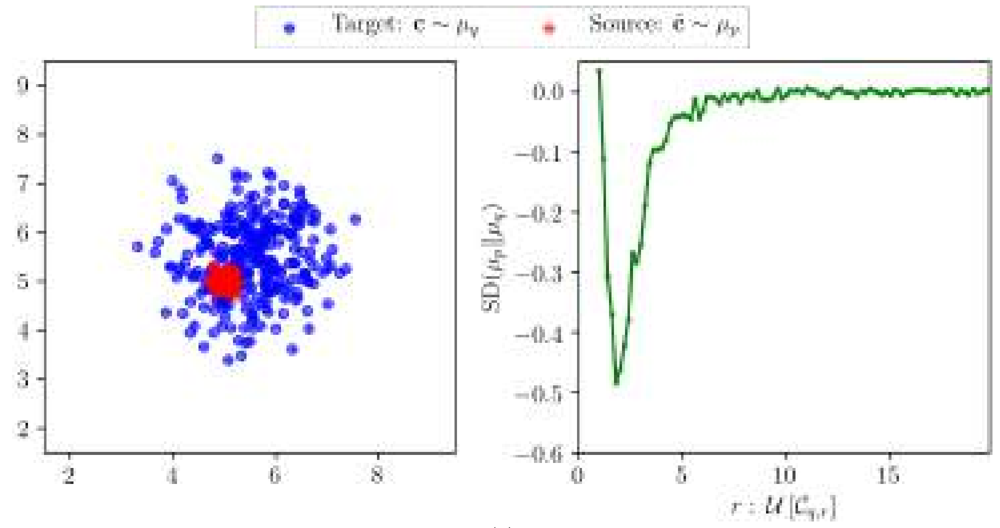

(a)

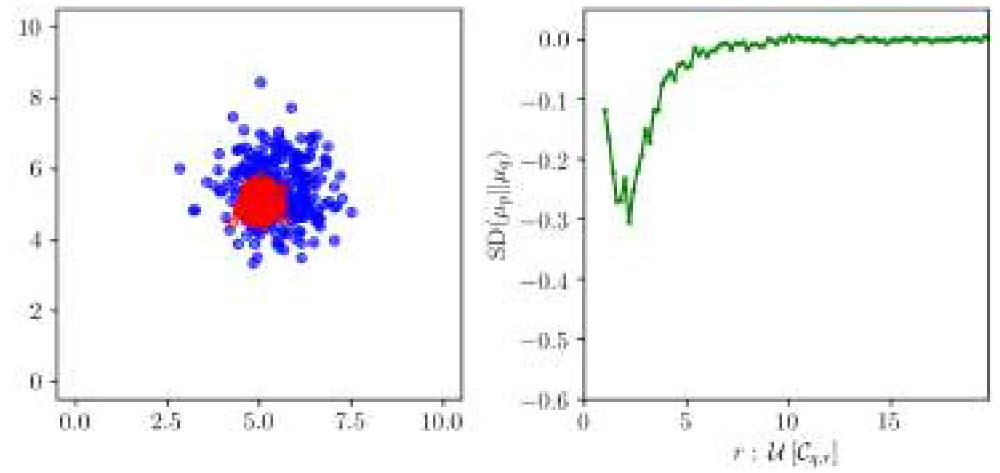

(b)

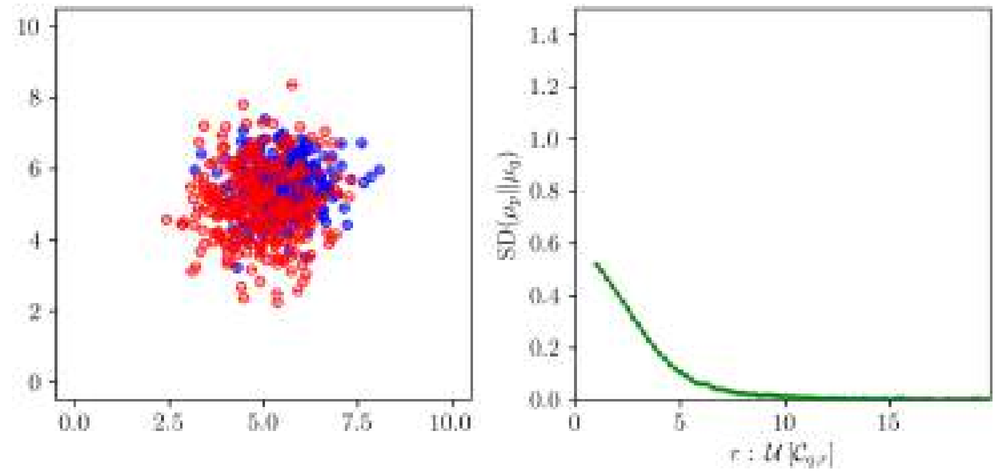

(c)

Figure 3. Plots comparing the signed distance $\mathrm{SD}_{m,r}$ between a source Gaussian $\mu_p = \mathcal{N}(5.5\mathbf{1}_2, 0.75\mathbb{I}_2)$ and a target Gaussian $\mu_q = \mathcal{N}(5.5\mathbf{1}_2, \Sigma_p)$ for (a) $\Sigma_p = 0.1\mathbb{I}_2$; (b) $\Sigma_p = 0.25\mathbb{I}_2$; and (c) $\Sigma_p = \mathbb{I}_2$. When the source Gaussian overlaps with the target but with a smaller variance, $\mathrm{SD}_{m,r}$ is negative. However, if the source has a larger variance than the target, $\mathrm{SD}_{m,r}$ is positive.

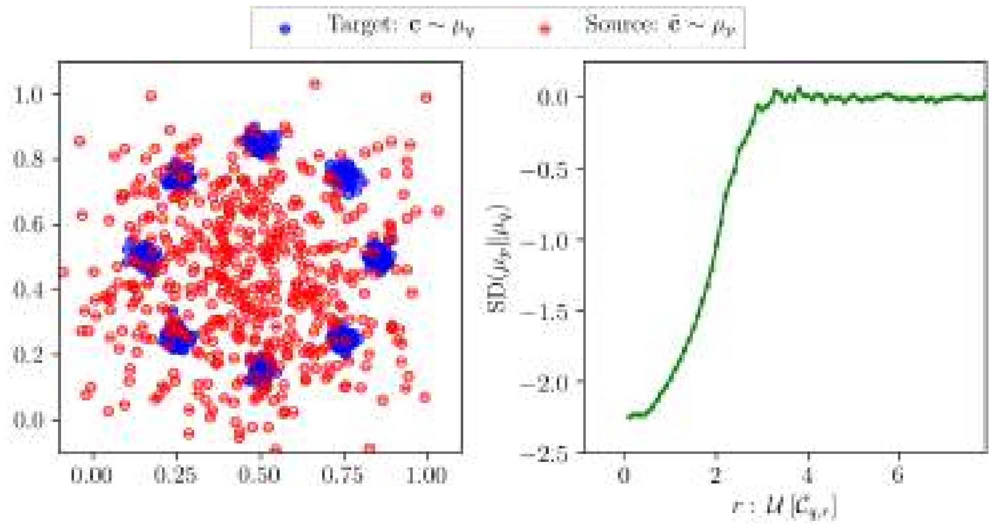

(a)

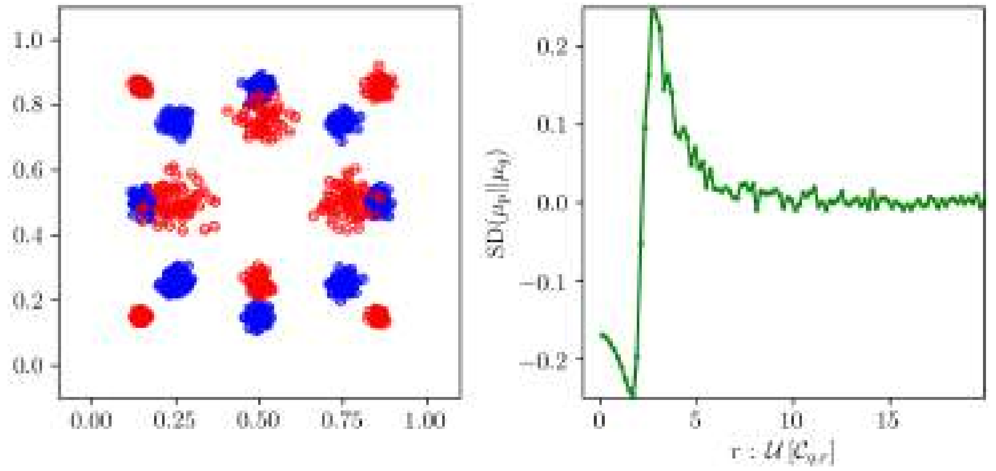

(b)

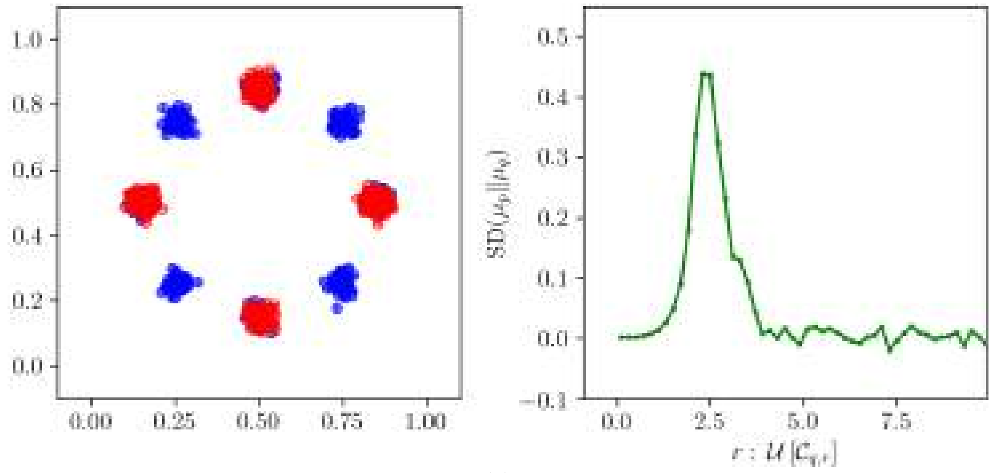

(c)

Figure 4. Plots comparing the signed distance $\mathrm{SD}_{m,r}$ when the target is a Gaussian mixture density. (a) Unimodal Gaussian source with identical first and second moments as the target; $\mathrm{SD}_{m,r}$ is negative as the source has lower diversity than the target. (b) A Gaussian mixture distinct from the target; $\mathrm{SD}_{m,r}$ flips sign based on the relative concentrations of the source and target samples. (c) A mode-collapsed source results in a non-zero $\mathrm{SD}_{m,r}$ although FID and KID between these distributions would be zero.

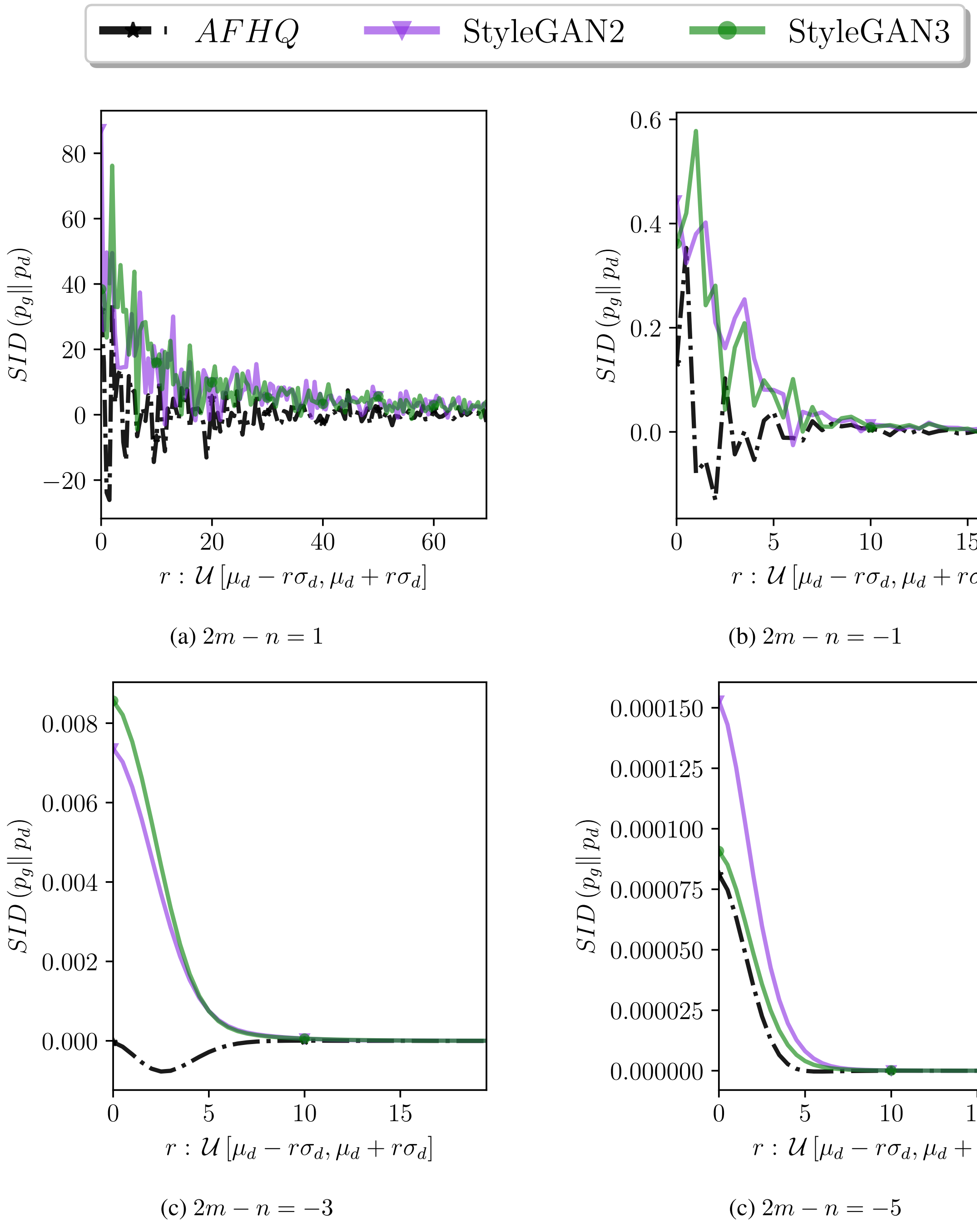

Figure 5. SID versus r for multiple choices of $2m - n$ for the case when the target dataset is 512×512 Animal Faces HQ. Images generated by StyleGAN2 and StyleGAN3 are compared with the AFHQ dataset as the target. We observe that StyleGAN3 has a performance comparable to StyleGAN2 for higher orders m. Convergence for lower orders is indicative of superior performance, as the penalty for mismatch between the source and target distributions increases with decrease in the order. The SID for StyleGAN3 closely matches the SID of the target data with itself for $2m - n = -5$, indicating superior performance to StyleGAN2. This finding is in agreement with the comparison between StyleGAN2 and StyleGAN3 in terms of FID/KID reported in [10].

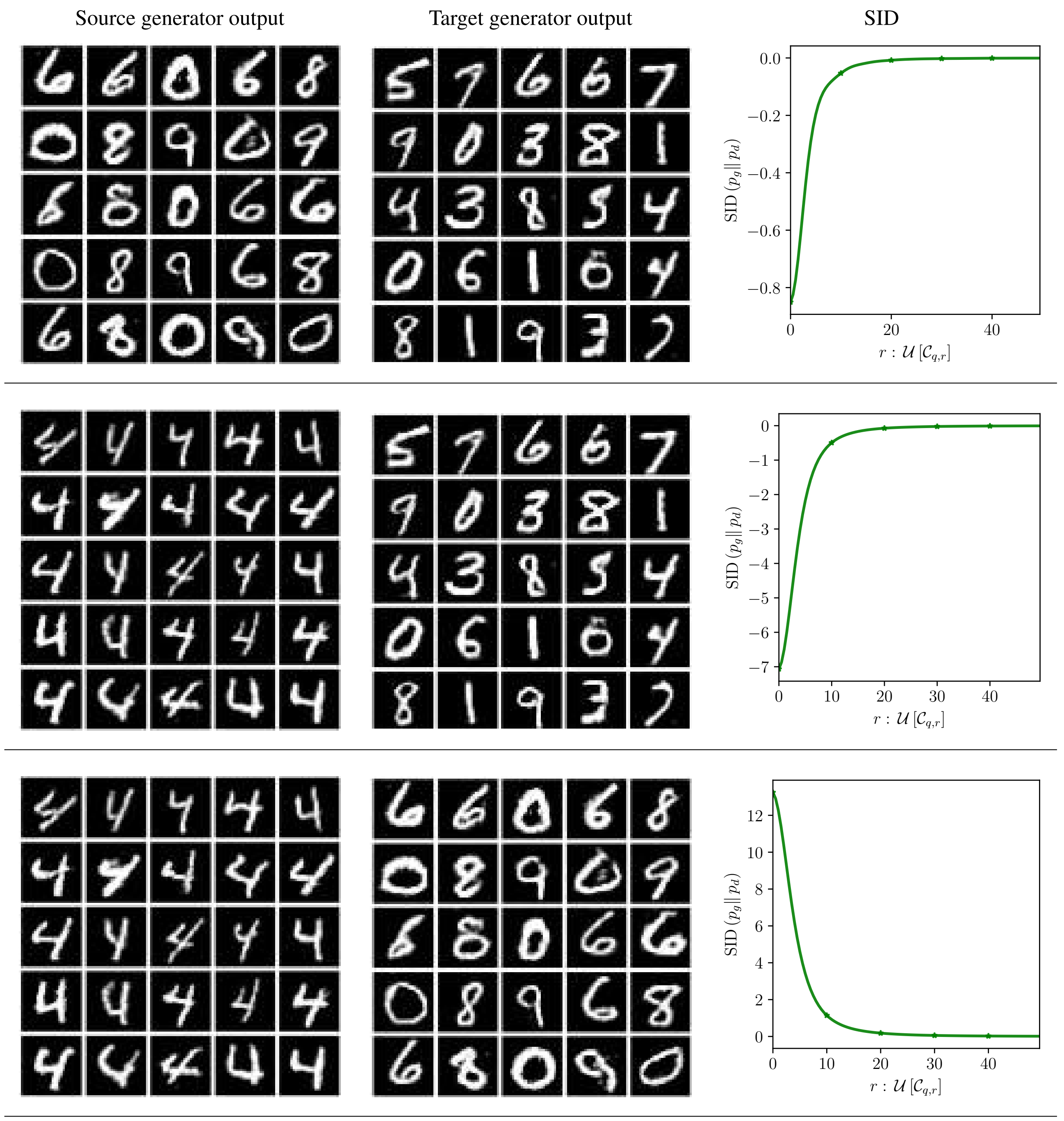

Figure 6. SID versus r when the source and target samples are drawn from GAN generators trained on various subsets of MNIST. When the source generator has mode-collapsed, either to a single digit or a subset of digits, the corresponding SID is negative. When comparing two mode-collapsed generators, the SID will be positive as the distributions of the Inception embeddings are less likely to overlap.

C. Implementation Details

We provide details on the experimental setup, evaluation metrics and computational resources employed in the various experiments reported in the *Main Manuscript* and this *Supporting Document*.

C.1. Experimental Setup

Spider DCGAN: The experiments presented in Section 4 consider the DCGAN [14] architecture for the generator and discriminator. For the baseline GANs, the parametric input is drawn from $\mathbb{R}^{100}$. We consider the Gaussian, Gamma [15] and non-parametric [16] input distributions drawn from $\mathbb{R}^{100}$ as baselines. In the case of Spider GAN, we conducted experiments by resizing the input data to $16 \times 16 \times 3$. To bridge the gap between the two noise variants, we also consider Gaussian noise drawn from $\mathbb{R}^{16\times16\times3}$ provided as input in a similar fashion to the datasets. We did not observe improvement in performance with higher-resolution images for the input dataset. The images are vectorized and provided as input to the generator. Both Spider DCGAN and the baselines are trained on the Wasserstein GAN [17] loss with a stable version of the gradient penalty [18] enforced only on samples drawn from p_d. The choice was motivated by its successful usage in baseline StyleGAN2 and StyleGAN3 variants.

The networks are trained on batches of 100 samples. The Adam [19] optimizer is used with a learning rate $\eta = 2 \times 10^{-4}$, and the exponential decay parameters for the first and second moments are $\beta_1 = 0.5$ and $\beta_2 = 0.999$, respectively. The implementation was carried out using TensorFlow 2.0 [20]. The networks are trained for 15×10^3 iterations on MNIST and Fashion-MNIST, 10^4 iterations on SVHN and CIFAR-10, and 3×10^4 iterations on Celeb-A, Ukiyo-E and Tiny-ImageNet learning tasks.

Spider PGGAN: The publicly available PGGAN GitHub repository (URL: `https://github.com/tkarras/progressive_growing_of_gans`) was extended to incorporate the *Spider* framework. The implementation was carried out using TensorFlow 2.0 [20]. The input distributions are drawn from PGGAN models, trained on Tiny-ImageNet images of resolution $16 \times 16 \times 3$. The input PGGAN was trained for 12×10^3 iterations. Samples drawn from the input PGGAN are resized to $14 \times 14 \times 3$, vectorized, and provided as input to the cascaded Spider PGGAN layer.

Spider StyleGAN: The publicly available, PyTorch 1.10 [21] based StyleGAN3 GitHub repository (URL: `https://github.com/NVlabs/stylegan3`) was extended to incorporate the *Spider* framework, allowing for the implementation of both StyleGAN2, StyleGAN2-ADA and StyleGAN3 variants. The input distributions are drawn from StyleGAN2-ADA models, trained on (a) Tiny-ImageNet images of resolution $16 \times 16 \times 3$; and (b) Images from the AFHQ-Dogs dataset, resized to $16 \times 16 \times 3$. The input StyleGAN was trained for 25×10^3 iterations in both cases. We considered the following two input transformations to obtained 512-dimensional input vectors: (i) Samples drawn from the input StyleGAN are averaged across the color channels, resized to $16 \times 32 \times 1$, vectorized, and provided as input to the cascaded layer; and (ii) Samples drawn from the input StyleGAN are averaged across the color channels, resized to $23 \times 23 \times 1$ and vectorized. The vectors are truncated to 512 entries, and provided as input to the cascaded stage. We did not observe a significant difference in performance when considering either of the two configurations. As in classical StyleGANs, the cascaded StyleGAN network transforms the input dataset to the latent $\mathcal{W}$-space, and subsequently learn the target. Spider StyleGANs are trained with transformation-(i) on FFHQ and AFHQ-Cats data, while transformation-(ii) is used to train the Spider StyleGAN variants on Ukiyo-E faces and MetFaces.

C.2. Evaluation Metrics

To draw a fair comparison with the baseline approaches, we evaluate various Spider GAN and baseline models in terms of their FID, KID and CSID$_m$. We also compare the interpolation quality of the networks based on the sharpness of the interpolated images.

Fréchet Inception Distance (FID): Proposed by Heusel *et al.* [22], FID can be used to quantify how *real* samples generated by GANs are. FID is computed as the Wasserstein distance between Gaussian distributed embeddings of the generated and target images. To compute the image embedding, we consider the InceptionV3 [23] model without the topmost layer, loaded with weights for the ImageNet [24] classification task. Images are resized to $299 \times 299 \times 3$ and given as input to these networks. Grayscale images are replicated across the color channels. FID is computed by assuming a Gaussian prior on the embeddings of real and fake images. The means and covariances are estimated using $10,000$ samples. The publicly available TensorFlow based *Clean-FID* library [10] is used to compute FID. As noted by Parmar *et al.* [10], the Clean-FID is generally found to be a few points higher than those computed through base PyTorch and TensorFlow implementations. Our implementation of the DCGAN baselines [15, 16] also exhibit similar offsets between the reported FID and those computed by Clean-FID. However, in our experiments, we were able to reproduce the scores reported in [10] for PGGAN and StyleGAN architectures fairly accurately.

Kernel Inception Distance (KID): The kernel inception distance [25] is an unbiased alternative to FID. The KID computes the squared maximum-mean discrepancy (MMD) between the InceptionV3 embeddings of data in $\mathbb{R}^n$. The embeddings are computed as in the FID case. The third-order polynomial kernel $\mathcal{K}(\boldsymbol{x},\boldsymbol{y}) = \left(\frac{1}{n}\boldsymbol{x}^{\mathrm{T}}\boldsymbol{y}+1\right)^3$ is used to compute the MMD over a batch of 5000 samples. As in the case of FID, to maintain consistency, we use the *Clean-FID* [10] library implementation of KID.
Image Interpolation and Sharpness: In order to compare the performance of GAN for generating unseen images, we evaluate the output of the generator when the interpolated points between two input distribution samples are provided to the generator. We use the sharpness metric introduces by Tolstikhin *et al.* [26] in the context of Wasserstein autoencoders. The edge-map of an image is obtained using the Laplacian operator. The average sharpness of the images is then defined as the variance in pixel intensities on the edge-map, averaged over batches of $50,000$ images. In the case of of baseline GAN, the inputs are interpolated points between random samples drawn from the parametric noise distribution, while in the case of Spider GAN, the interpolation between two images from the input dataset are fed to the generator.

C.3. Computational Resources

All experiments on low-resolution ($\leq 32 \times 32 \times 3$) images with the DCGAN architecture were conducted on workstations with one of two configuration: (a) $4\times$ NVIDIA 2080Ti GPUs with 11 GB visual RAM (VRAM) each, and 256 GB system RAM; and (b) $2\times$ NVIDIA 3090 GPUs with 24 GB VRAM and 256 GB system RAM. The high-resolution experimentation involving PGGAN or StyleGAN was carried out on workstations with one of the two configurations: (i) NVIDIA DGX with $8\times$ Tesla V100 GPUs with 32 GB VRAM each, and 512 GB system RAM; and (ii) $8\times$ NVIDIA A6000 GPUs with 48 GB VRAM each, and 512 GB system RAM. The memory requirements and training times for StyleGAN and PGGAN variants are on par with training times reported for the baselines [27, 12].

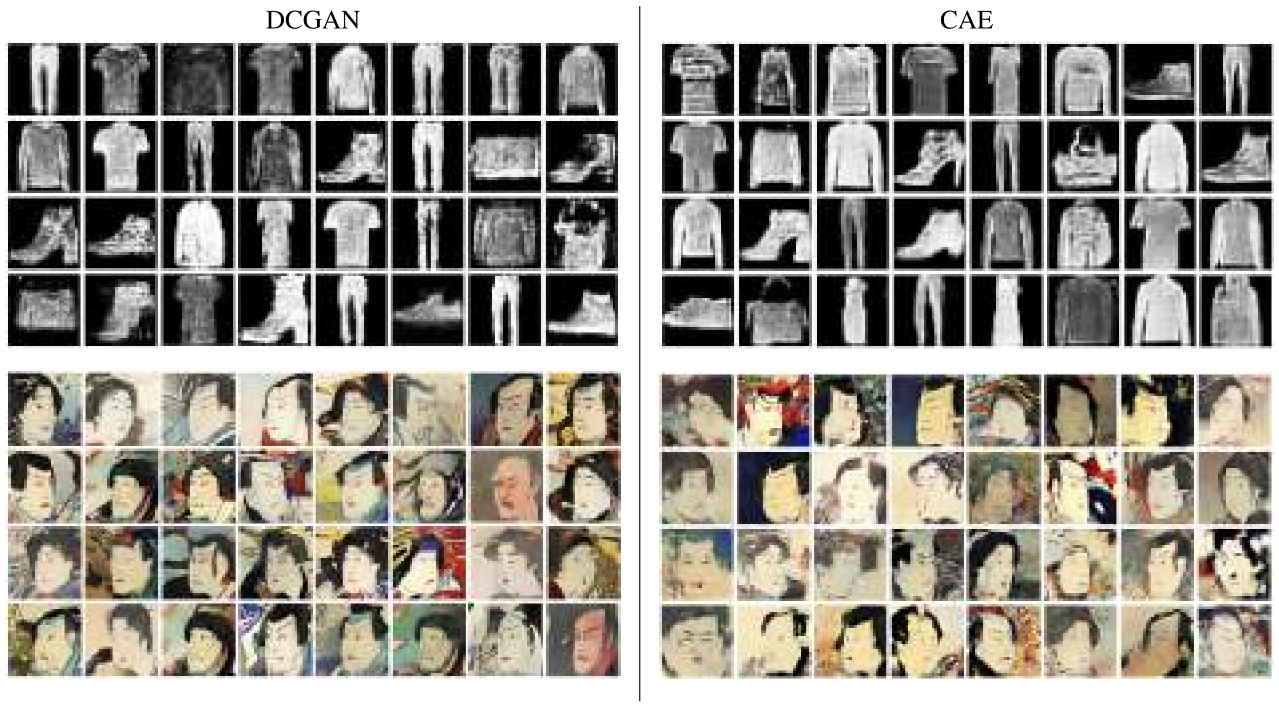

Figure 7. Images generated by Spider GAN on Fashion-MNIST and Ukiyo-E Faces, given the friendliest neighbor input as identified by SID. Both CAE and DCGAN result in images of comparable visual quality on Fashion-MNIST. However, for high-resolution image generation on 256-dimensional Ukiyo-E Faces, the fully convolutional structure of the CAE generator result in images of poorer visual quality than those generated by DCGAN.

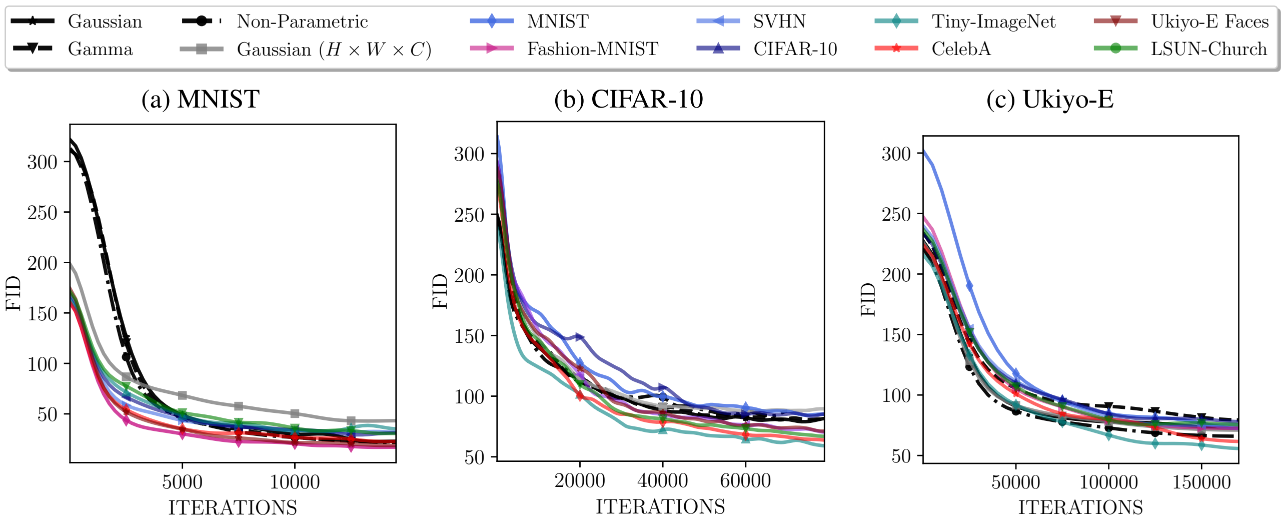

Figure 8. FID versus iterations for training baseline and Spider GAN variants. Spider GAN trained with the friendliest neighbor identified in Section 3 (of the *Main Manuscript*) result in the best (lowest) FID scores. On MNIST, Spider DCGAN approaches converge an order faster than the baseline counterparts.

Table 5. Comparison of FID, KID and CSID$_m$ for the Spider DCGAN and baseline variants on Fashion-MNIST, SVHN, Tiny-ImageNet, and CelebA datasets. Spider DCGANs with *friendly neighborhood* inputs outperform the baselines with parametric and non-parametric priors. The performance of Spider DCGAN with MNIST or Fashion-MNIST as the input is sub par when the target is a color-image dataset.

	Input Distribution	Fashion-MNIST			SVHN			Tiny-ImageNet			CelebA		
		FID	KID	CSID$_m$	FID	KID	CSID$_m$	FID	KID	CSID$_m$	FID	KID	CSID$_m$
Baselines	Gaussian ($\mathbb{R}^{100}$)	76.60	0.0557	22.24	135.4	0.1245	30.02	89.94	0.0657	18.06	50.32	0.0554	24.31
	Gamma ($\mathbb{R}^{100}$)	65.36	0.0513	19.72	130.8	0.1181	27.13	83.33	0.0536	14.63	40.69	0.0544	20.98
	Non-Parametric ($\mathbb{R}^{100}$)	62.42	0.0426	21.96	107.2	0.1053	33.52	82.37	0.0579	13.25	40.41	0.0543	72.18
	Gaussian ($\mathbb{R}^{H\times W\times C}$)	119.2	0.0905	28.96	113.7	0.1121	31.45	103.0	0.0844	15.62	83.61	0.0912	113.4
Spider GAN	MNIST	**56.59**	**0.0387**	**18.50**	**95.71**	**0.0817**	**20.62**	96.91	0.0669	14.95	40.78	0.0595	32.70
	Fashion MNIST	–	–	–	115.0	0.1096	32.57	108.8	0.0667	13.06	35.18	0.0574	23.98
	SVHN	79.14	0.0526	24.67	–	–	–	98.11	0.0655	15.62	40.27	0.0575	20.64
	CIFAR-10	92.60	0.0658	30.21	101.8	0.0998	32.40	98.22	0.0642	17.90	36.16	0.0508	22.16
	TinyImageNet	130.5	0.0883	22.26	111.7	0.1082	31.77	–	–	–	**29.47**	**0.0468**	**18.16**
	CelebA	81.38	0.0604	24.73	108.9	0.1029	22.77	**75.68**	**0.0511**	**12.42**	–	–	–
	Ukiyo-E	66.90	0.0475	23.29	114.8	0.1145	38.28	88.51	0.0612	16.01	39.41	0.0630	28.23
	LSUN-Churches	102.9	0.0774	33.87	106.8	0.1020	26.52	92.86	0.0697	15.98	53.01	0.0636	25.72

D. Additional Experimentation on Spider GAN

We now discuss additional experimental results and ablation studies on various *Spider GAN* flavors presented in the *Main Manuscript*. One could also extend the *Spider* philosophy to VQGAN [28, 29] or diverse class-conditional models [30, 31]

D.1. Exploring Generator Architectures

We now discuss the choice of the generator architecture in Spider GAN (cf. Section 4 of the *Main Manuscript*). We consider two network architectures:

- **DCGAN**: We consider standard DCGAN where the images from the friendly neighborhoot are resized, vectorized, and provided as input to generator as described in Appendix C.1.
- **Convolutional autoencoder (CAE)**: In this setup, the images are resized to $16 \times 16 \times 3$ and provided as input to convolutional layers to learn a low-dimensional latent representation. The output image is generated by deconvolution layers.

Table 6. A comparison of FID and KID in Spider GAN for various noise perturbations considered when the input dataset is Ukiyo-E Faces. Gaussian perturbations such as $\mathcal{N}(\mathbf{0}, 0.25\mathbb{I})$ and $\mathcal{N}(\mathbf{0}, 0.1\mathbb{I})$ that are concentrated about their mean result in the best performance improvements over the baseline Spider GAN.

Input Distribution	Fashion-MNIST		CIFAR-10	
	FID ↓	KID ↓	FID ↓	KID ↓
Ukiyo-E Faces	55.1200	0.0376	74.7085	0.0518
Ukiyo-E + $\mathcal{N}(\mathbf{0}, 0.1\mathbb{I})$	**47.2873**	**0.0285**	<u>70.101</u>	0.0488
Ukiyo-E + $\mathcal{N}(\mathbf{0}, 0.25\mathbb{I})$	<u>50.2150</u>	0.0345	**68.7473**	**0.0473**
Ukiyo-E + $\mathcal{N}(\mathbf{0}, \mathbb{I})$	79.8415	0.0690	71.9181	0.0531
Ukiyo-E + Gamma noise	51.8201	0.0343	70.362	<u>0.0476</u>
Ukiyo-E + Non-parametric noise	50.8536	<u>0.0329</u>	72.9138	0.0495

The number of trainable parameters are fewer for the CAE architecture than the DCGAN approach in both cases. Figure 7 shows the output images generated by these approaches considering the friendliest neighbor (as suggested by Tables 1-4) provided as input when learning the Fashion-MNIST and Ukiyo-E Faces datasets. We observe that the CAE based Spider GAN outperforms the DCGAN approach on Fashion-MNIST. However, on higher resolution images, multiple visual artifacts were found as a consequence of the fully convolutional architecture. We observed similar degradation in image quality when training Spider GAN with CAE on other high-resolution datasets such as CelebA. We therefore consider the DCGAN approach in the experiments presented in Section 4 of the *Main Manuscript* and Appendix D.2.

D.2. Additional Experiments on Spider DCGAN

We now present results on additional experimental validation run on the Spider DCGAN architecture. The experimental setup is the same as the one described in Appendix C.1. First, we consider training Spider GAN on Fashion-MNIST, SVHN, Tiny-ImageNet and 64-dimensional CelebA datasets. The FID and KID of the converged models are presented in Table 5. On the Fashion-MNIST, SVHN, and CelebA datasets, we observe that the Spider GAN approach with the friendliest neighbor (as identified by FID, KID and CSID$_m$), results in improved learning over the baselines. On the Tiny-ImageNet learning task, we observe that a source dataset with less diversity (such as CIFAR-10, as suggested by FID and KID) performs poorly, while a more diverse source dataset, such as CelebA, improves the best-case FID over the baselines. These results validate the *friendly neighborhood* of Tiny-ImageNet identified using CSID$_m$ in Section 3 of the *Main Manuscript*, where CIFAR-10 and LSUN-Churches are less diverse, having a negative CSID$_m$. Figures 10-16 present the images generated by Spider GAN and the baseline variants on various datasets considered. Figure 8 presents the convergence of FID as a function of iterations for the remaining source dataset combinations of Spider GAN models considered in Section 4 and Figure 4 of the *Main Manuscript*.

D.2.1 Noise Perturbations on the Input Dataset

The SpiderGAN framework relies on the variability present in the chosen input dataset to learn the target better. As discussed in Section 4 of the *Main Manuscript*, we considered addition of noise to the dataset input to the Spider GAN generator when the cardinality of the input is small. We observed that CelebA or Tiny-ImageNet are more diverse and perform better than small datasets such as Ukiyo-E Faces. To overcome the lack of diversity in small datasets, we consider additive-noise perturbations to augment the data. While Gaussians are a popular choice, we also consider the Gamma density and non-parametric densities to generate noise, which are known to improve the performance of the GANs on latent-space interpolation. We consider three Gaussian examples: the standard normal $\mathcal{N}(\mathbf{0}, \mathbb{I})$, $\mathcal{N}(\mathbf{0}, 0.25\mathbb{I})$, and $\mathcal{N}(\mathbf{0}, 0.1\mathbb{I})$. Three variances are considered to highlight the trade-off between generating noisy images (Gaussians with high variance) and low diversity in the input dataset (Gaussians with low variance). We present results on learning MNIST and CIFAR-10 datasets with Ukiyo-E Faces dataset as input.
Results: Figures 17(a)-(f) show the images generated by Spider GAN with various noise perturbations applied to Ukiyo-E Faces. Adding Gaussian noise with a small variance, or Gamma distributed noise results in diverse images and better visual quality of generated images. On the other hand, models trained with the standard normal or non-parametric densities resulted in poor learning, with several out-of-distribution images. The performance of the converged models in presented in Table 6.

Perturbations that are Gaussian, and concentrated about the mean, such as $\mathcal{N}(\mathbf{0}, 0.1\mathbb{I})$ or $\mathcal{N}(\mathbf{0}, 0.25\mathbb{I})$ resulted in the lowest FID and KID. Therefore, Gaussian perturbations with a small variance result in better performance when the input datasets have small cardinality.

Table 7. Comparison of sharpness metric evaluated on interpolated images in MNIST, CIFAR-10 and Ukiyo-E learning tasks. The benchmark sharpness is computed on target data samples. Spider GAN variants outperform the baselines on CIFAR-10 and MNIST, while being on par with the non-parametric prior on the Ukiyo-E Faces. The values shown in **bold** are closest to the benchmark sharpness.

	Input Distribution	Sharpness of the Interpolated Image		
		MNIST	CIFAR-10	Ukiyo-E
Baselines	Gaussian	0.0868	0.587	1.730
	Gamma	0.0536	1.217	1.981
	Non-parametric	0.2522	0.785	**2.538**
SpiderGAN	MNIST	–	0.467	2.008
	Fashion MNIST	**0.1408**	0.377	1.353
	SVHN	0.0898	1.214	1.480
	CIFAR-10	0.0859	–	2.533
	TinyImageNet	0.0623	**0.906**	1.274
	CelebA	0.1735	0.449	2.104
	Benchmark	0.1396	0.993	2.748

Table 8. Comparison of *Interpolation FID* and *Interpolation KID* for the Spider GAN and baseline variants on MNIST, CIFAR-10, and Ukiyo-E Faces datasets. The input provided to the generator $\boldsymbol{z}_{in} = \frac{\boldsymbol{z}_1+\boldsymbol{z}_2}{2}$; $\boldsymbol{z}_1, \boldsymbol{z}_2 \sim p_Z$ is the mid-point between two samples drawn from the input distribution p_Z, either of parametric form in the case of the baselines, or the *friendly neighborhood* datasets, in the case of Spider GAN. The values in the parentheses indicate the relative increase in the FID/KID scores, in comparison to those reported in Table 2 of the *Main Manuscript*. Spider GANs with *friendliest neighborhood* input datasets achieve FID and KID scores on par with the best-case baseline.

	Input Distribution	MNIST		CIFAR10		Ukiyo-E Faces	
		FID	KID	FID	KID	FID	KID
Baselines	Gaussian ($\mathbb{R}^{100}$)	25.111 (+16.8%)	0.0181 (+30.2%)	121.198 (+68.7%)	0.0848 (+36.9%)	74.241 (+3.1%)	0.0612 (+14.4%)
	Gamma ($\mathbb{R}^{100}$)	23.564 (+11.3%)	0.0149 (+12.1%)	77.113 (+6.1%)	0.0492 (+1.8%)	70.302 (+0.4%)	0.0558 (+18.7%)
	Non-Parametric ($\mathbb{R}^{100}$)	22.301 (+6.4%)	0.0142 (+3.6%)	87.478 (+16.7%)	0.0568 (+7.1%)	**66.022** (+1.0%)	**0.0434** (+3.0%)
Spider GAN	MNIST	–	–	122.084 (+71.2%)	0.0790 (+47.5%)	103.80 (+51.4%)	0.0732 (+67.1%)
	Fashion MNIST	**20.644** (+22.8%)	**0.0147** (+42.7%)	113.109 (+46.7%)	0.0731 (+32.9%)	89.901 (+23.6%)	0.0654 (+43.7%)
	SVHN	27.630 (+1.8%)	0.0208 (+1.5%)	89.161 (+39.1%)	0.0558 (+23.7%)	77.302 (+10.0%)	0.0542 (+12.4%)
	CIFAR-10	30.214 (+3.4%)	0.0305 (+38.6%)	–	–	87.981 (+24.2%)	0.0621 (+17.1%)
	TinyImageNet	46.233 (+41.6%)	0.0397 (+50.4%)	86.708 (+47.3%)	**0.0520** (+70.4%)	79.848 (+28.9%)	0.0565 (+29.5%)
	CelebA	21.517 (+4.6%)	0.0152 (+5.5%)	**86.475** (+43.9%)	0.0534 (+23.0%)	68.849 (+27.2%)	0.0449 (+10.1%)
	Ukiyo-E	38.950 (+26.9%)	0.0318 (+39.4%)	98.045 (+60.6%)	0.0671 (+83.8%)	–	–

D.2.2 Input-space Interpolation with Spider DCGAN

Gamma and non-parametric priors were introduced to the GAN landscape to improve the quality of interpolated images in GANs [15, 16]. We compare the image interpolation quality of Spider GAN with respect to the gamma and non-parametric baselines. The experimental setup is similar to that in Appendix C.1. We compare the visual quality of images generated by interpolated inputs to the generator. In the baseline GANs, we provide the generator with eight linearly interpolated points between two random samples drawn from the prior densities. In the case of Spider GAN, we draw two random samples from the input dataset, and generate eight linearly interpolated images that are input to the Spider GAN generator. The quality of the interpolation is evaluated in terms of the sharpness metric. We present results on MNIST, CIFAR-10, and Ukiyo-E Faces.

Figures 18-20 present the images generated by the interpolated input vectors by the three baseline GAN variants and Spider GAN with the three friendliest neighbors as the input datasets. We observe that, Spider GAN, although not trained for the task, is able to generate realistic interpolated images. The visual quality is on par with the non-parametric interpolation scheme in the case of MNIST, and superior to the baselines on the Ukiyo-E Faces learning task. All variants fail to generate realistic images on CIFAR-10. Table 7 shows the sharpness metric computed on the interpolated images. We observe that Spider GAN variants attain values closer to the benchmark in comparison with the baselines. As discussed in the Main Manuscript, the best performance of Spider GAN is achieved when the input dataset is the *friendliest neighbor* of all the target datasets under consideration. Table 8 presents the FID and KID scores of the Spider GAN and baseline variants, when computed on a batch of 10^4 samples obtained by proving the mid-point sample $\boldsymbol{z}_{in} = \frac{\boldsymbol{z}_1+\boldsymbol{z}_2}{2}$; $\boldsymbol{z}_1, \boldsymbol{z}_2 \sim p_Z$ as input to the generator. The inputs $\boldsymbol{z}_1$ and $\boldsymbol{z}_2$ are samples drawn from parametric distributions as in the case of the baselines, or images from the *friendly neighborhood* input dataset as in the case of Spider GAN. Table 8 also shows the relative increase in FID and KID compared to those obtained when unaltered samples drawn from p_Z are provided as input to the generator (cf. Table 2 of the *Main Manuscript*). Across all the datasets considered, we observe that Spider GAN variants with the *friendliest neighbor* input result in a performance comparable with the best-case baselines in terms of FID and KID. However, the baselines GAN with the non-parametric or gamma-distributed priors, which are designed to minimize the interpolation error [15, 16], and consequently, result in lower relative change in the scores. The results suggest that, while Spider GAN is superior to Gaussian latent spaces, a trade-off exists between the interpolated image quality offered by non-parametric or gamma priors, and the overall superior performance offered by Spider GAN. A detailed discussion on the input-space control over the generated images is discussed in the context of Spider StyleGAN2-ADA in Appendix D.5.1

D.2.3 Impact of Diversity and Dataset Bias on Spider GANs

The *friendly neighbourhood* of a target in SpiderGAN is chosen based on the SID metric, which compares the distance between data manifolds. SpiderGAN does not enforce image-level structure to learn pairwise transformations. We therefore expect that the diversity of the source dataset (such as racial or gender bias) should not affect the diversity in the learnt distribution. To demonstrate this, consider the task of learning Ukiyo-E faces dataset with CelebA dataset as input. We consider three variants of CelebA – (i) The entire dataset of 2×10^5 images, comprising an even split of the *male* and *females* classes; (ii) Only the *female* class comprising 10^5 images; and (iii) A simulated imbalance, created by including the entire *male* class and 200 images from the *female* class. The input resolution is 64×64, while the output resolution is set to 128×128. The models are trained using the DCGAN architecture with hyperparameters as described in Appendix C.1. All the models are trained for 10^5 generator iterations.

The images output by the Spider GAN model in each case are presented in Figure 21 (a.1-a.3). We did not observe bias in the images generated by the three models. To demonstrate this further, we compared the Spider GAN outputs for the same 20 samples of the *female* class images provided as input (cf. Figure 21 (a)). The results indicate that, while correspondence between images is not learnt, the bias in the source dataset of the generator in SpiderGAN does not affect the target diversity. The bias in these datasets is neither leveraged, nor exemplified by Spider GAN.

D.2.4 Mode Coverage in Spider GANs

In order to evaluate the mode coverage in Spider GAN learning, consider the *partial MNIST* experiment proposed by Zhong *et al.* [32] involving the 11-class augmented Fashion-MNIST dataset consisting of an additional 100 images drawn from from the *digit 1* class of MNIST. We train SpiderGAN on the Fashion-MNIST dataset with the CAE architecture (cf. Appendix D.1). We consider two input datasets: CIFAR-10 and Tiny-ImageNet.

In order to evaluate mode coverage, the trained GAN generators are compared on the ability to faithfully generate samples from the underrepresented *digit 1* class. For evaluation, a 11-class fully-connected classifier is trained on the augmented dataset consisting of all 10 classes from Fashion-MNIST and the entire *digit 1* class from MNSIT. Following the approach presented in [32], the GANs are evaluated by sampling a batch of 9×10^5 images, and computing the number of instances of *digit 1* generated, as indicated by the output of the classifier. We compare against the DCGAN, AdaGAN [33] and the GAN with mixture of generators (MixGAN) [32]. The images from *digit class 1* generated by the Spider GAN variants are presented in Figure 9, while Table 9 summarizes the performance of the baseline and Spider GAN models. The results highlight the need for class diversity in the input dataset. When SpiderGAN is trained with CIFAR-10, consisting of fewer classes than the target, the minority *digit 1* class is poorly represented. On the other hand, for Spider GAN with Tiny-ImageNet or CelebA as the input, the minority class is generated faithfully.

D.2.5 Learning the Identity Mapping

Based on the intuition that GAN generators perform entropy minimization [34], we expect the generator to learn an identity mapping when the same dataset is provided as both input and output. To validate this, we consider the Fashion-MNIST learning task with the DCGAN architecture. We considered all four combinations of adding noise to the input or target datasets. The learnt input-output pairs are presented in Figure 22. In all four scenarios, although pairwise consistency is not explicitly enforced, it was discovered by Spider GAN, resulting in a GAN generator that approximates an identity function. When the input and output datasets are both noisy, the generator attempts to retain the noise in the generated images. However, when the input dataset is clean but the target dataset incorporates noise, artifacts are introduced in the generated images as the models attempts to create noise (which has a higher entropy than the dataset).

Table 9. Mode coverage of Spider GAN in comparison to baseline GANs on the *Fashion-MNIST and partial MNIST* experiment. The * indicates values reported by Zhong *et al.* [32]. The measure *#1s* indicates the number of the samples from the *digit class* 1 predicted in a batch of 9×10^5 samples drawn the generator. *Avg. Prob.* denotes the average classification probability of *digit class 1* samples output by a pre-trained classifier. Spider GAN trained with an input dataset that posses higher diversity than the target, such as Tiny-ImageNet, outperforms the baselines.

Measure ($\uparrow$)	DCGAN*	AdaGAN*	MixGAN*	Spider GAN (CIFAR-10 Source)	Spider GAN (Tiny-ImageNet Source)
#1s	13	60	289	201	**345**
Avg. Prob.	0.49	0.45	0.69	0.81	**0.89**

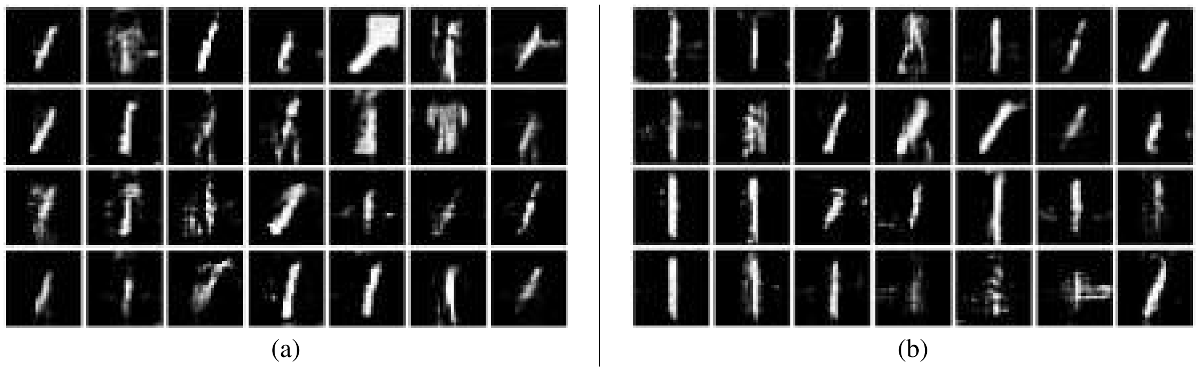

Figure 9. Images from the *digit class* 1 generated by Spider GAN with input images drawn from (a) CIFAR-10, and (b) Tiny-ImageNet datasets. The samples were identified based on the output of a pre-trained 11-class classifier network. Spider GAN with an input class diversity lower than the target (CIFAR-10 dataset) generated images of inferior quality in comparison to the Spider GAN trained on a more diverse input dataset such as Tiny-ImageNet.

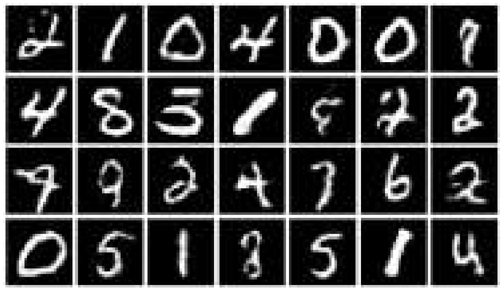
(a) Gaussian input

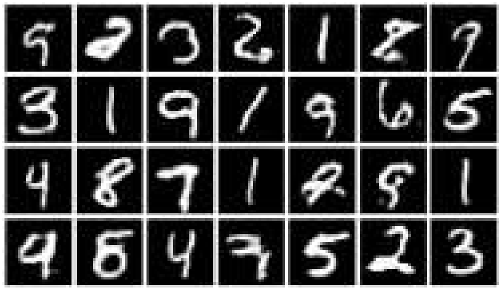
(b) Gamma input

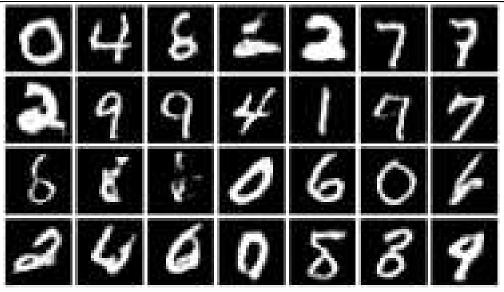
(c) Non-Parametric input

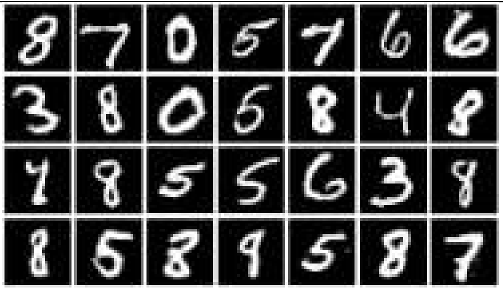
(d) Fashion-MNIST input

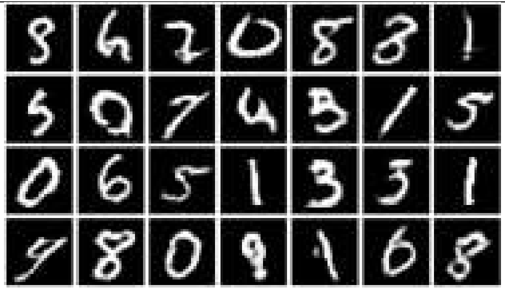
(e) SVHN input

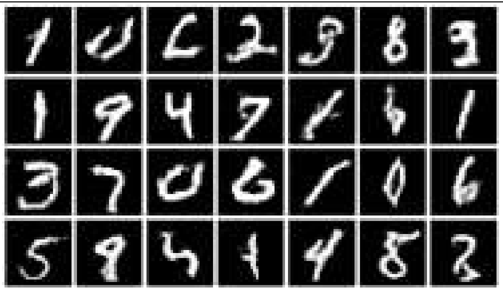
(f) CIFAR-10 input

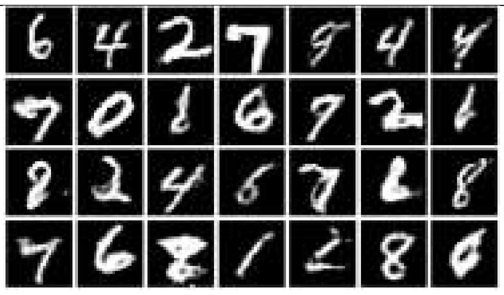
(g) Tiny-ImageNet input

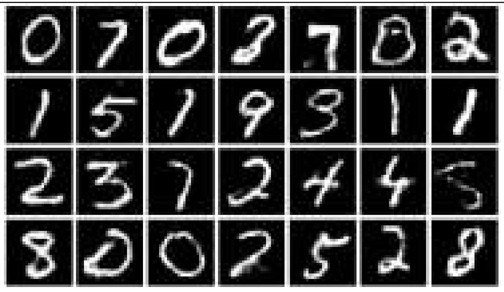
(h) CelebA input

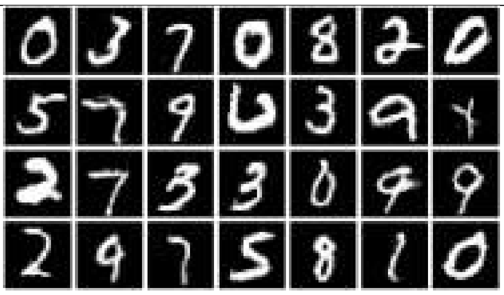
(i) Ukiyo-E Faces input

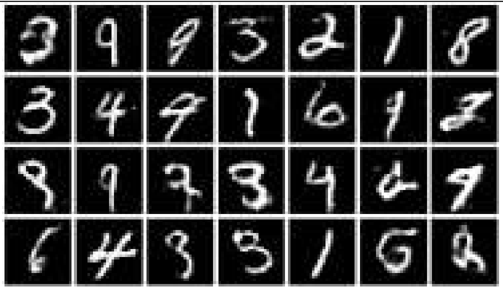
(j) LSUN-Churches input

Figure 10. Images generated by the baseline GAN and Spider GAN for various input distributions, with MNIST being the target. Spider GAN trained with Fashion-MNIST input (the friendliest neighbor of MNIST as identified by SID) generates sharper output images.

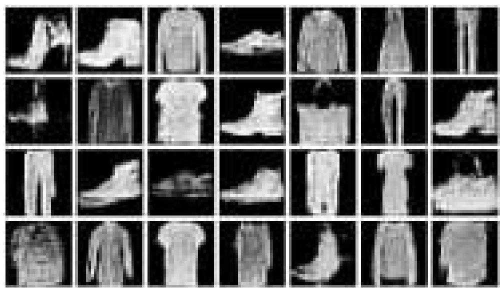
(a) Gaussian input

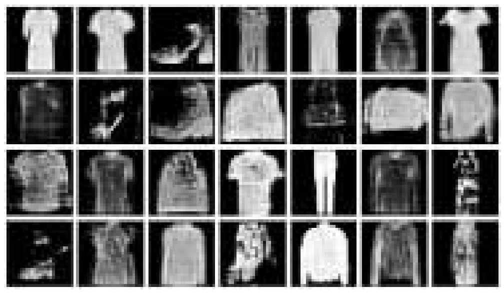
(b) Gamma input

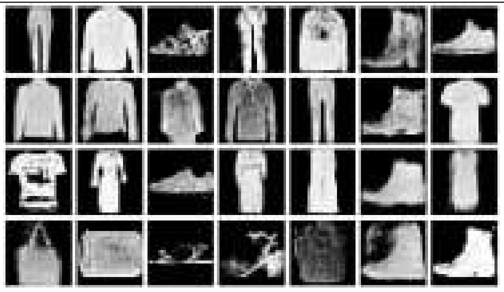
(c) Non-Parametric input

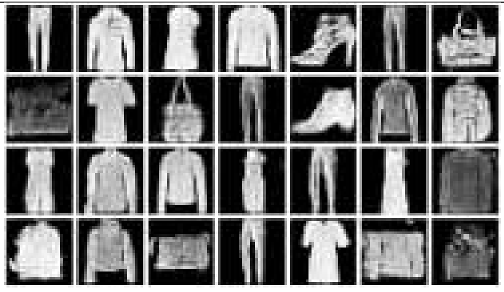
(d) MNIST input

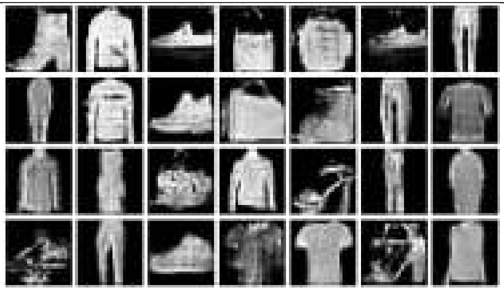
(e) SVHN input

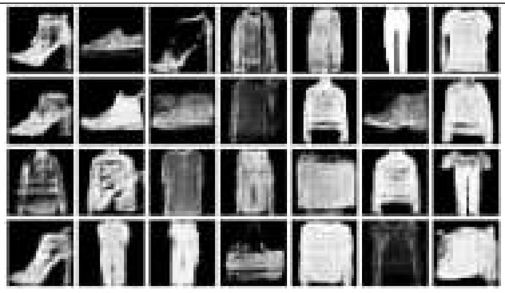
(f) CIFAR-10 input

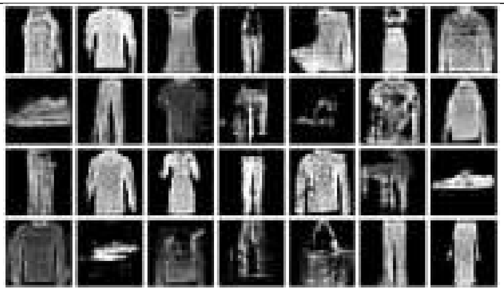
(g) Tiny-ImageNet input

(h) CelebA input

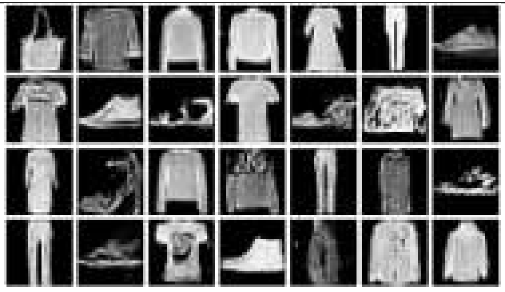
(i) Ukiyo-E Faces input

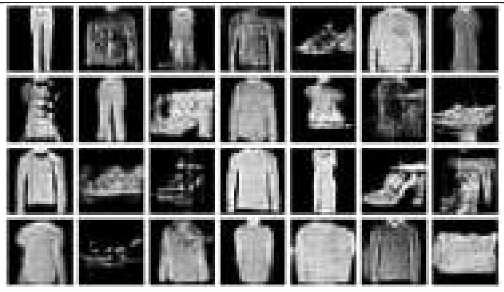
(j) LSUN-Churches input

Figure 11. Images generated by the baseline GAN and Spider GAN for various input distributions, with Fashion-MNIST chosen as the target. A poor choice of the input distribution results in a suboptimal generator that outputs low-quality images. For instance, the output generated for inputs coming from CelebA or a non-parametric distribution.

(a) Gaussian input

(b) Gamma input

(c) Non-Parametric input

(d) MNIST input

(e) Fashion-MNIST input

(f) CIFAR-10 input

(g) Tiny-ImageNet input

(h) CelebA input

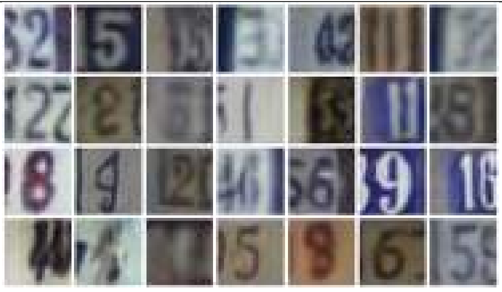
(i) Ukiyo-E Faces input

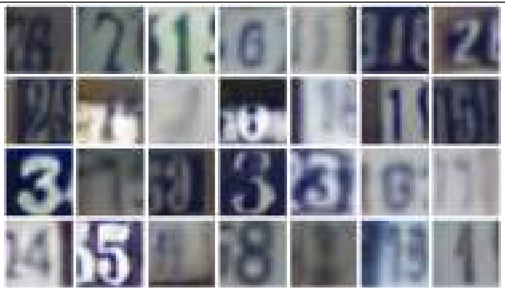
(j) LSUN-Churches input

Figure 12. Images generated by the baseline GAN and Spider GAN for various input distributions, when trained with SVHN as the target. A poor choice of the input distribution results in low-quality images output by the generator.

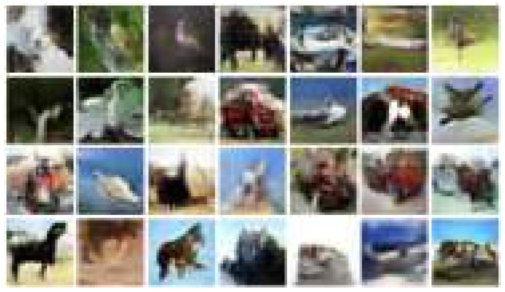
(a) Gaussian input

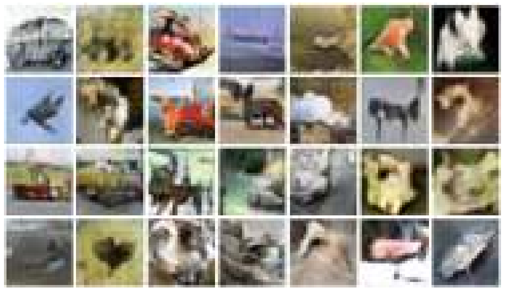
(b) Gamma input

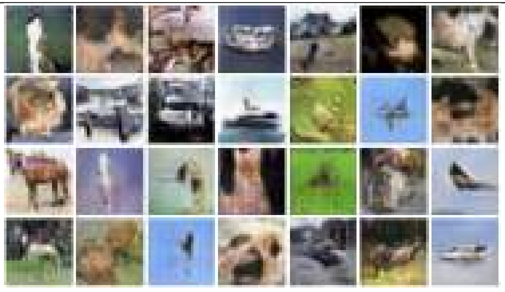
(c) Non-Parametric input

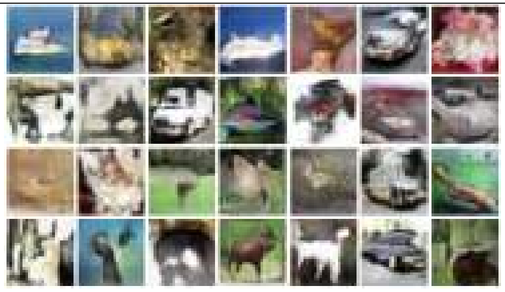
(d) MNIST input

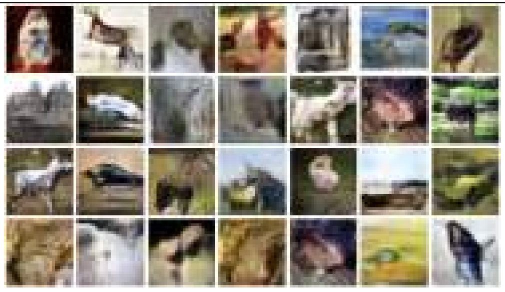
(e) Fashion-MNIST input

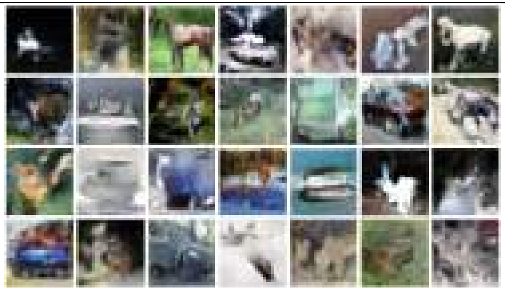
(f) SVHN input

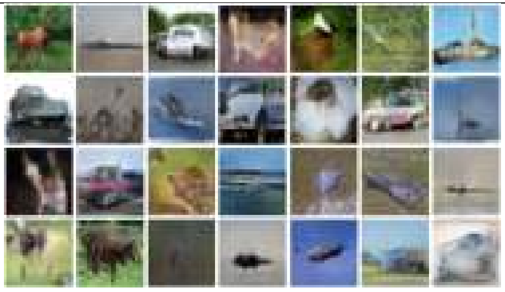
(g) Tiny-ImageNet input

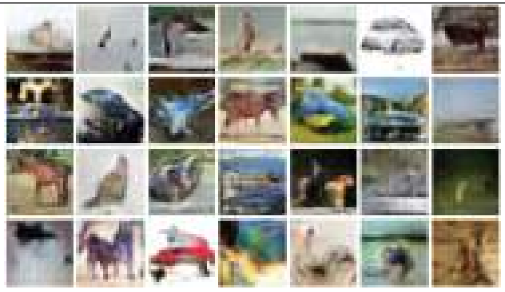
(h) CelebA input

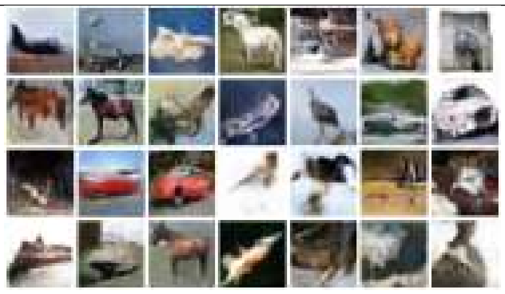
(i) Ukiyo-E Faces input

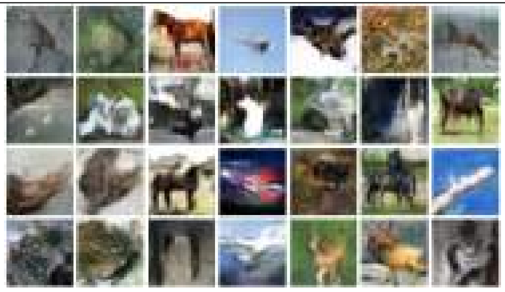
(j) LSUN-Churches input

Figure 13. Images generated by the baseline GAN and Spider GAN with CIFAR-10 as the target, for various input distributions. While some classes, such as the *horse*, *car* or *boat* are well generated by all GAN, neither the baseline GANs nor the Spider GANs are able to reliably learn all the classes in CIFAR-10.

(a) Gaussian input

(b) Gamma input

(c) Non-Parametric input

(d) MNIST input

(e) Fashion-MNIST input

(f) SVHN input

(g) CIFAR-10 input

(h) CelebA input

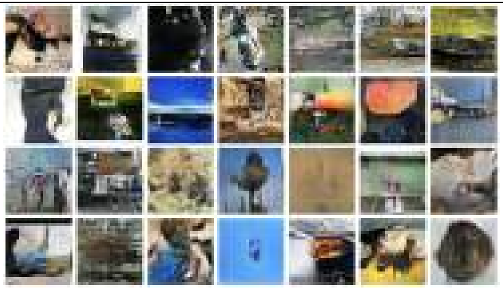
(i) Ukiyo-E Faces input

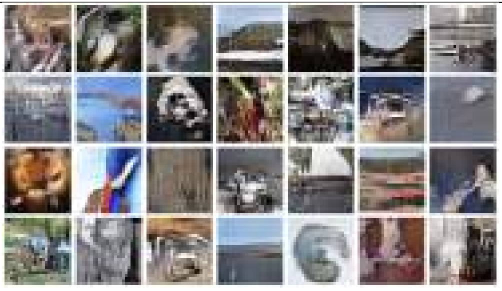
(j) LSUN-Churches input

Figure 14. Images generated by the baseline GAN and Spider GAN on Tiny-ImageNet as the target, for various input distributions as indicated. While Spider GAN approaches achieve a lower FID than the baselines on this task, none of the GAN variants generate realistic output images.

(a) Gaussian input

(b) Gamma input

(c) Non-Parametric input

(d) MNIST input

(e) Fashion-MNIST input

(f) SVHN input

(g) CIFAR-10 input

(h) Tiny-ImageNet input

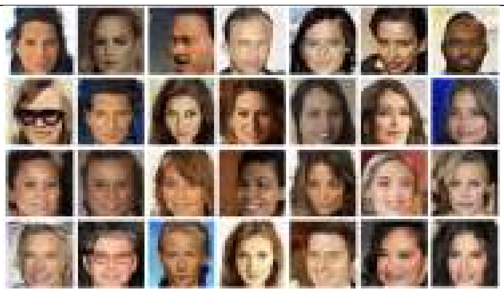

(i) Ukiyo-E Faces input

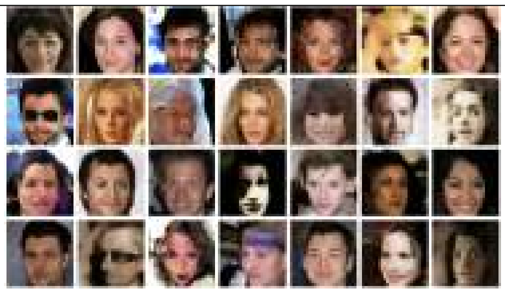

(j) LSUN-Churches input

Figure 15. Images generated by the baseline GAN and Spider GAN on the low resolution CelebA (64×64), given various input distributions. Images generated by Spider GAN trained with Tiny-ImageNet and Ukiyo-E Faces as the input outperform other GAN flavors.

(a) Gaussian input

(b) Gamma input

(c) Non-Parametric input

(d) MNIST input

(e) Fashion-MNIST input

(f) SVHN input

(g) CIFAR-10 input

(h) Tiny-ImageNet input

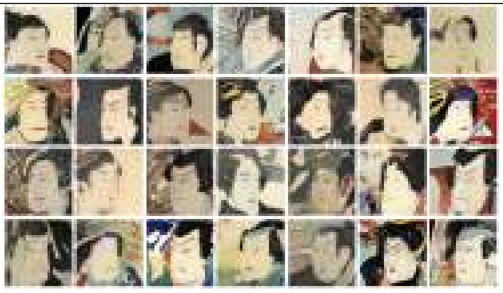
(i) CelebA input

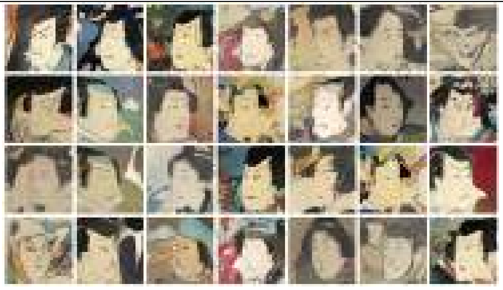
(j) LSUN-Churches input

Figure 16. Images generated by the baseline GAN and Spider GAN variants on the Ukiyo-E Faces for different inputs to the generator. Images generated by Spider GAN with Tiny-ImageNet or CelebA images as input results in sharper images in comparison to the baselines.

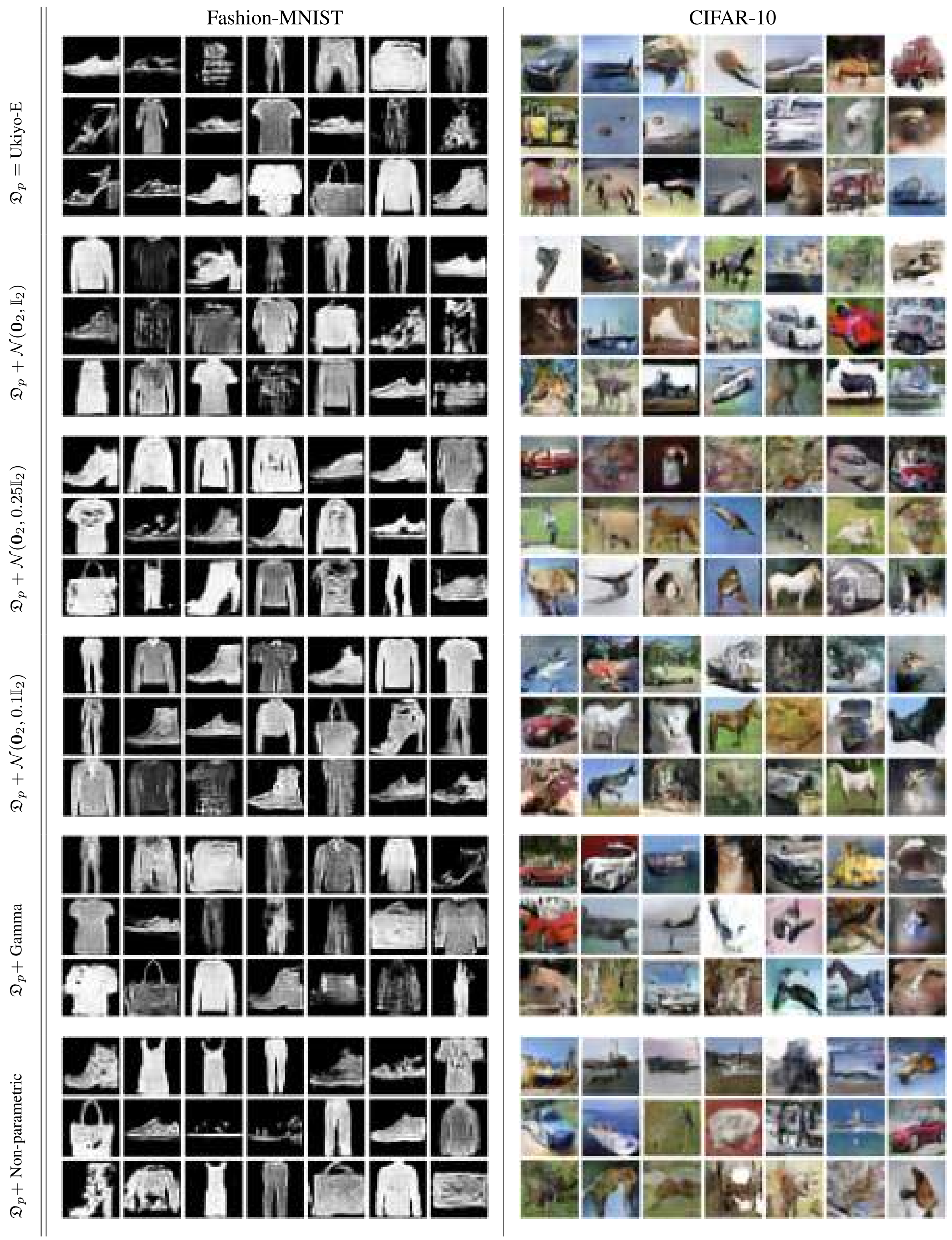
Fashion-MNIST
CIFAR-10
$\mathfrak{D}_p =$ Ukiyo-E
$\mathfrak{D}_p + \mathcal{N}(\mathbf{0}_2, \mathbb{I}_2)$
$\mathfrak{D}_p + \mathcal{N}(\mathbf{0}_2, 0.25\mathbb{I}_2)$
$\mathfrak{D}_p + \mathcal{N}(\mathbf{0}_2, 0.1\mathbb{I}_2)$
$\mathfrak{D}_p +$ Gamma
$\mathfrak{D}_p +$ Non-parametric

Figure 17. Images generated by Spider GAN on Fashion-MNIST and CIFAR-10, when trained with the Ukiyo-E Faces as input. Ukiyo-E Faces are perturbed mildly with various parametric noise sources to enhance the input diversity. Gaussian perturbations result in superior image quality compared to the rest.

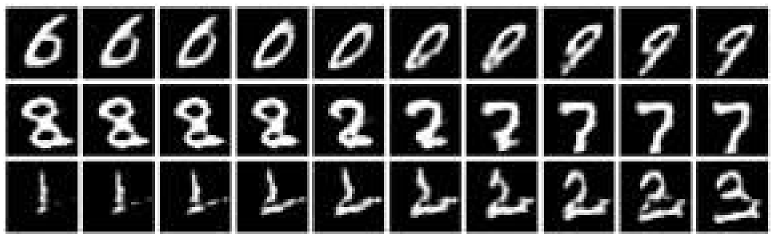
(a) Gaussian input

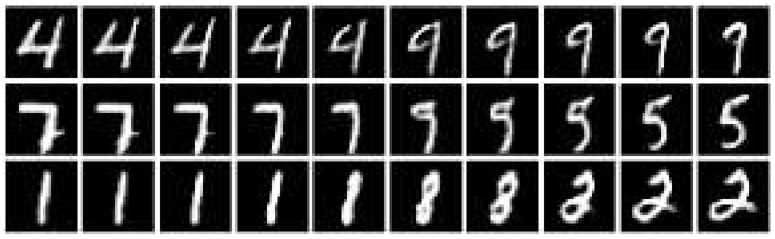
(d) Fashion-MNSIT input

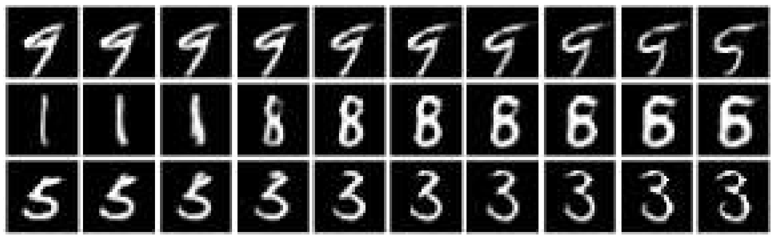
(b) Gamma input

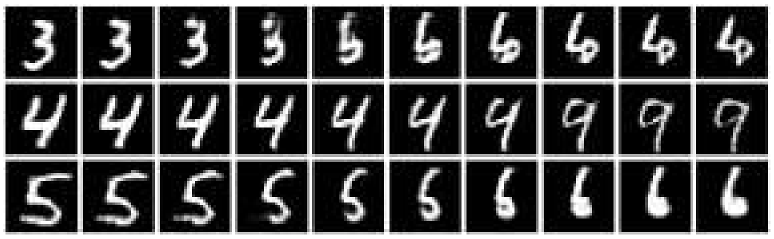
(e) CIFAR-10 input

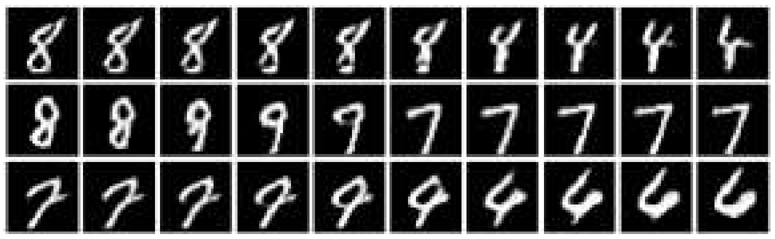
(c) Non-parametric input

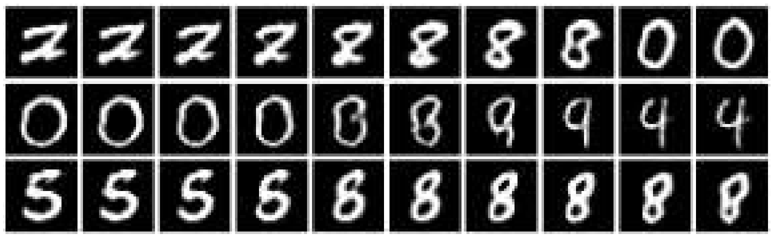
(f) Tiny-ImageNet input

Figure 18. Input-space interpolation on the baseline and Spider GAN variants trained on the MNIST dataset. Interpolation with Fashion-MNIST input for Spider GAN results in output images that transition smoothly, compared to the baselines.

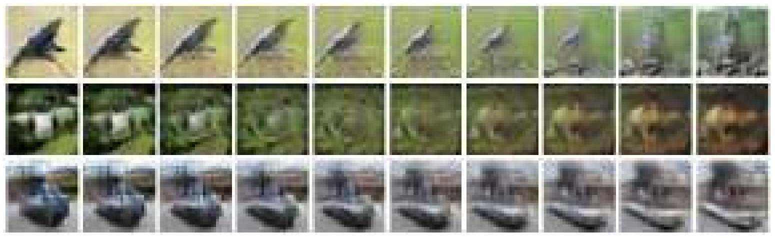
(a) Gaussian input

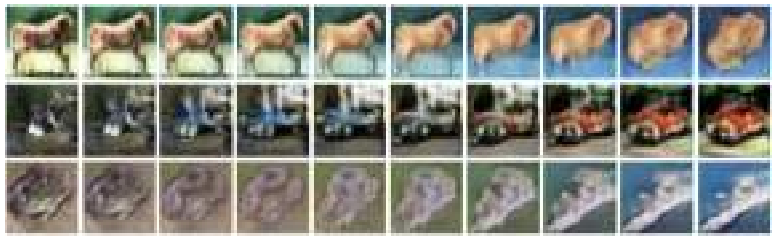
(d) Tiny-ImageNet input

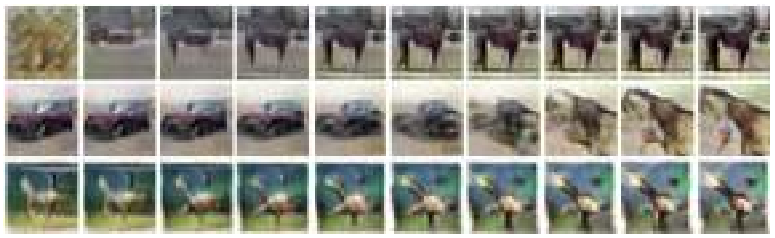
(b) Gamma input

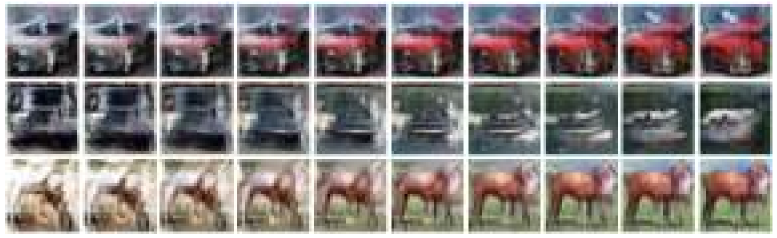
(e) CelebA input

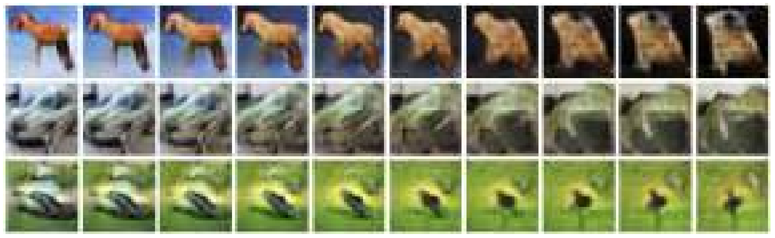
(c) Non-parametric input

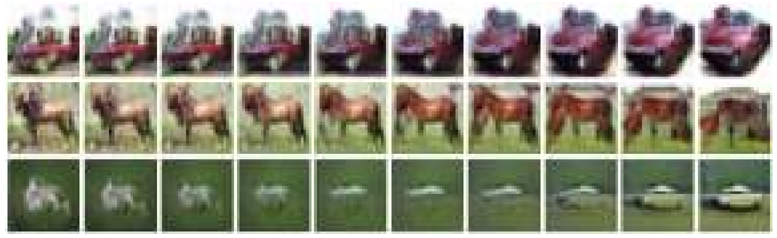
(f) LSUN-Churches input

Figure 19. (Color online) Input-space interpolation on the baseline GANs and Spider GAN trained on the CIFAR-10 dataset. Interpolation with Tiny-ImageNet input for Spider GAN result in output images of superior quality. However, all variants fail to create realistic images when provided with interpolated input samples.

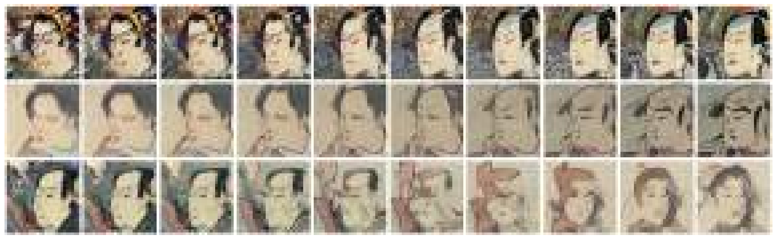
(a) Gaussian input

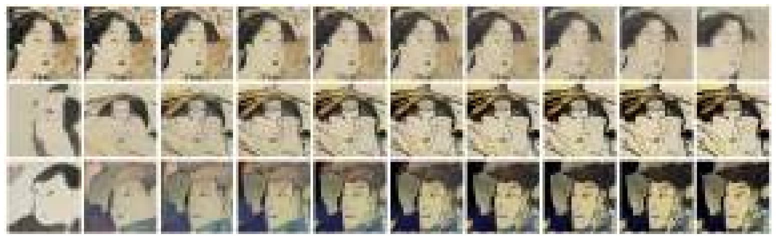
(b) Gamma input

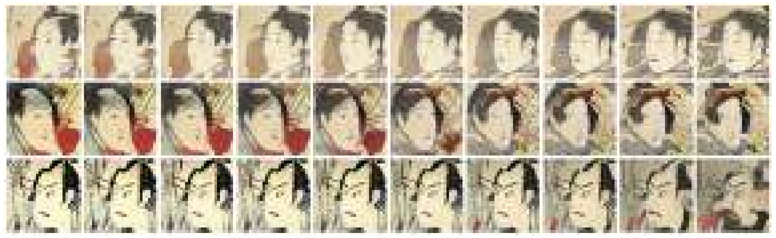
(c) Non-parametric input

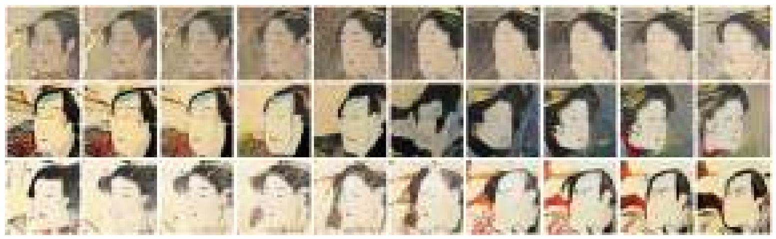
(d) Tiny-ImageNet input

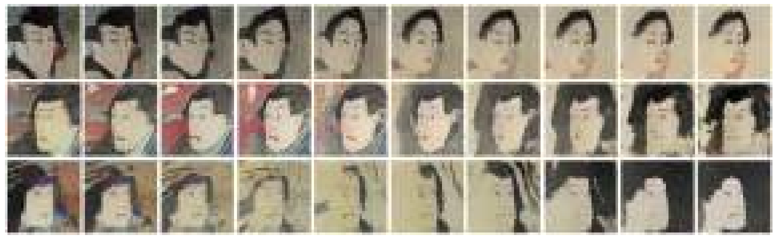
(e) CelebA input

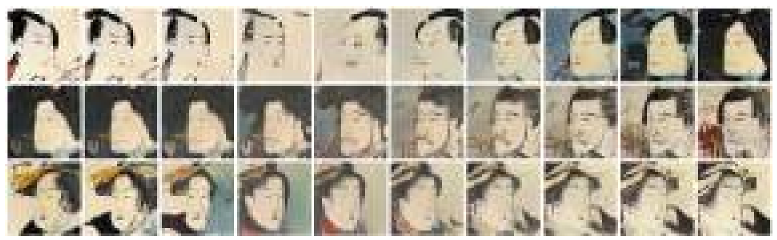
(f) LSUN-Churches input

Figure 20. (Color online) Input-space interpolation on the baseline and Spider GAN variants trained on the Ukiyo-E Faces. Interpolations with CelebA input for Spider GAN are the smoothest. Baseline variants result is sharp fluctuations in the orientation of the faces, which is indicative of a non-smooth generator in the output space.

(a) Input Samples from the *Female Class* of the source CelebA dataset.

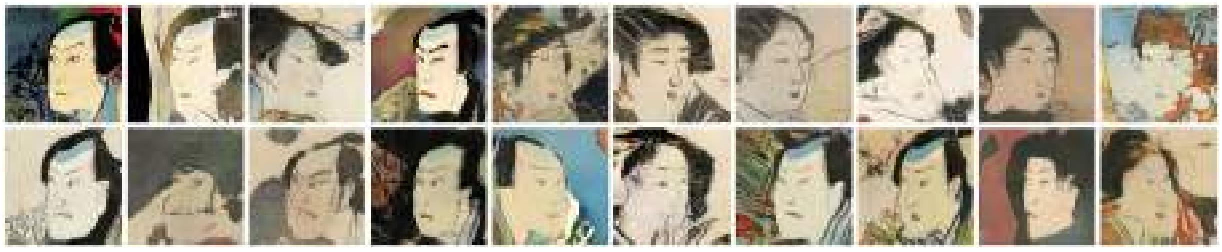

(a.1) Corresponding outputs for balanced source data.

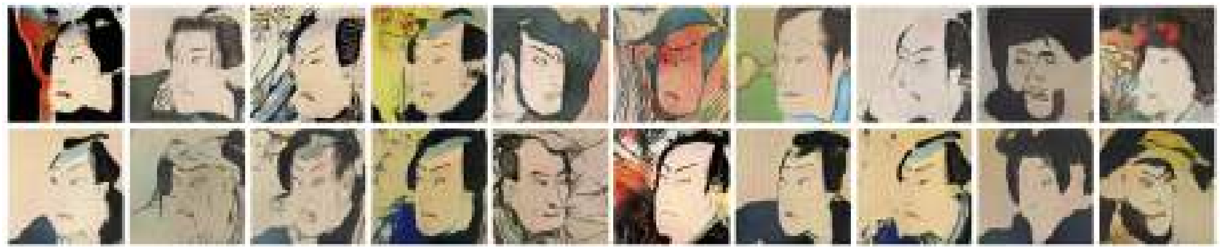

(a.2) Corresponding outputs for source data bias: 100% *Males* class + 0.2% *Female Class*.

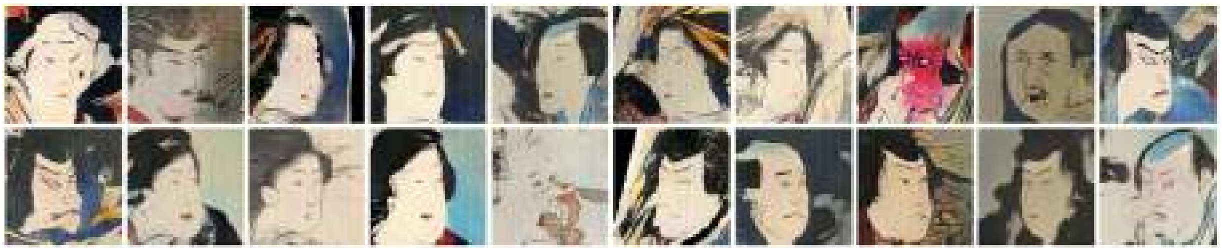

(a.3) Corresponding outputs for source data bias: 0% *Males* class + 100% *Female Class*.

Figure 21. Images generated by Spider GAN when trained on the Ukiyo-E Faces as the target dataset, with varying levels of bias simulated in the source CelebA dataset. The output images (a.1-a.3) correspond to the generator input with the same *Females class* CelebA images depicted. The bias in the input dataset does not carry over to the generator outputs in Spider GAN formulation. Irrespetive of the class imbalance in the source CelebA images, the generated Ukiyo-E Faces posses sufficient class diversity.

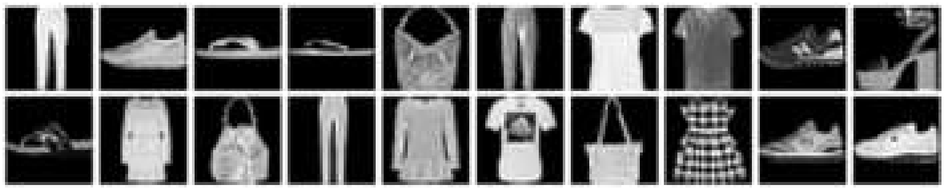

(a) Input Samples drawn from Fashion-MNIST.

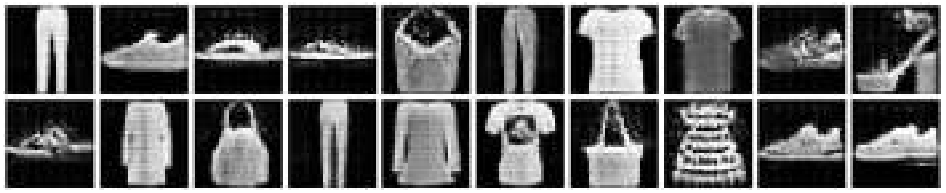

(a.1) Spider GAN ouptut when trained on noisy Fashion-MNIST as target.

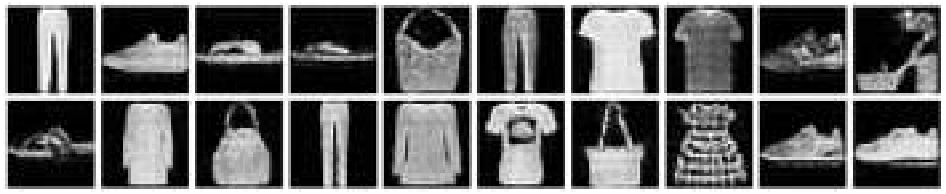

(a.2) Spider GAN output when trained on Fashion-MNIST as target.

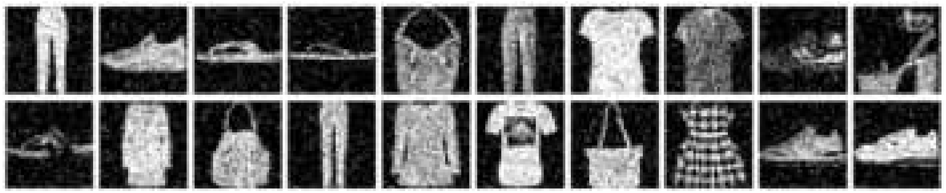

(b) Input Samples drawn from noisy Fashion-MNIST.

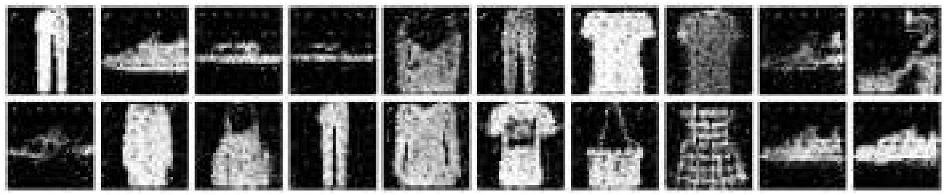

(b.1) Spider GAN ouptut when trained on noisy Fashion-MNIST as target.

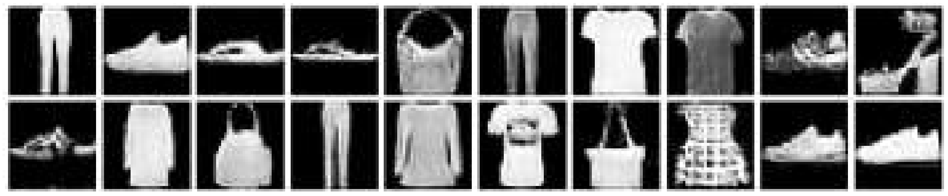

(b.2) Spider GAN output when trained on Fashion-MNIST as target.

Figure 22. Images generated by Spider GAN when trained on various combinations of noisy and clean Fashion-MNIST images provided as the input and output to the GAN. In all scenarios, although pairwise consistency was not explicitly enforced, it was discovered by Spider GAN network. When the input and output datasets are (a.2) both clean, or (b.1) both noisy, the generator attempts to learn an identity mapping. When the input dataset is clean but the target dataset incorporates noise (a.1), we observe artifacts in the generated images. SpiderGAN with a noisy input dataset and clean target samples learns a denoising network.

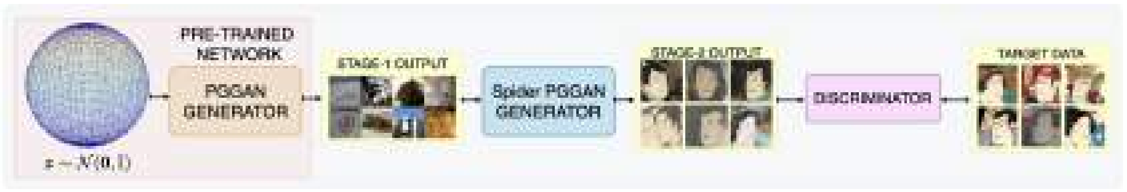

Figure 23. Spider GAN based progressively growing GAN (PGGAN) architecture. The output distribution of PGGAN trained on Tiny-ImageNet data is provided as input to the second Spider PGGAN stage that is trained to learn a high-resolution, small-sized dataset such as Ukiyo-E Faces.

D.3. Class-conditional Spider GAN

We present a *Spider* counterpart to the auxiliary classifier GAN (ACGAN [35]) formulation, entitled Spider ACGAN. In Spider ACGAN, the discriminator not only provides a *real versus fake* classification of its input, but also provides a prediction of the class from which the sample is drawn. The discriminator is trained to minimize both the WGAN loss with the R_d penalty [18], and the classification cross-entropy loss. We consider two variants of the generator, one without class information, and the other with the class label provided as a fully-connected embedding to the input layer. The Spider ACGAN variants are compared with the un-conditioned Spider GAN baseline. We present experiments on learning Fashion-MNIST dataset with MNIST as the input. The pairwise correspondences between the input and output images are presented in Figures 24-26. While Spider ACGAN without generator embeddings is superior to the baseline Spider GAN in learning class-level consistency, mixing between the classes is not eliminated. However, with the inclusion of class embeddings in the generator, the disentanglement of classes can be achieved in Spider ACGAN.

While this experiment demonstrates the feasibility of employing Spider GAN in class-conditional settings, scenarios involving mismatch between the number of classes in the input and output datasets, is a promising direction for future research.

D.4. Additional Experiments on Spider PGGAN

We now present additional experiments conducted with the Spider PGGAN architecture, and present the images generated by the Spider PGGAN variants. Figure 23 depicts the philosophy employed in a two-stage cascaded Spider PGGAN model considered in Section 5.1 of the *Main Manuscript*, where the input-stage PGGAN generated Tiny-ImageNet images, while the second Spider PGGAN stage transforms Tiny-ImageNet into Ukiyo-E Faces. Consider two extensions of the Spider PGGAN training algorithms: (a) The Spider PGGAN is trained on $32 \times 32 \times 3$ CIFAR-10 data with the input images drawn from the output of a PGGAN pre-trained on Tiny-ImageNet. Additionally, weights from PGGAN pre-trained on Tiny-ImageNet are transferred to Spider PGGAN for all layers but the first because the dimensionality in the first layer does not match. The trained model achieves an FID of 9.56, which is an improvement over the base Spider GAN trained on CIFAR-10 without the weight transfer. Images generated by Spider PGGAN with weight transfer are shown in Figure 28. This suggests that other network modifications and augmentations can be used in combination with the Spider GAN framework to improve the performance of PGGAN. (b) We train the Spider PGGAN with multiple cascade layers. The output of a Stage-I PGGAN pre-trained on Tiny-ImageNet is used to train a Spider PGGAN (Stage-II) to generate CIFAR-10 images. The output of the converged second stage model is used to generate high-resolution Ukiyo-E and MetFaces images (Stage-III). The final model achieves an FID of 45.32 on MetFaces (a 12% improvement over a single-stage Spider PGGAN), and 57.63 on Ukiyo-E Faces (a 10% improvement over single stage). The MetFaces images generated by the cascade network, juxtaposed the images generated by the baseline methods are provided in Figure 32. These results suggest that having multiple stages of pre-trained networks in the Spider PGGAN, and training incrementally results in superior performance than a single-stage Spider PGGAN.

D.5. Additional Experimental on Spider StyleGAN

The philosophy behind StyleGAN [11, 12] architectures run parallel to our proposed philosophy, where a *mapping* network is used to learn editable intermediate representations of the input noise distribution. A *synthesis* network subsequently transforms this representation into an image. The Spider GAN approach can be incorporated readily into any StyleGAN network, by replacing the input noise distribution to the mapping network with samples from the input dataset, drawn from a pre-trained GAN.

We trained the *Spider* variants of StyleGAN2, StyleGAN2-ADA [11] and StyleGAN3 [12] on the Ukiyo-E Faces, MetFaces, FFHQ, animal faces HQ Cats (AFHQ-Cats) dataset using the various combinations that included adaptive regularization and weight transfer. Across all experiments, two pre-trained networks were employed to generated the input dataset distribution

– (i) A StyleGAN2-ADA network trained on the AFHQ-Dogs dataset of resolution 32×32; and (ii) A StyleGAN2-ADA network trained on the Tiny-ImageNet dataset of resolution 32×32. The outputs are transformed based on the approach described in Appendix C.1. To generate higher-quality samples, we adopted the popular *truncation trick* [30] in sampling from the input-stage generator – The input-stage baseline generator is trained to transform samples drawn from the standard normal distribution to those coming from Tiny-ImageNet, or AFHQ-Dogs datasets. When generating the inputs to the cascaded SpiderGAN stage, samples are drawn from a truncated Gaussian, where a sample is re-drawn if it lies outside the $[-2, 2]^n$ hypercube (a 2σ interval). This was shown to improve the generator output quality at a small cost of marginally reduced sample diversity [30]. On the experiments on learning Ukiyo-E Faces, MetFaces, and FFHQ with cascaded Spider StyleGAN2-ADA, the truncation trick resulted in a 10% improvement in FID on the average. Figure 29 presents the images generated by these models considering baseline sampling and the truncation trick.

The comparison of FID and CSID$_m$ of the StyleGAN variants trained on FFHQ are provided in Table 10. Spider StyleGAN2-ADA with the Tiny-ImageNet input achieved an FID score on par with StyleGAN-XL, a model with three-fold higher network complexity. However, in terms of CSID$_m$, Spider StyleGAN2-ADA achieves state-of-the-art performance, which suggests that the diversity of images generated by Spider StyleGAN2-ADA is superior to that of StyleGAN-XL. The Spider StyleGAN3 model with weight transfer achieves a state-of-the-art FID of 3.07 on AFHQ-Cats, with one-fourth of the training iterations as the baselines. The accelerated convergence can be attributed to the superior *initialization* in the Spider GAN framework, as opposed to initializing with high-dimensional Gaussian inputs. Figures 30- 41 show the images generated by the various models and side-by-side comparison of the images generated by Spider StyleGAN and baseline variants.

D.5.1 Interpolating with Spider StyleGAN3

In order to better understand the control over representations that the *Spider* framework provides, we consider interpolation experiments on cascaded Spider StyleGAN2-ADA. A pre-trained SpiderStyleGAN2 with Gaussian distributed input and AFHQ-Dogs as output forms the input-stage network. The outputs of this network serve as the input to Spider StyleGAN2-ADA. As discussed in Section 5.2, we consider the following two interpolation schemes:

- Scheme-1, where interpolation is carried out between the AFHQ-Dogs images generated by the input-stage GAN, and subsequently fed to cascaded Spider GAN stage. Figures 42, 44 and 46 present the outputs of the first- and second-stage GANs, when trained on Ukiyo-E Faces, MetFaces and FFHQ images, respectively.
- Scheme-2, where linear interpolation is performed in the Gaussian space. The corresponding samples are used to generate AFHQ-Dogs images, which are fed as input to the Spider GAN stage. Figures 43, 45 and 47 show the intermediate AFHQ-Dogs and Spider GAN outputs for this configuration, when trained on Ukiyo-E Faces, MetFaces and FFHQ images, respectively.

Across all datasets, we observe that Scheme-1 results in superior control over the features, with gradual, fine-grained transitions between the images. On the other hand, images generated by Scheme-2 are affected by the known caveats of Gaussian-space interpolation [15, 16]. Interpolations of Gaussian-distributed points have a very low probability of lying on the Gaussian manifold. Consequently, the generated AFHQ-Dogs images, and the the subsequent target-dataset images possess unnatural discontinuities, appearing unrealistic. In the case of generating FFHQ and Ukiyo-E Faces, this results in the generation of noisy images at intermediate locations.

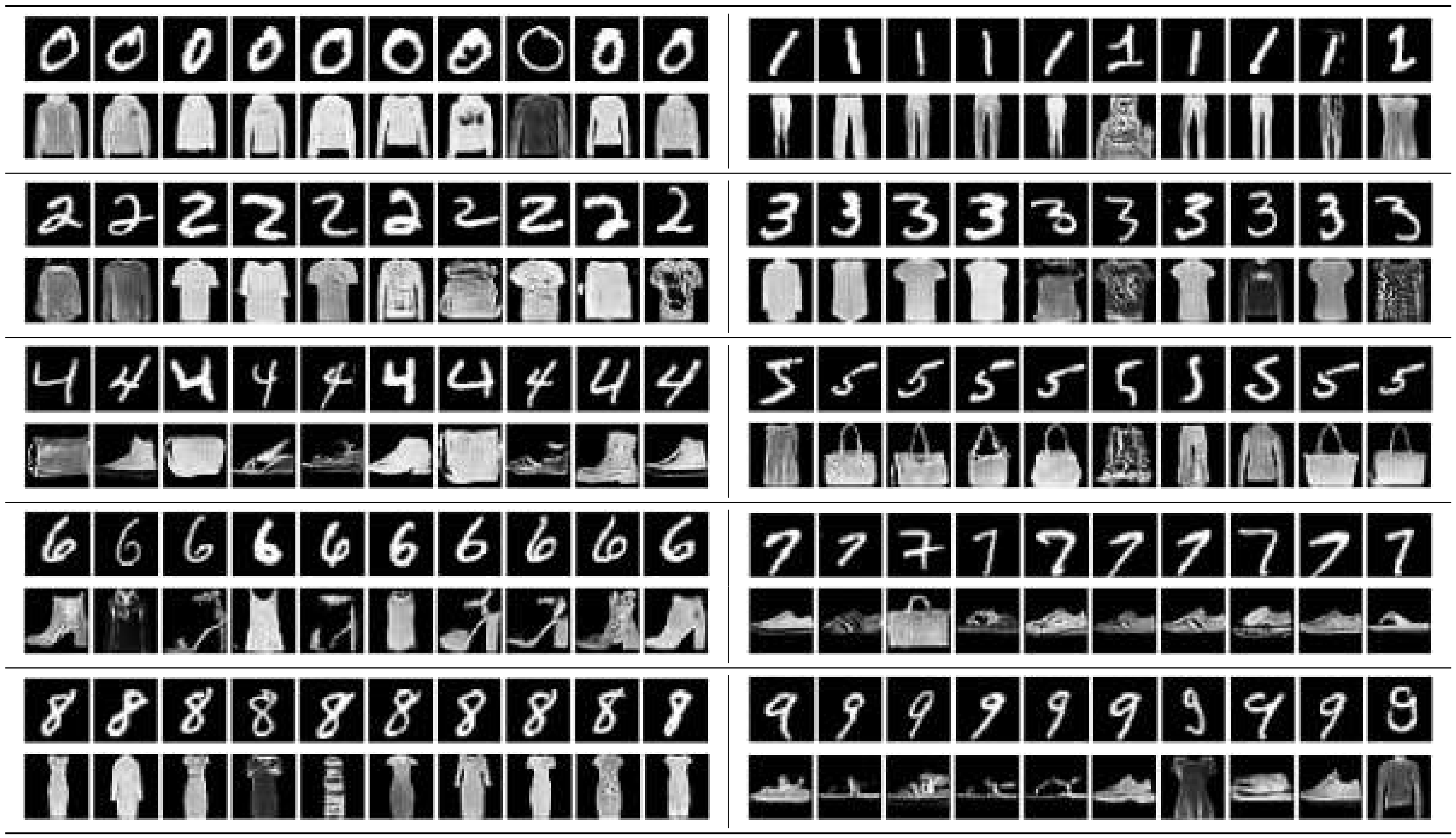

Figure 24. Images representing the class correspondence in a baseline Spider GAN where class embedding are not provided to the networks. While Style GAN learns to maps images based on image-level structure, there is overlap between classes.

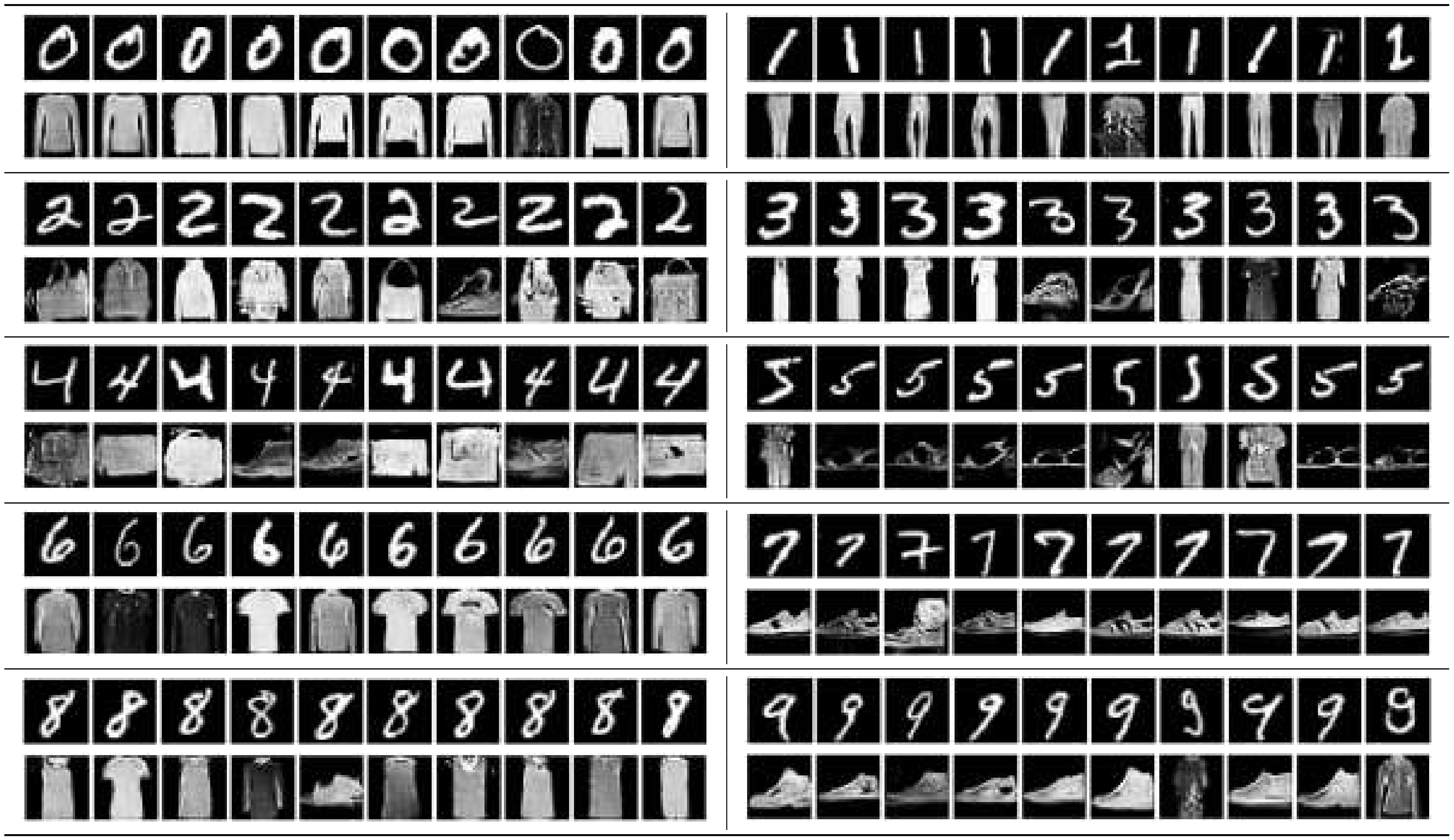

Figure 25. Images representing the class correspondence between the source and target data in a class-conditional Spider GAN where discriminator is modified to output the class label of the generated images. The Spider GAN generator is not provided class information, but is trained to minimize the classification accuracy. While the model's class-correspondence is superior to that of the baseline Spider GAN, class overlap is not eliminated.

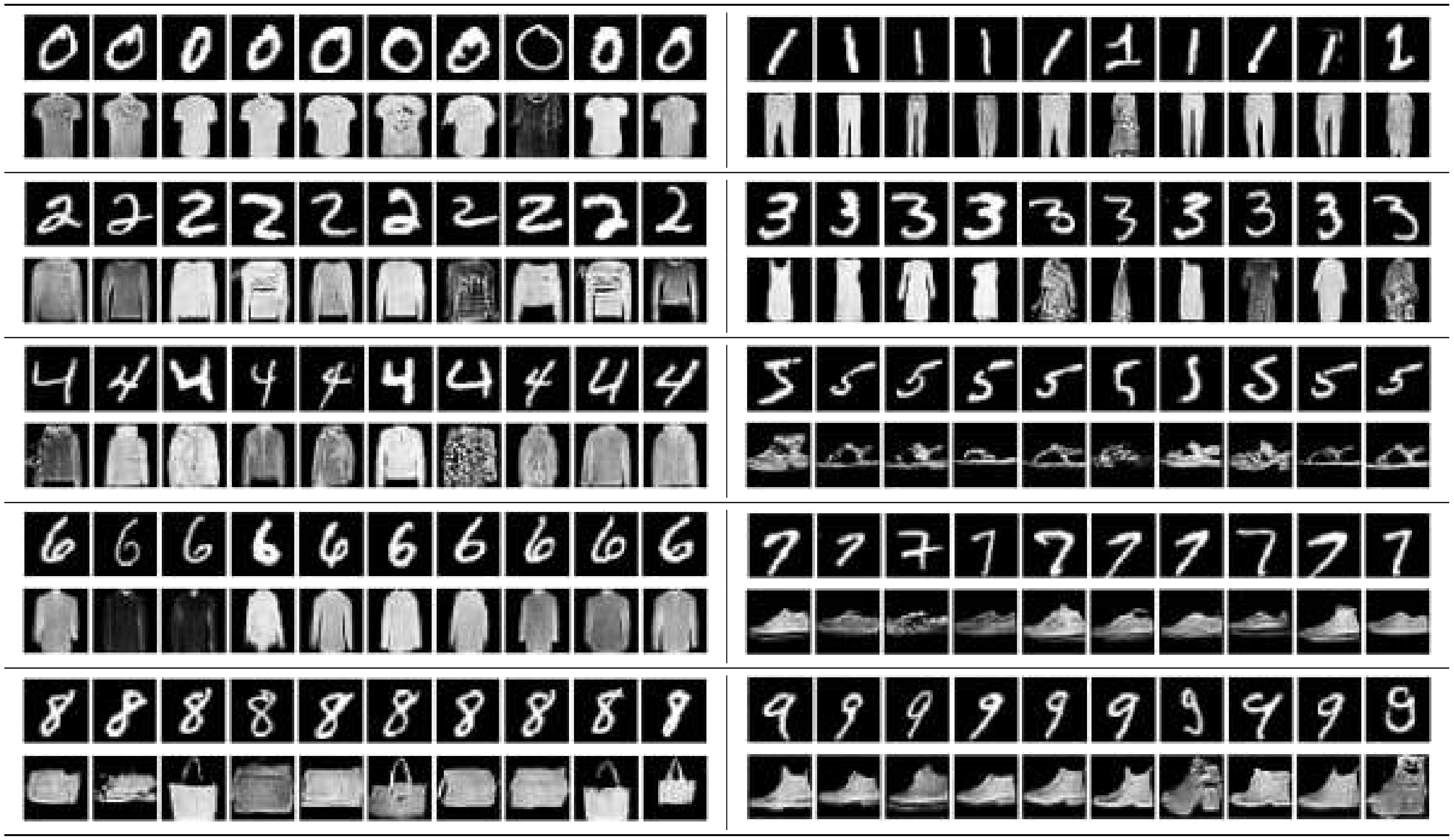

Figure 26. The class correspondence of the images generated by Spider ACGAN. The discriminator is modified to output the class label of the generated images, while the source class information is provided as an embedding layer to the generator. The Spider ACGAN model achieves superior class disentanglement in comparison to the baselines.

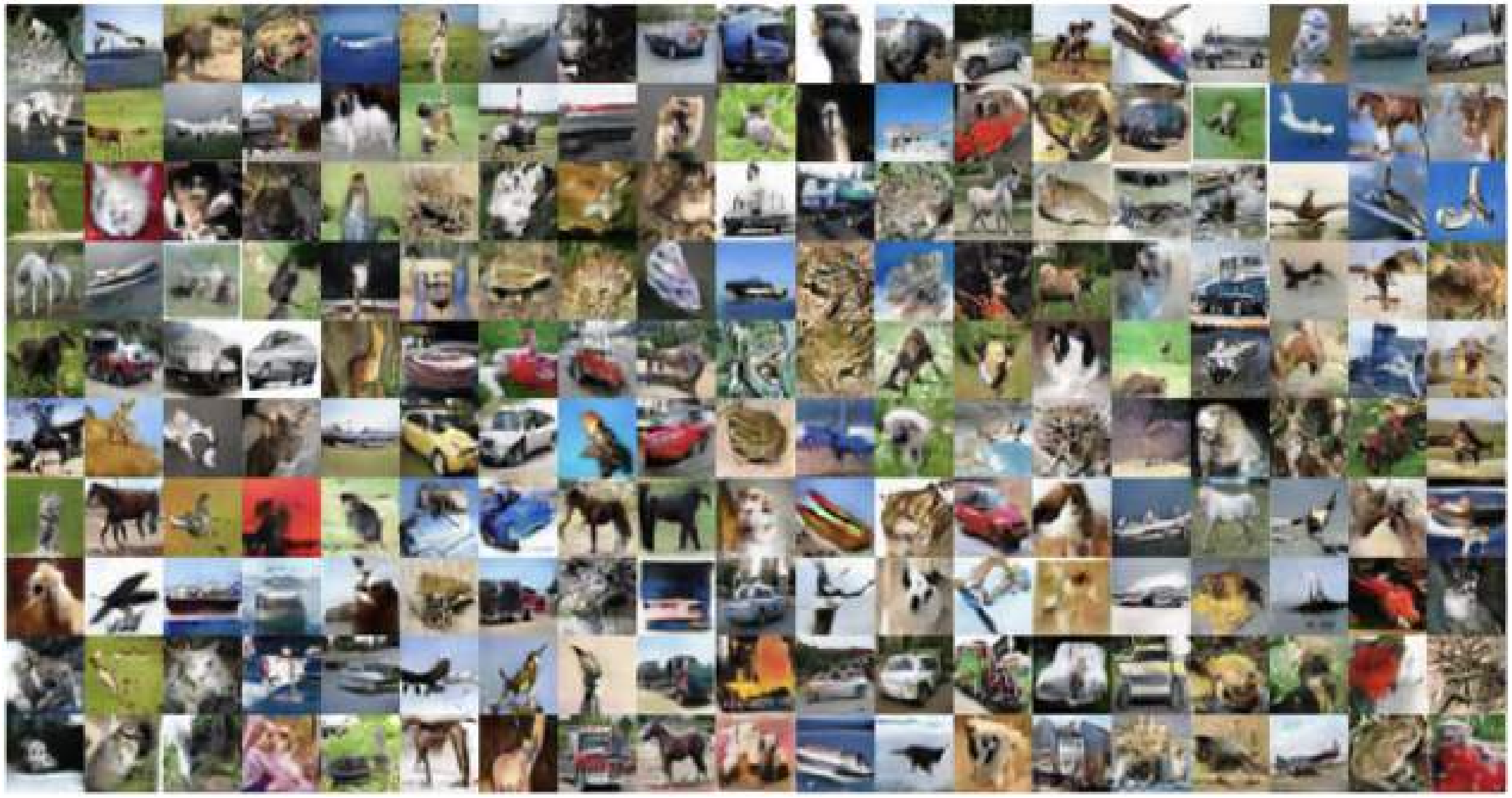

Figure 27. Images generated by Spider PGGAN with CIFAR-10 as the target, when trained with Tiny-ImageNet as input, which in turn, is the target for a PGGAN trained with Gaussian noise as the input.

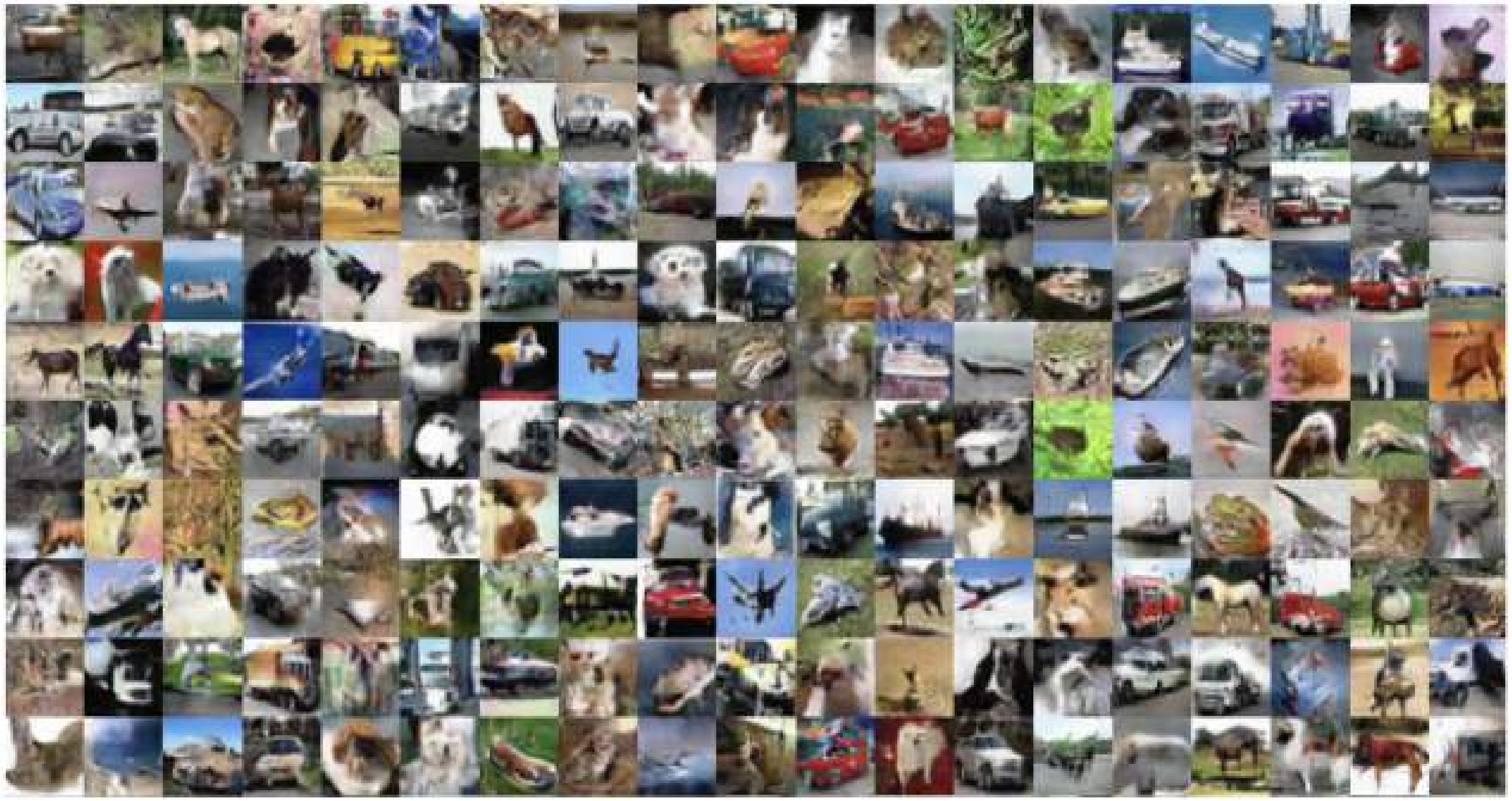

Figure 28. Images generated by Spider PGGAN with CIFAR-10 as the target, when trained with Tiny-ImageNet as the input, which in turn is drawn from a PGGAN trained with a Gaussian input. The weights of the Spider PGGAN are also initialized with the weights of the input PGGAN, resulting in faster training and superior output image quality.

Table 10. A comparison of StyleGAN2-ADA and StyleGAN3 variants, in terms of FID, KID and CSID$_m$, on learning FFHQ. A † indicates a reported score. Spider StyleGAN2-ADA performs on par with the state-of-the-art StyleGAN-XL (three fold higher network complexity) [36] in terms of FID and KID. However, Spider StyleGAN2-ADA variants achieved the best (lowest) CSID$_m$ scores, which suggests that the *Spider* variants learnt more diverse representations of the target dataset when compared against the baselines.

Architecture	Input	Clean-FID [10]	Clean-KID [10]	CSID$_m$
StyleGAN2-ADA [11]	Gaussian	2.70†	0.906×10^{-3}	2.65
StyleGAN3-T [12]	Gaussian	2.79†	1.031×10^{-3}	2.95
StyleGAN-XL [36]	Gaussian	**2.02**†	$\mathbf{0.287 \times 10^{-3}}$	3.94
Spider StyleGAN2-ADA (**Ours**)	TinyImageNet	$\underline{2.45}$	0.915×10^{-3}	**1.99**
Spider StyleGAN2-ADA (**Ours**)	AFHQ-Dogs	3.07	$\underline{0.795 \times 10^{-3}}$	$\underline{2.55}$
Spider StyleGAN3-T (**Ours**)	TinyImageNet	2.86	1.162×10^{-3}	3.25

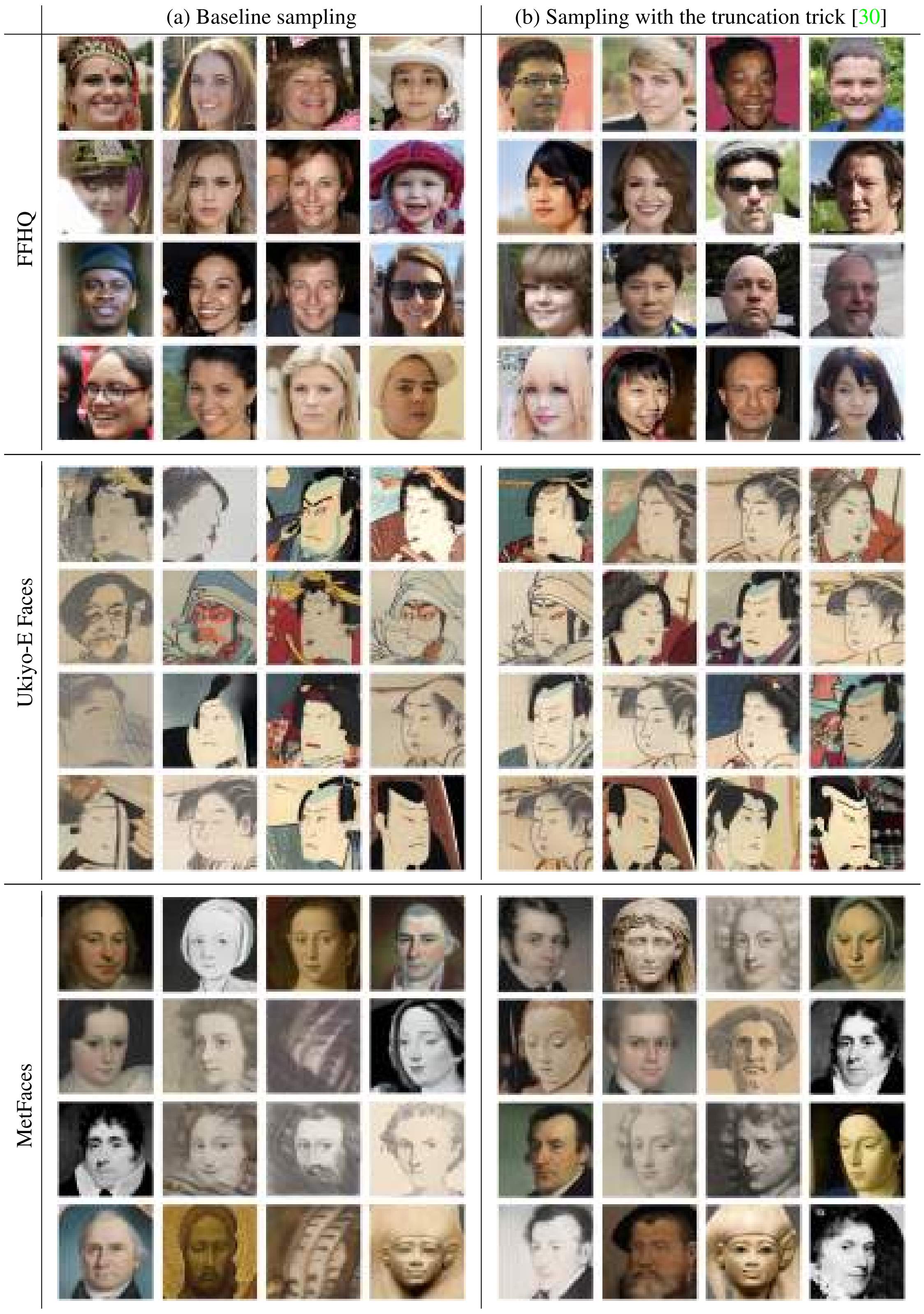

Figure 29. Images generated by cascaded Spider GAN variants when the Gaussian samples provided to the input-stage are (a) retained as-is; and (b) resampled when lying outside of the 2σ interval $[-2, 2]$ (*the truncation trick* [30]). Images generated using truncated input samples are of a superior visual quality. Baseline sampling results in distorted faces in the case of FFHQ and Ukiyo-E faces datasets, while on MetFaces, poor quality samples resulted in *alien* patterns.

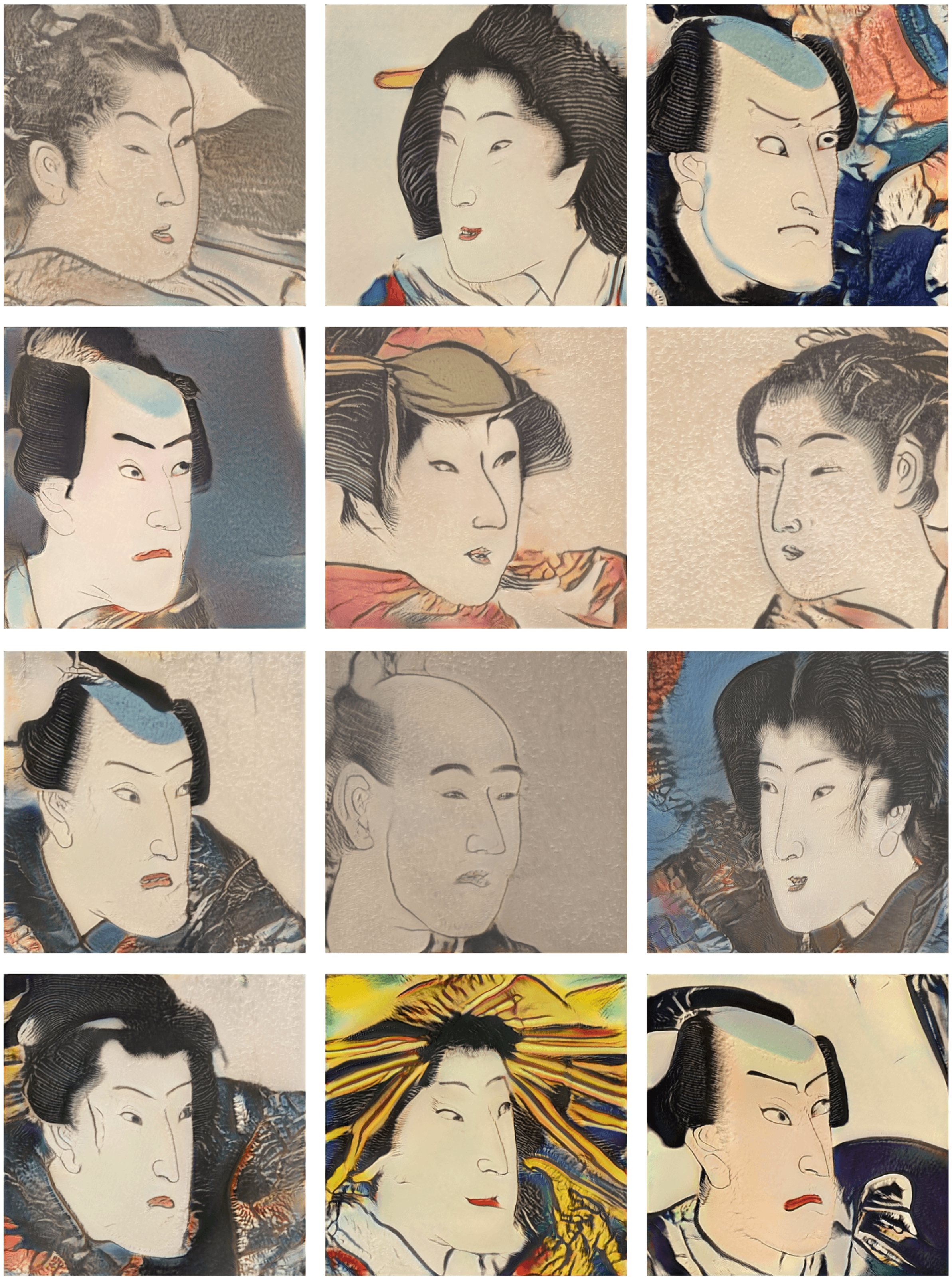

Figure 30. Ukiyo-E images generated by the *Spider* variant of StyleGAN2, trained on AFHQ-Dogs input. Since the AGFQ-Dogs dataset has relatively lower diversity than the target, the generated Ukiyo-E samples are visually sup-par compared to the performance of the baseline StyleGAN2-ADA.

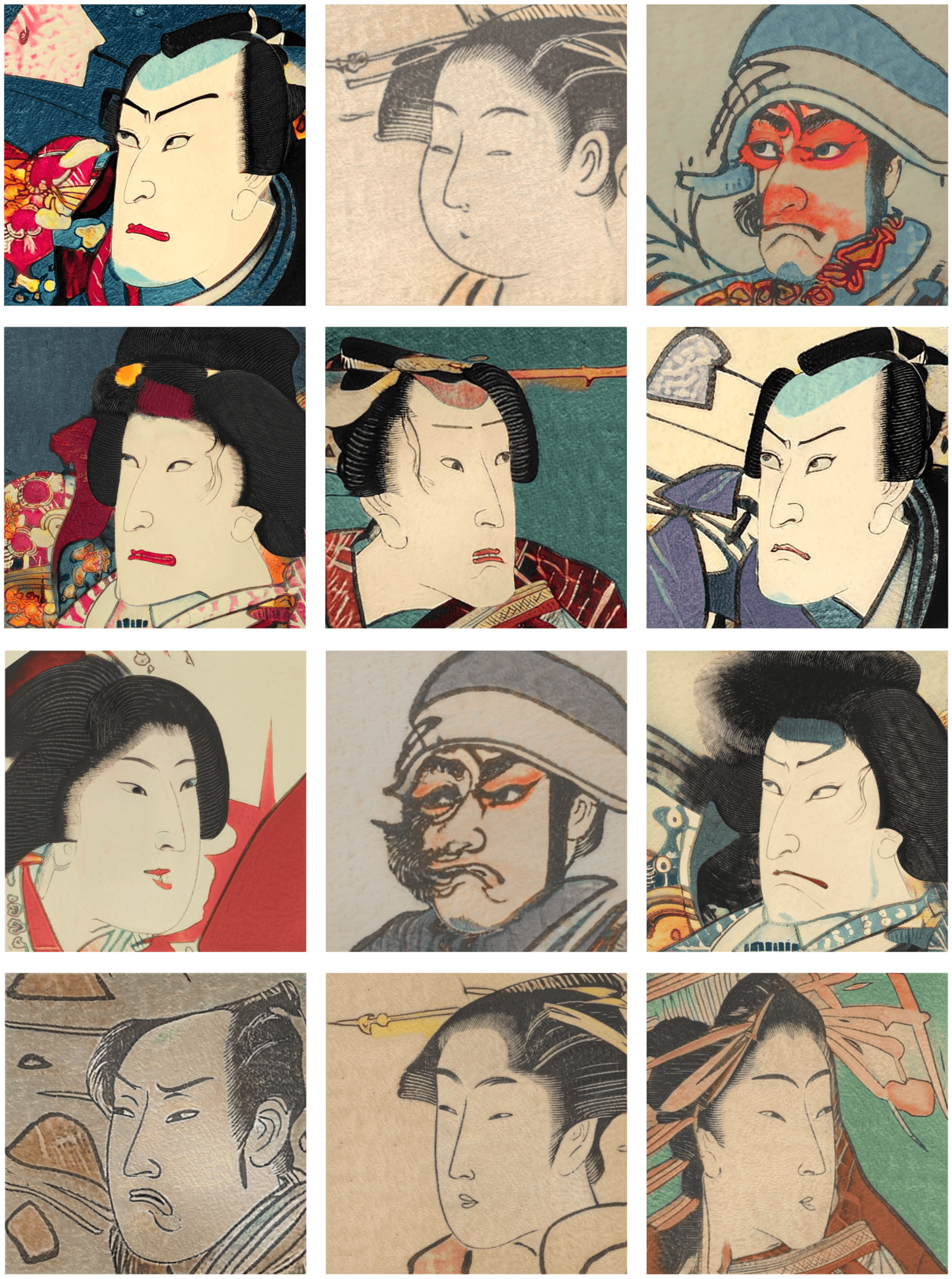

Figure 31. Ukiyo-E face images generated by the *Spider* variant of StyleGAN2, trained on Tiny-ImageNet input. The Spider variant achieves state-of-the-art FID of 20.44, compared to 26.74 of the baseline StyleGAN2-ADA (lower FID is better).

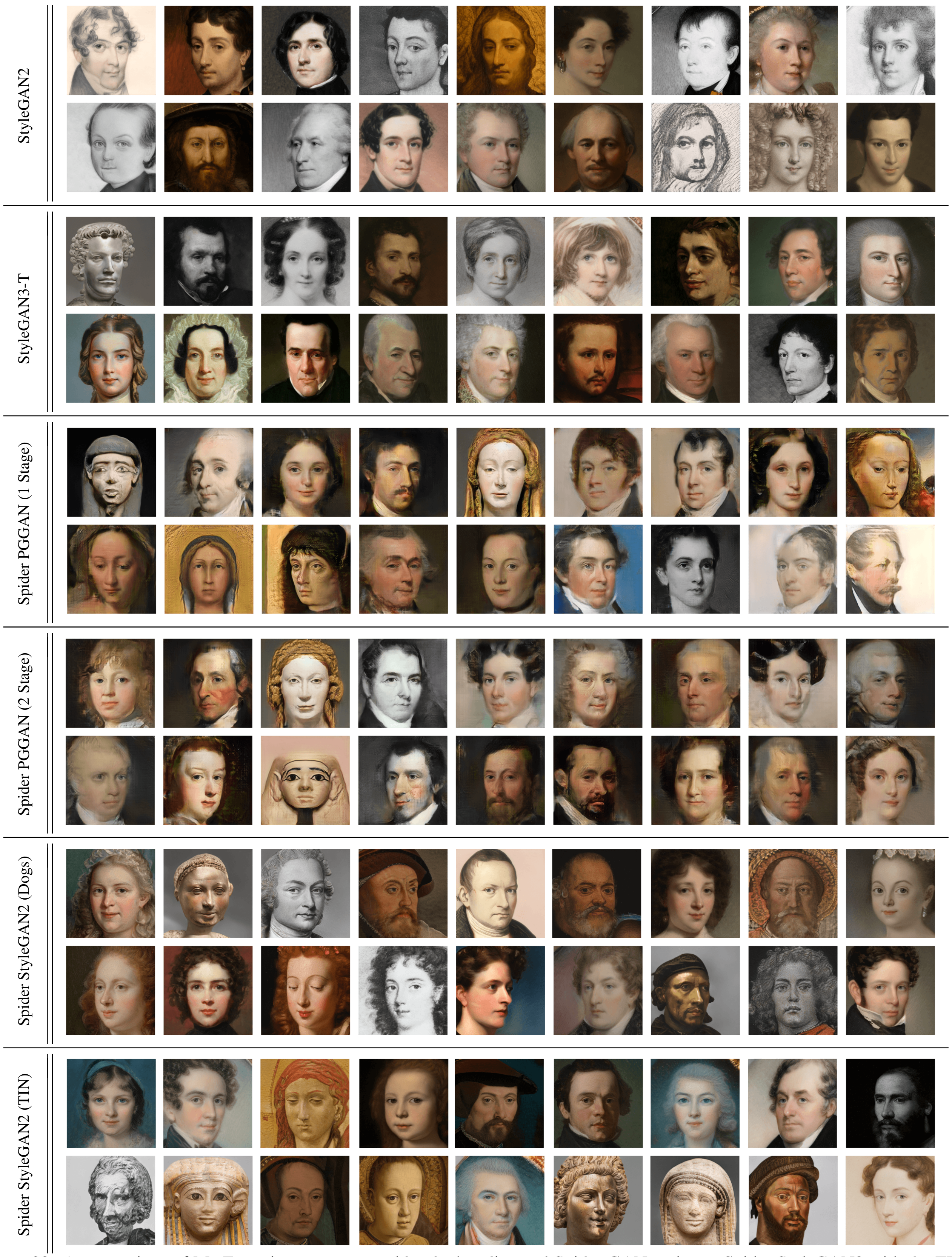

Figure 32. A comparison of MetFaces images generated by the baseline and Spider GAN variants. Spider StyleGAN2 with the TIny-ImageNet (TIN) input data outperforms all other variants, generating sharper and more diverse images, achieving a state-of-the-art FID of 15.60 as opposed to an FID of 18.75 achieved by StyleGAN2-ADA.

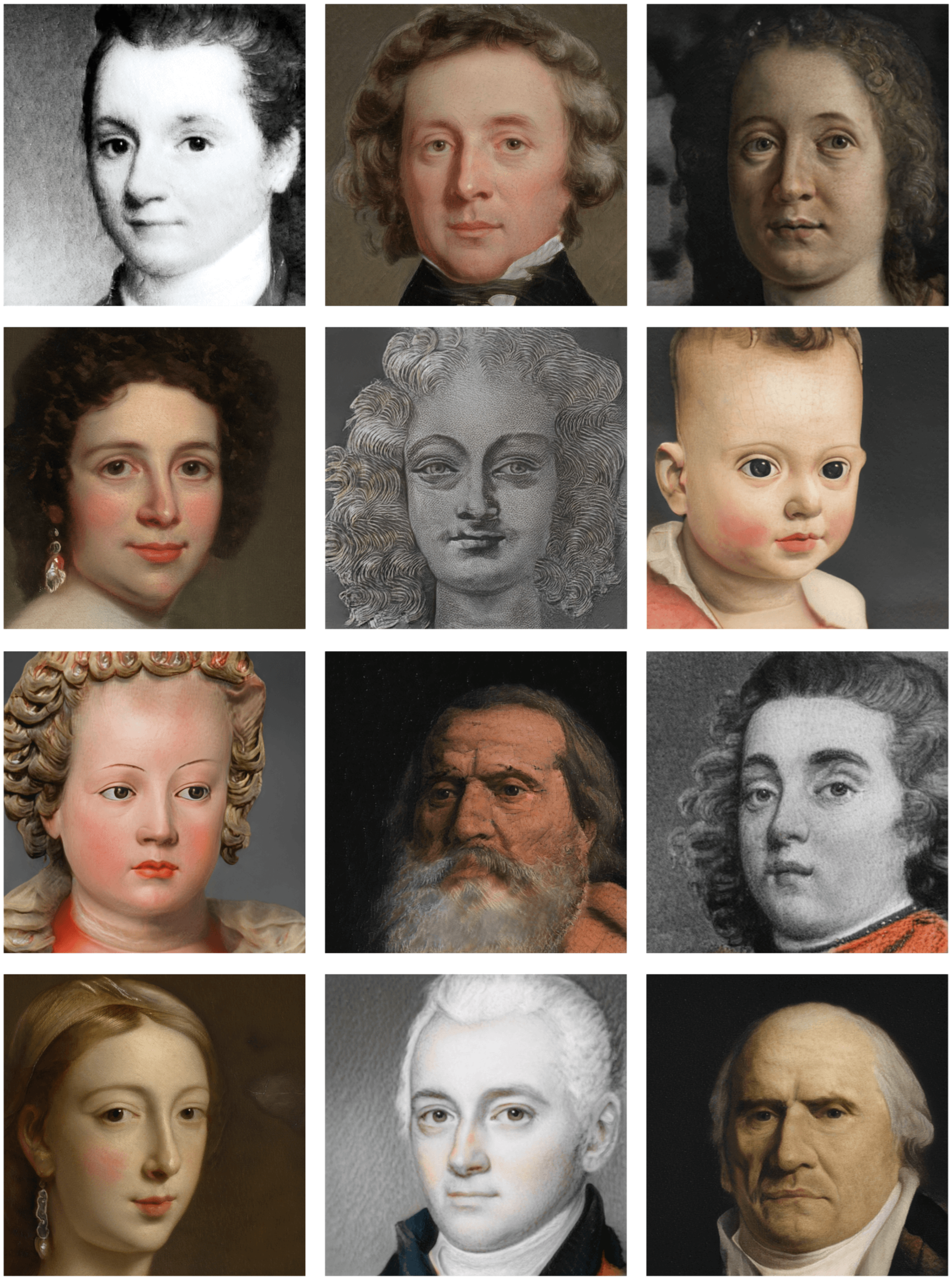

Figure 33. Representative MetFaces images generated by the *Spider* variant of StyleGAN2, trained on AFHQ-Dogs input. The model achieved an FID score of 29.82, which is lower than the FID of the StyleGAN2-ADA baseline (18.75). This is expected, as the AFHQ-Dogs is not a *friendly neighbor* of the target dataset.

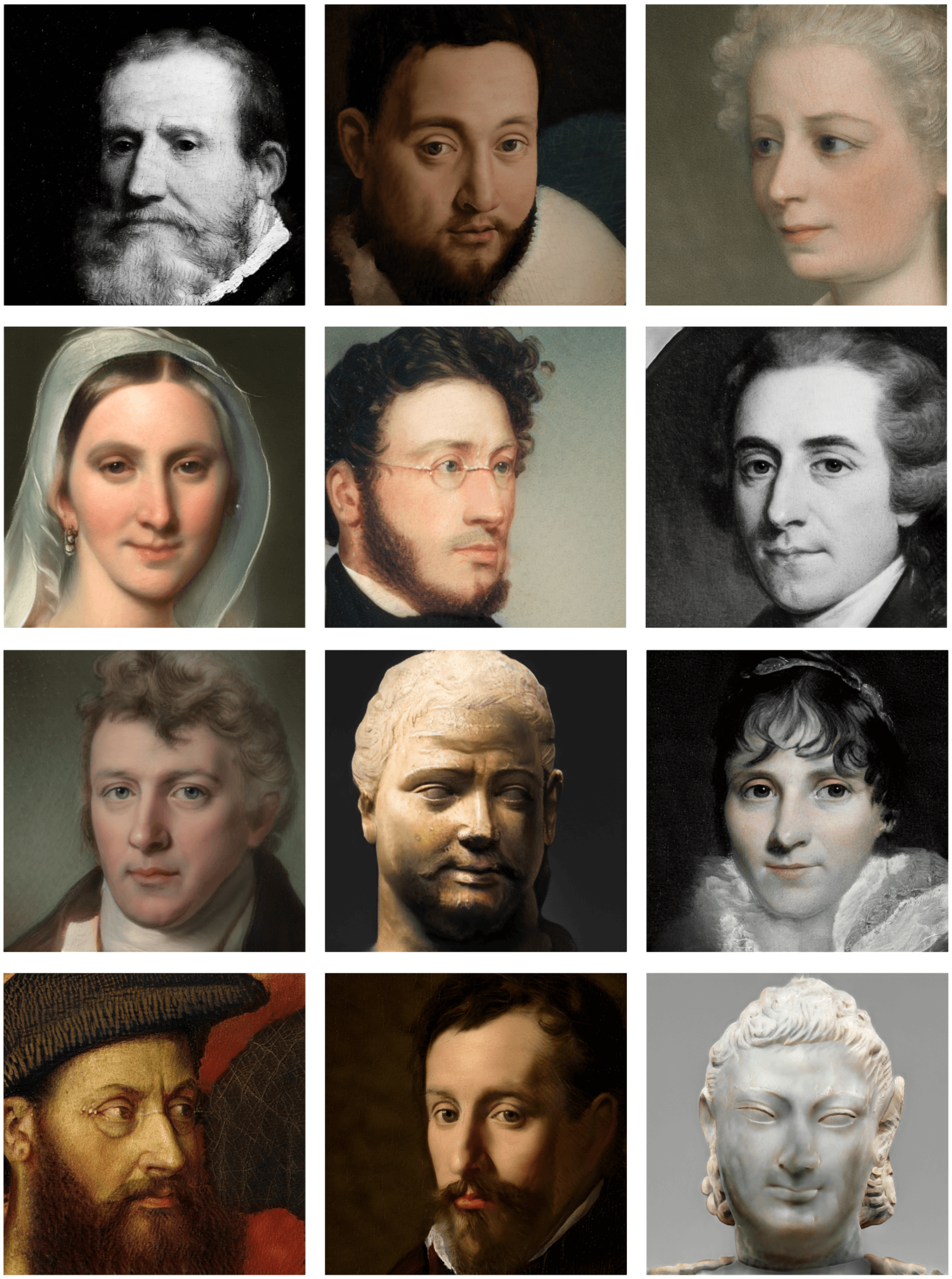

Figure 34. Sample images generated by the *Spider* variant of StyleGAN2, trained on Tiny-ImageNet input and MetFaces as output. The Spider StyleGAN variant achieves state-of-the-art FID of 15.60, against an FID of 18.75 achieved by the StyleGAN2-ADA baseline.

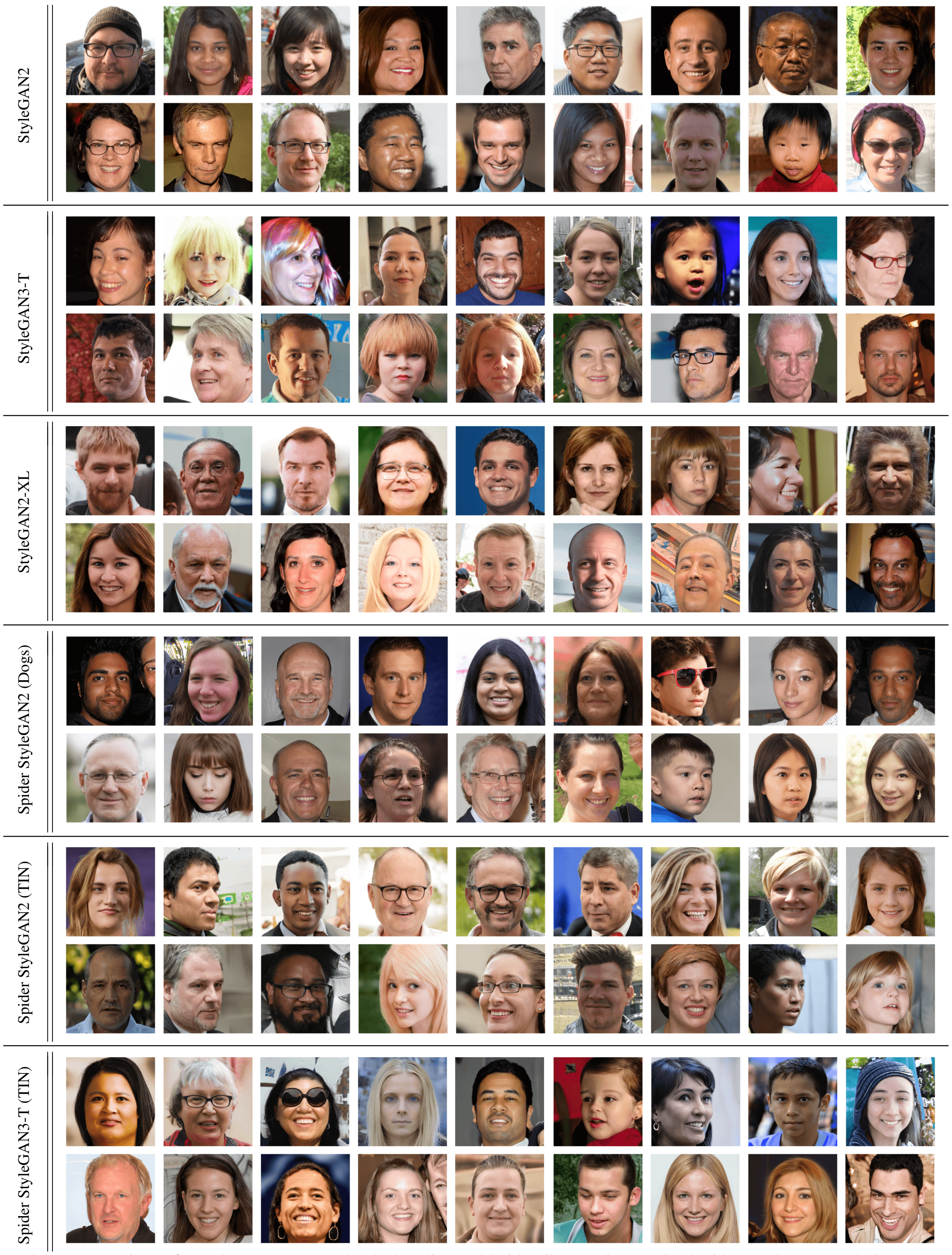

Figure 35. A comparison of FFHQ ages generated by the baseline and Spider GAN variants trained with AFHQ-Dogs and Tiny-ImageNet (TIN) inputs. Spider StyleGAN2-ADA with the Tiny-ImageNet input performs on par with the StyelGAN-XL baseline (FID of 2.45 for the proposed approach versus FID of 2.07 for the baseline), with a mere one-third of the network complexity.

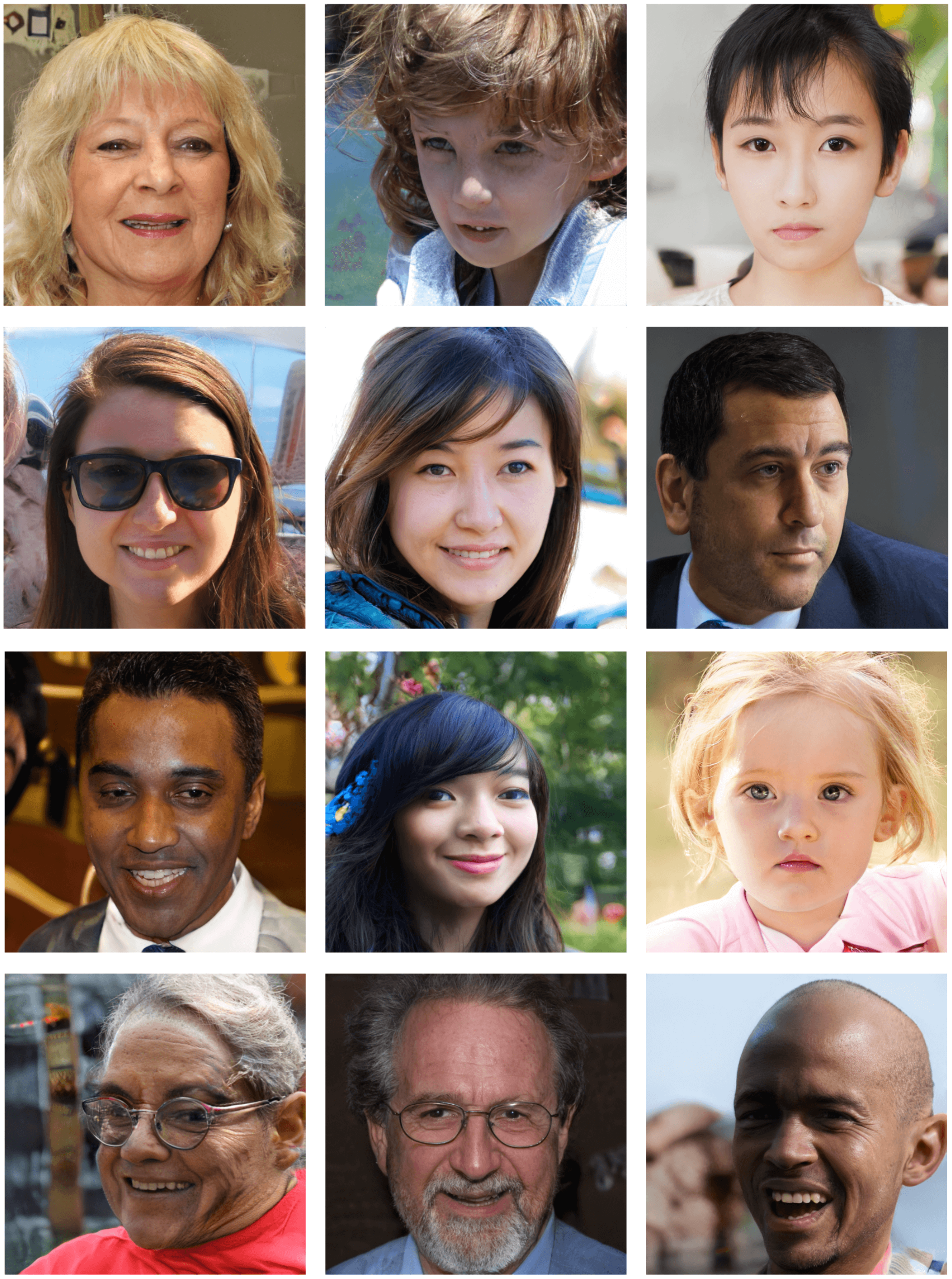

Figure 36. FFHQ images generated by the *Spider* variant of StyleGAN2-ADA, trained on a model incorporating weight transfer from the StyleGAN2-ADA model trained on AFHQ-Dogs. The input samples are drawn from a StyleGAN2-ADA model model pre-trained on 32×32 Tiny-ImageNet images. The converged model achieved an FID of 3.07 as opposed to 2.70 of the baseline model. The lower FID can be attributed to the choice of a *poor neighbor* of the target dataset.

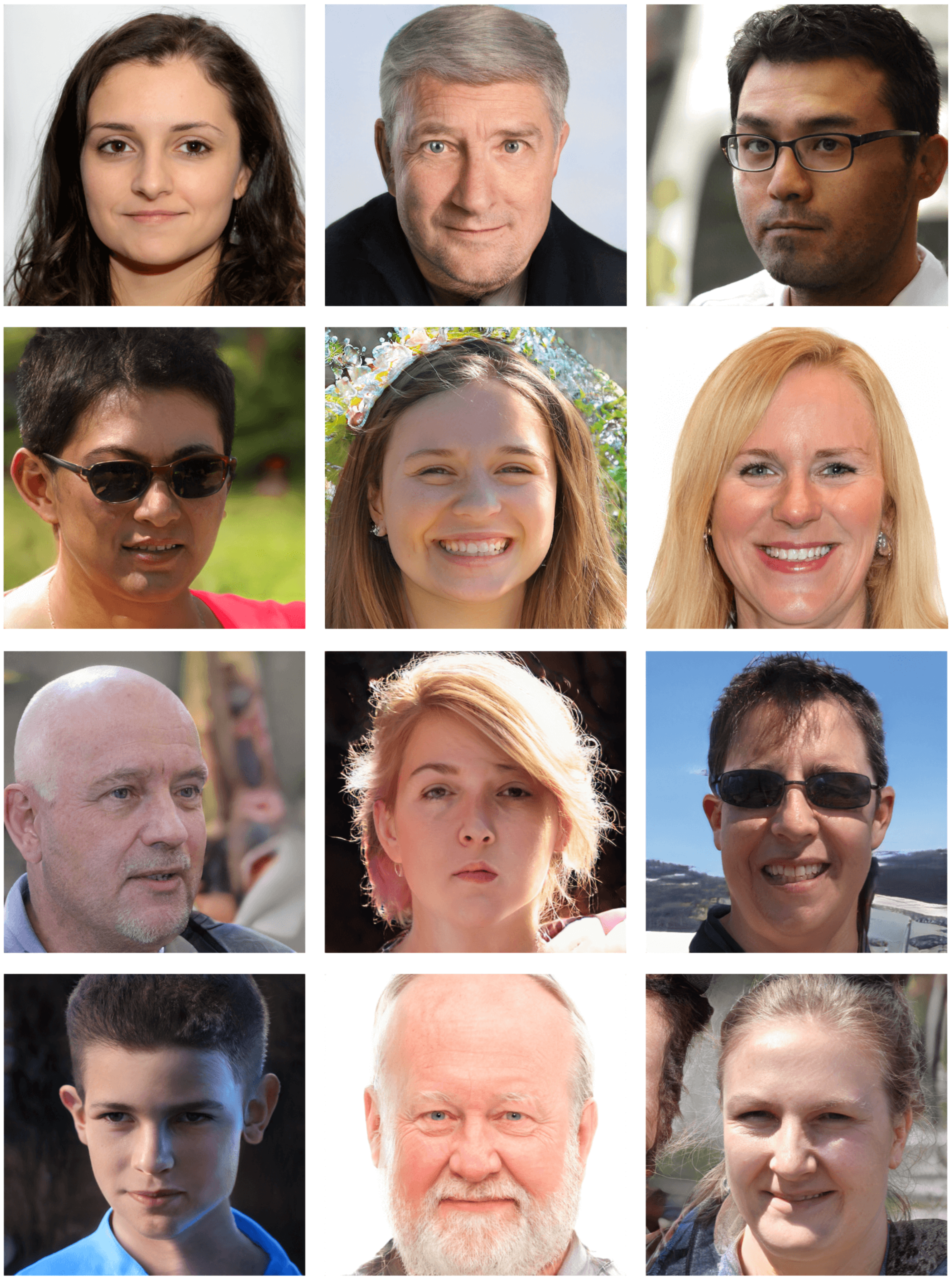

Figure 37. FFHQ images generated by the *Spider* variant of StyleGAN2-ADA, trained on a model incorporating weight transfer from the StyleGAN2-ADA model trained on AFHQ-Dogs images. The model achieves an FID of 2.45, superior to the baseline StyleGAN2-ADA, Polarity-StyleGAN2 and MaGNET-StyleGAN2 (with FID scores of 2.70, 2.57 and 2.66, respectively).

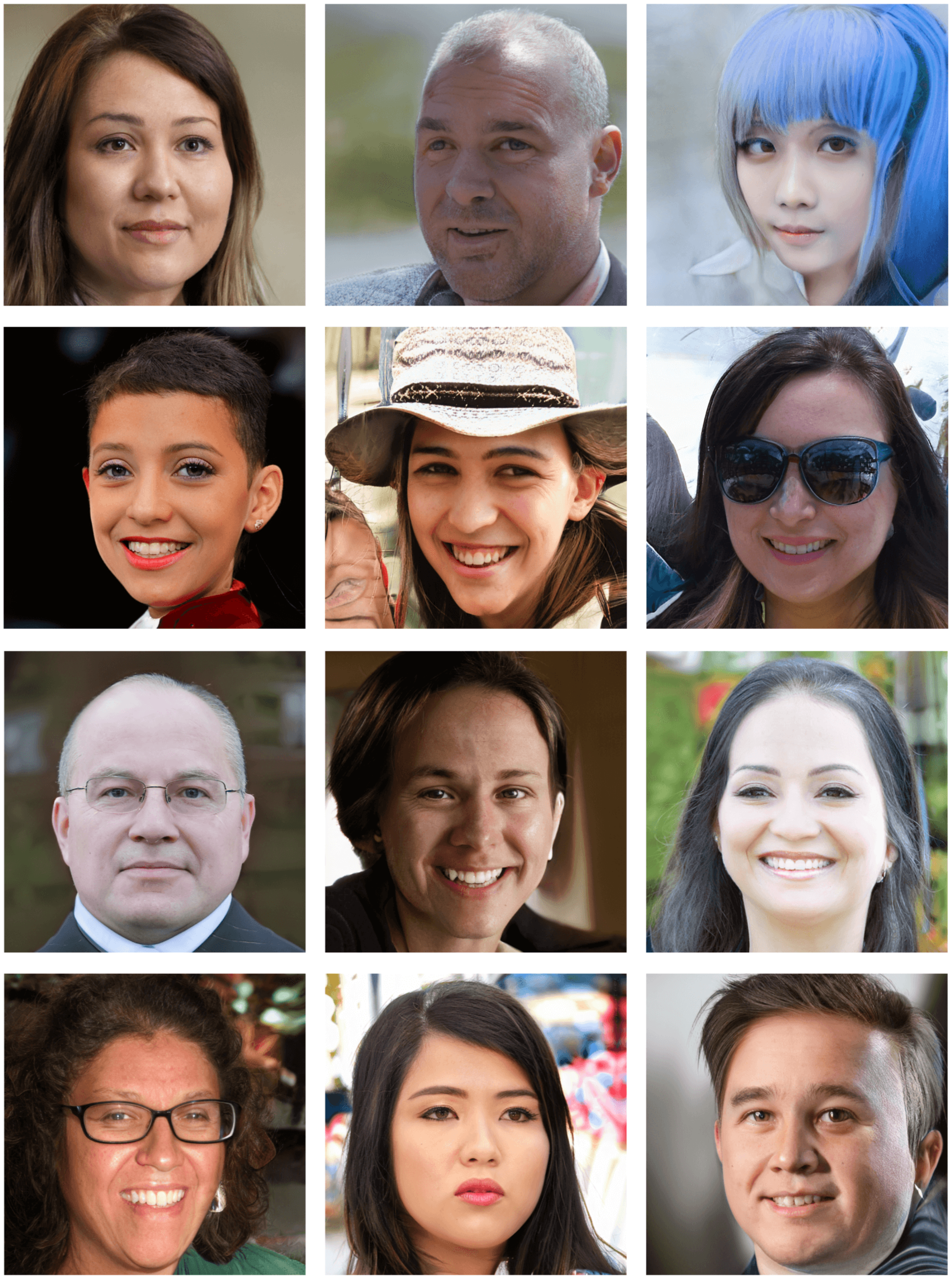

Figure 38. FFHQ images generated by the *Spider* variant of StyleGAN3-T, trained on Tiny-ImageNet dataset. The model achieved an FID of 2.86.

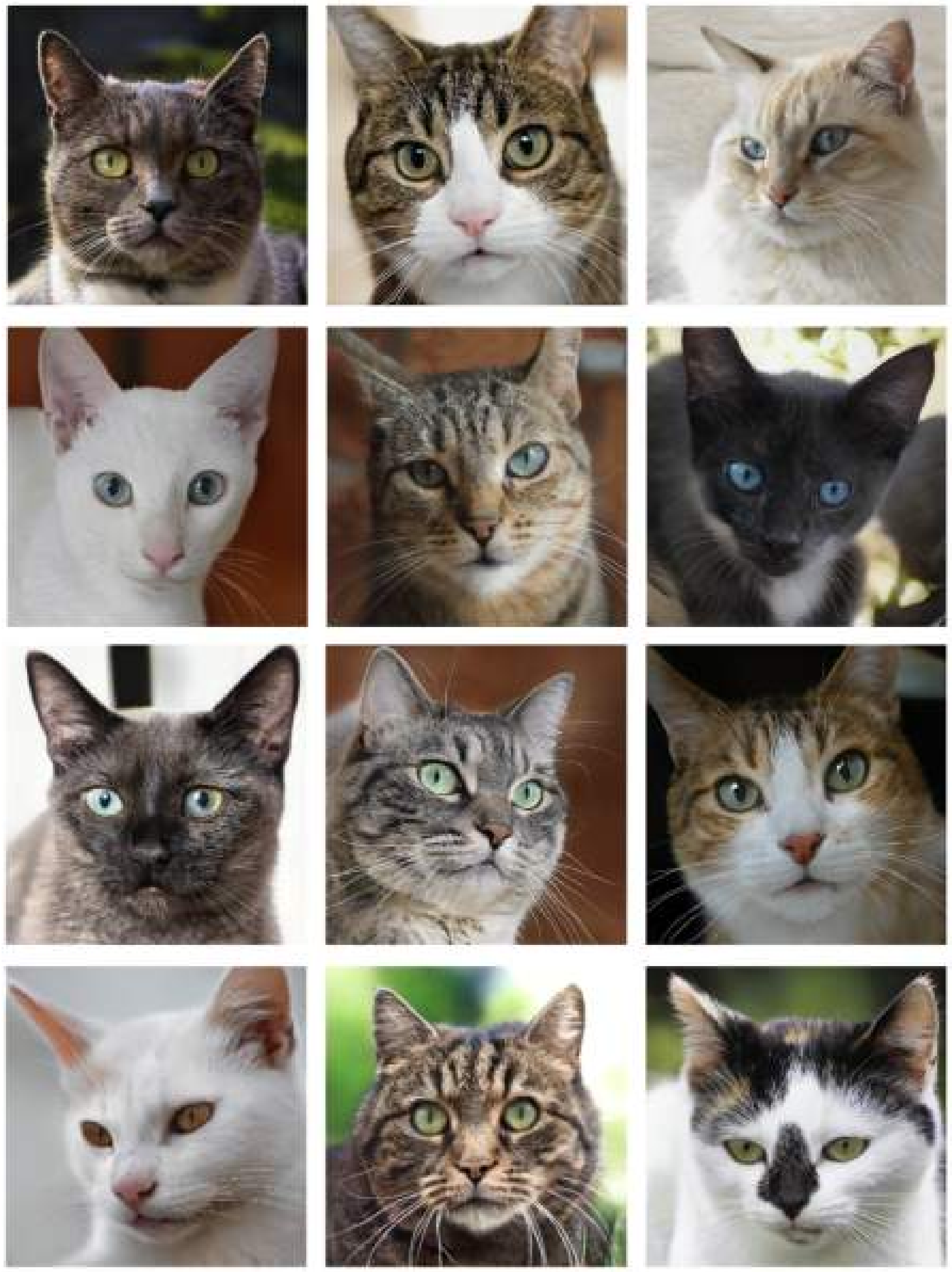

Figure 39. AFHQ-Cat images generated by the *Spider* variant of StyleGAN2-ADA, trained on a model incorporating weight transfer from the StyleGAN2-ADA model trained on AFHQ-Dogs. The input samples are drawn from a StyleGAN2-ADA model model pre-trained on 32×32 Tiny-ImageNet images. The converged model achieves an FID of 3.86 in one-fifth of he training iterations required by the baseline.

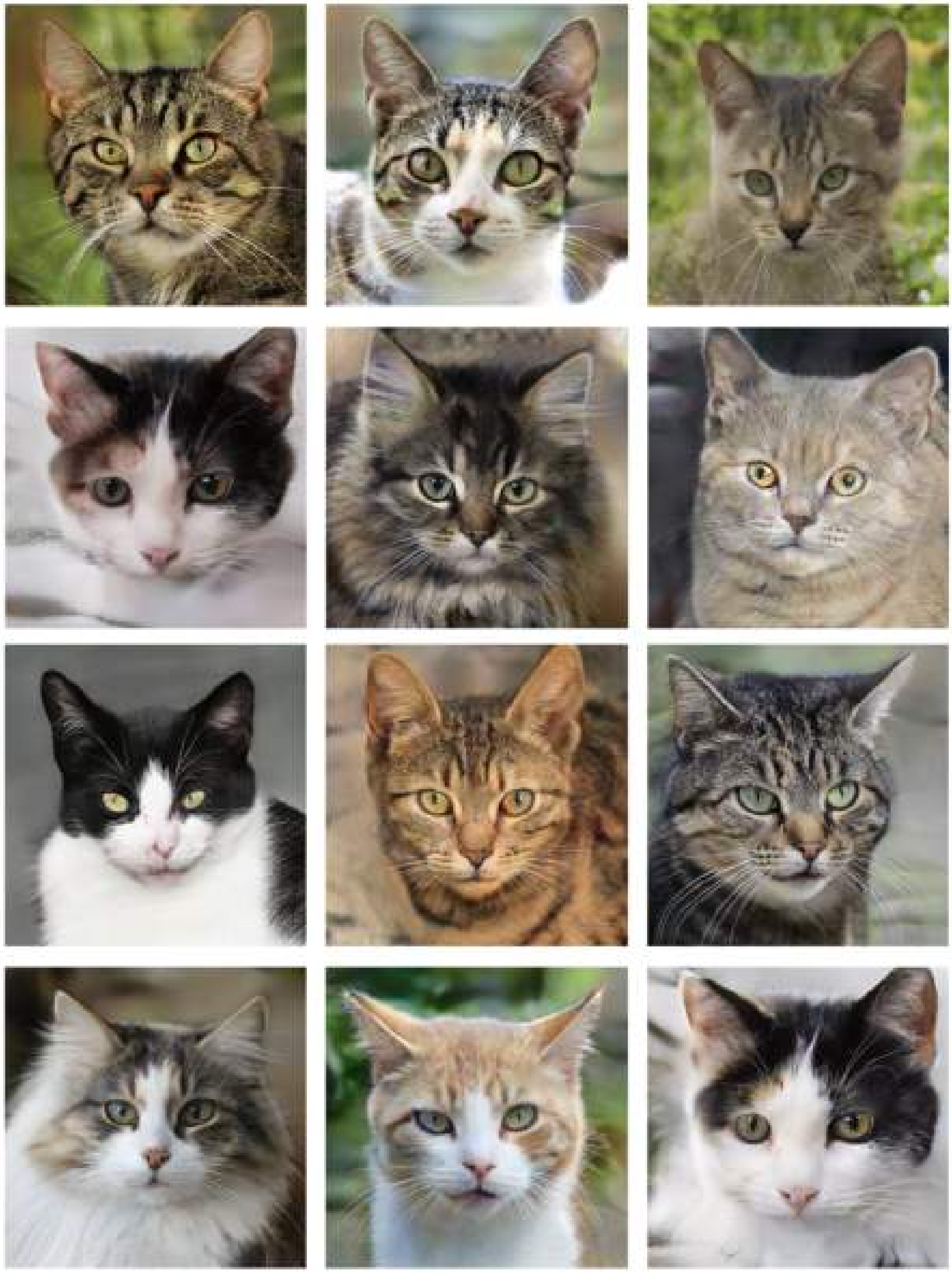

Figure 40. AFHQ-Cat images generated by the *Spider* variant of StyleGAN3-T from scratch. The input samples are drawn from a StyleGAN3-T model model pre-trained on 32×32 AFHQ-Dog images. The converged model achieves an FID of 6.29, which is on par with the baselines, in a mere one-fifth of the suggested [12] training iterations.

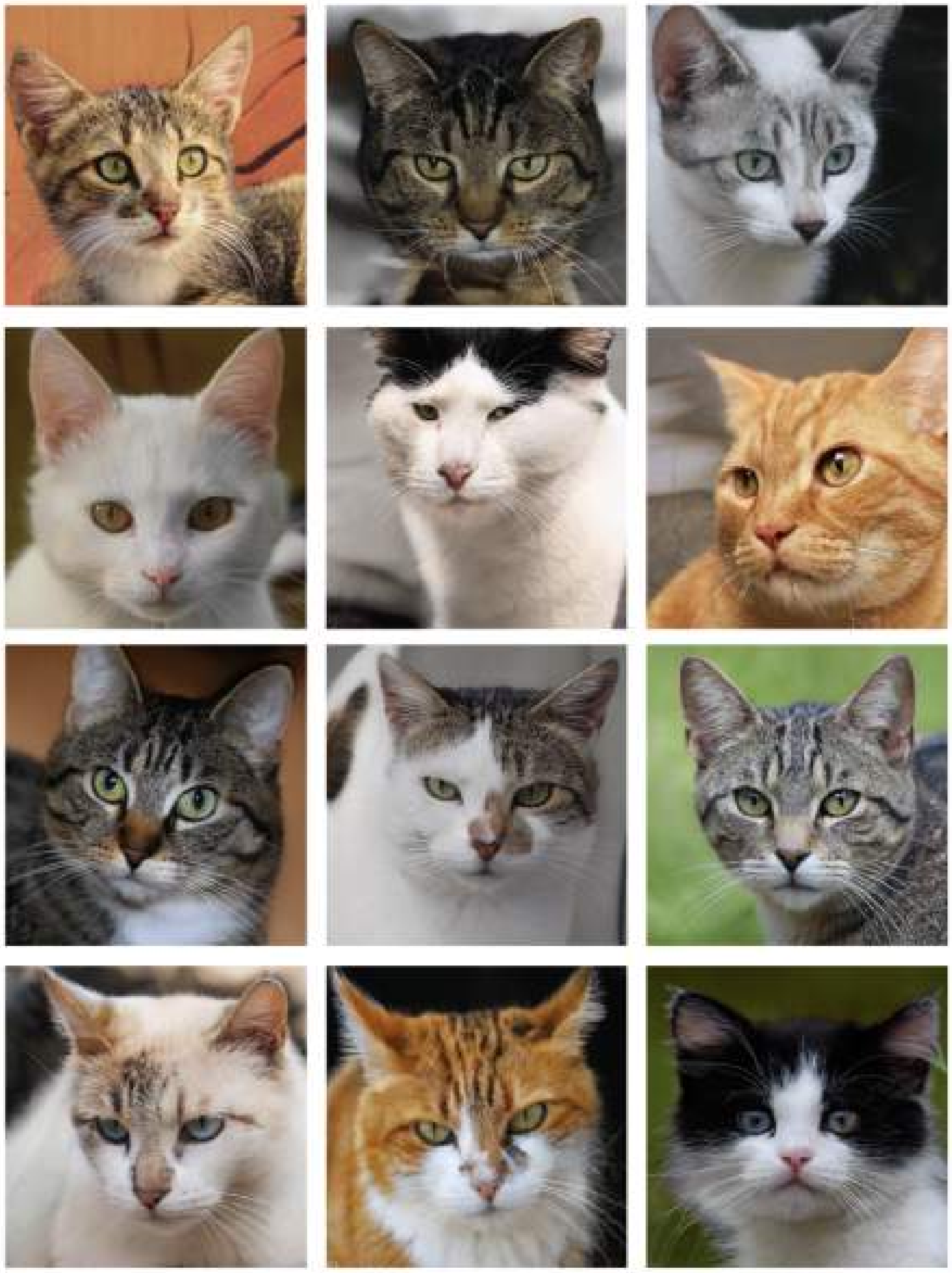

Figure 41. AFHQ-Cat images generated by the *Spider* variant of StyleGAN3-T, trained on a model incorporating weight transfer from the StyleGAN3-T model trained on AFHQv2-Dog. The input samples are drawn from a StyleGAN2-ADA model model pre-trained on 32×32 Tiny-ImageNet images. The converged model achieves a state-of-the-art FID of 3.07 and KID of 0.23×10^{-3} in one-fourth of the training iterations of baseline StyleGAN3 [12].

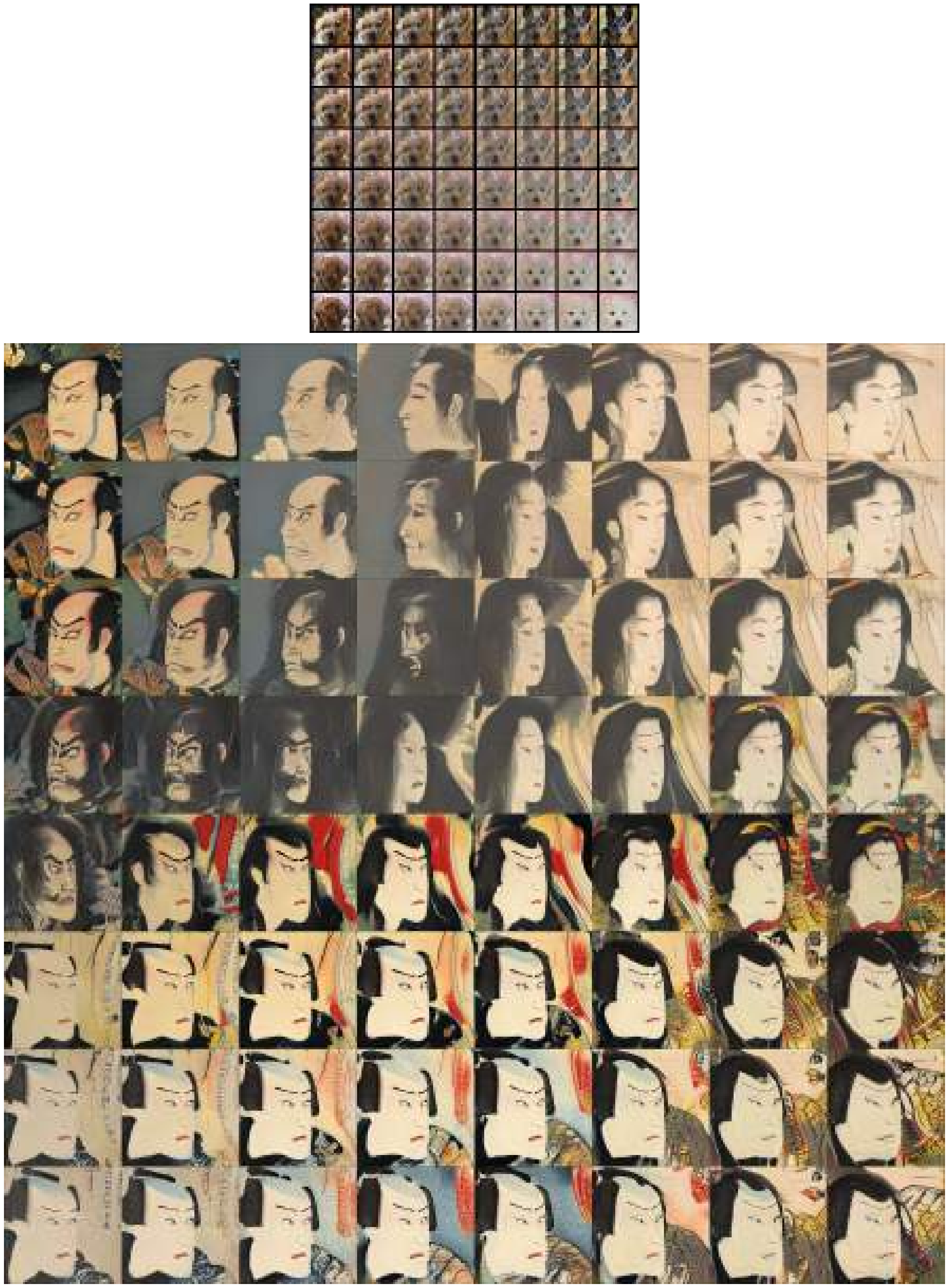

Figure 42. A grid of interpolated Ukiyo-E images generated by Spider StyleGAN2-ADA, trained on AFHQ-Dogs. Images are generated by transforming Gaussian noise to AFHQ-Dogs images via an input-stage model, whose subsequent outputs serve as the input to Spider StyleGAN2-ADA. The interpolation is performed in the AFHQ-Dogs space, and provided as input to Spider StyleGAN2-ADA. We observe smooth transitions between the interpolated images, which allows for fine-grained control of the features.

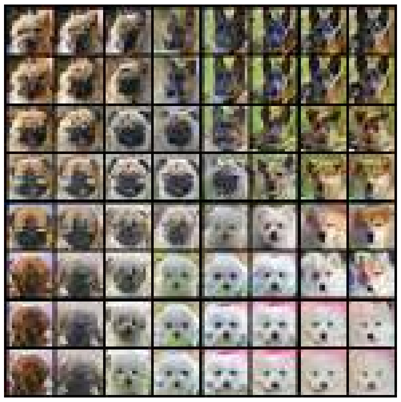

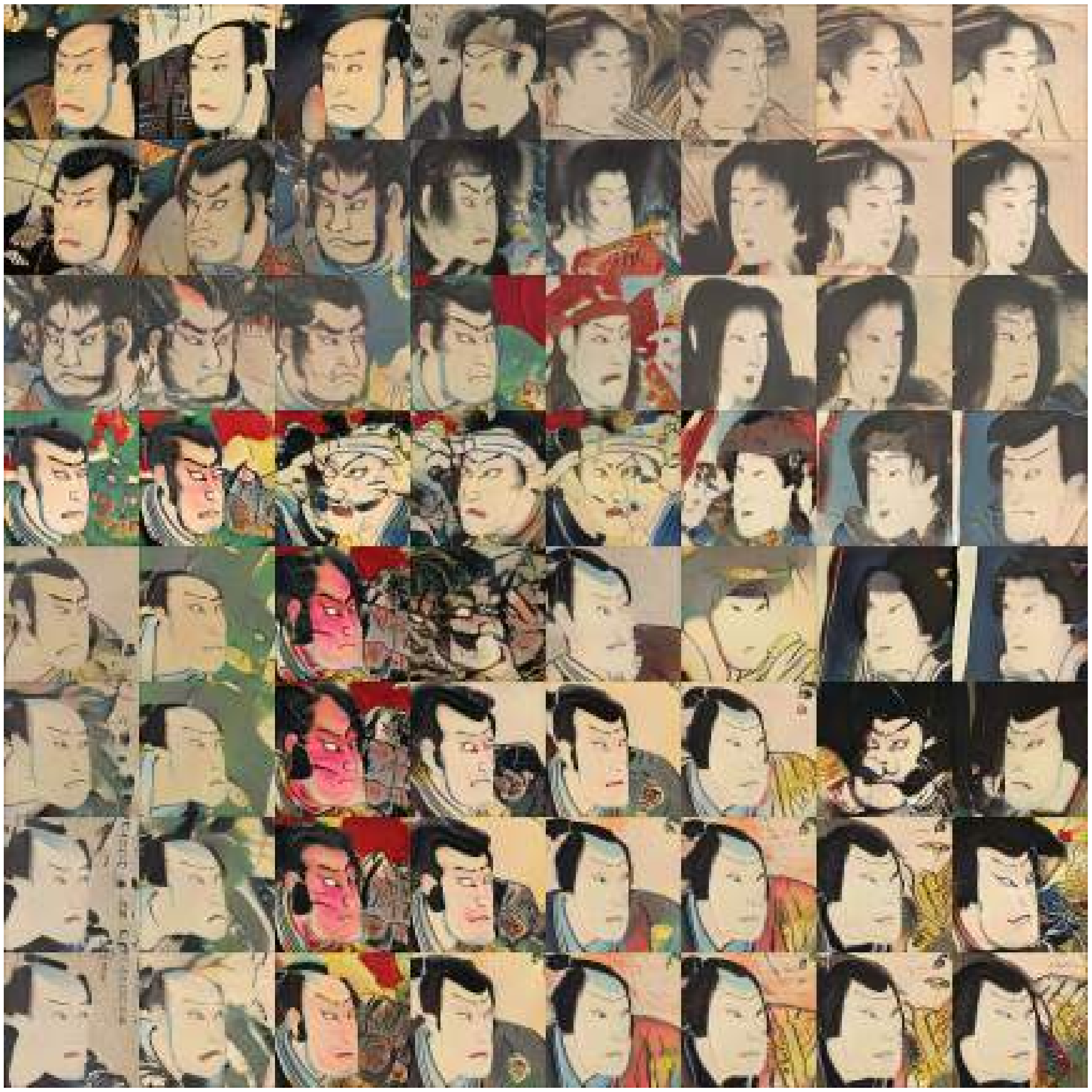

Figure 43. A grid of interpolated Ukiyo-E images generated by the Spider StyleGAN2-ADA, trained on AFHQ-Dogs. Images are generated by transforming Gaussian noise to AFHQ-Dogs images via an input-stage model, whose subsequent outputs serve as the input Spider StyleGAN2-ADA. In this case, the interpolation is performed in the Gaussian space and fed to the input-stage pre-trained StyleGAN. The corresponding AFHQ-Dogs images generated are provided as input to the Spider StyleGAN2-ADA. We observe abrupt and unnatural transitions between images. Some images also appear to be unrealistic, which is not surprising, as the interpolation of points drawn from a Gaussian manifold have an extremely low probability of lying on the manifold.

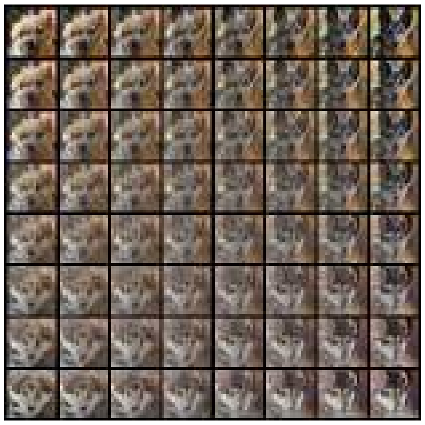

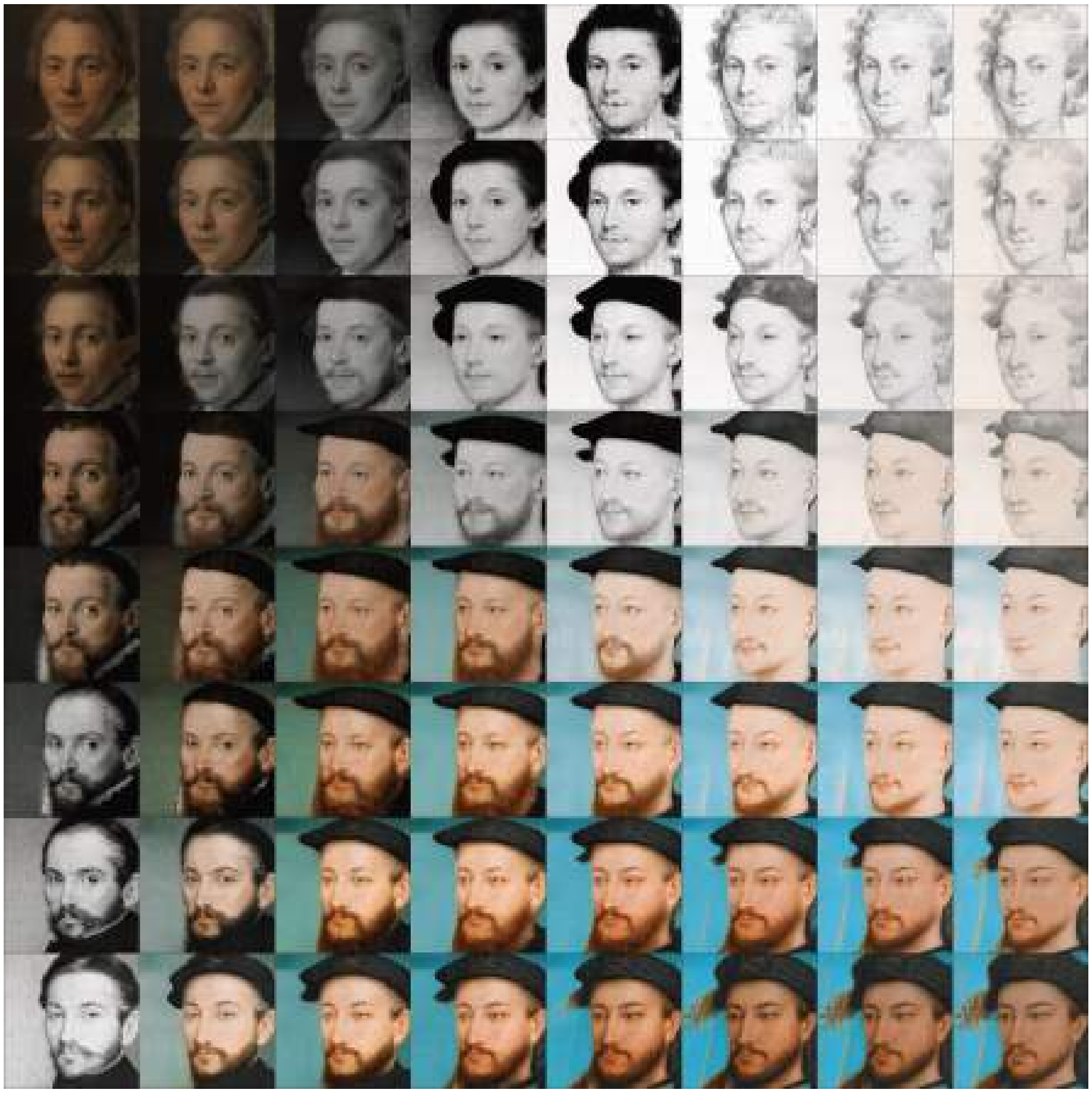

Figure 44. Interpolations on the MetFaces images generated by the Spider StyleGAN2-ADA, trained on AFHQ-Dogs. The inputs to the Spider StyleGAN are linearly interpolated AFHQ-Dogs images. We observe smooth and gradual transitions between the color- and sketch-based images generated by Spider StyleGAN, which is highly desirable for feature manipulation.

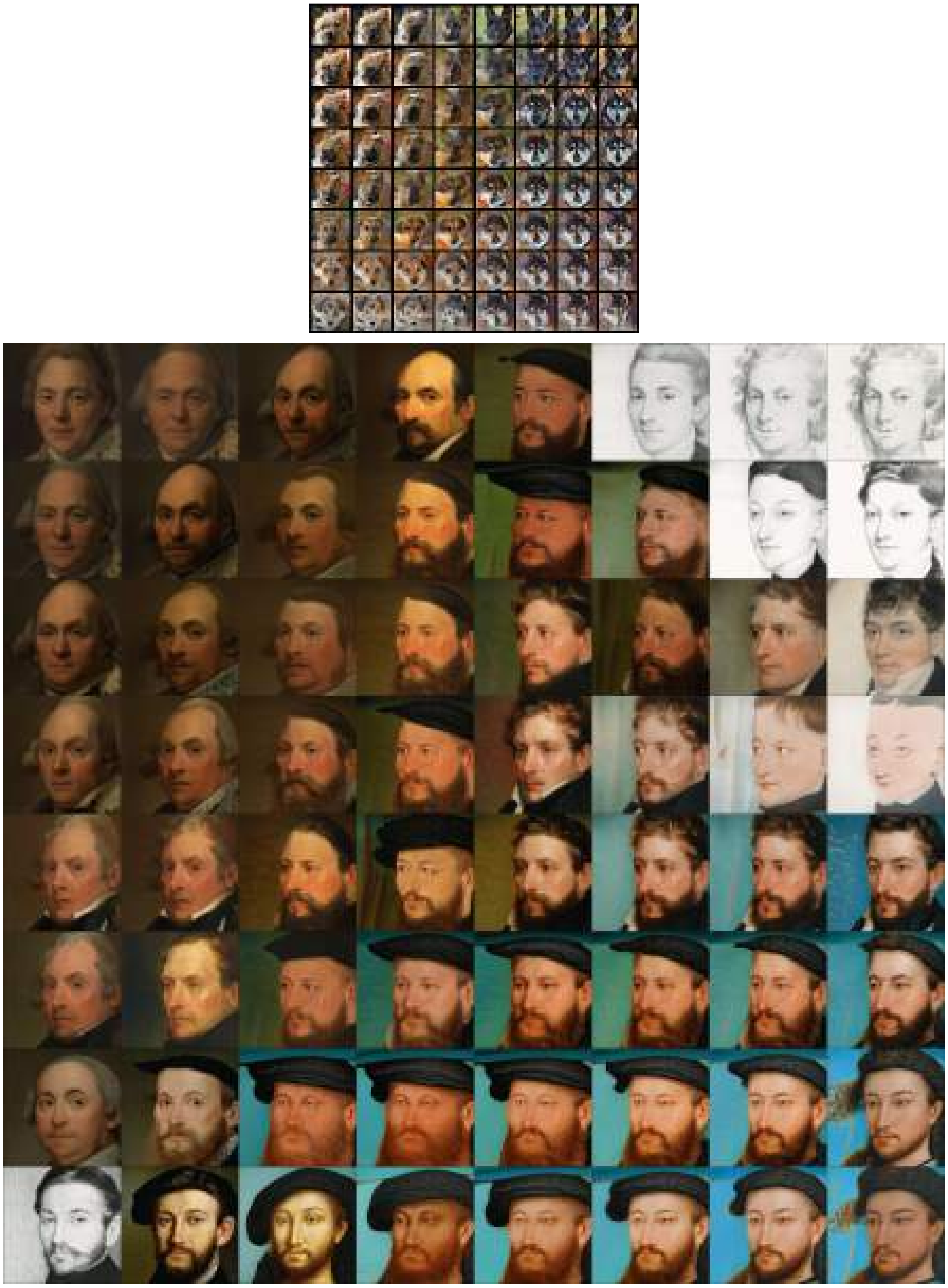

Figure 45. Interpolated MetFaces images generated by the Spider StyleGAN2-ADA, trained on AFHQ-Dogs. The interpolation is carried out in the Gaussian fed to the pre-trained input-stage StyleGAN. The corresponding AFHQ-Dogs images generated are given as input to Spider StyleGAN2-ADA. We observe unnatural and discontinuous transitions between the color and sketch images which can be attributed to the disconnected manifold structure of the dataset.

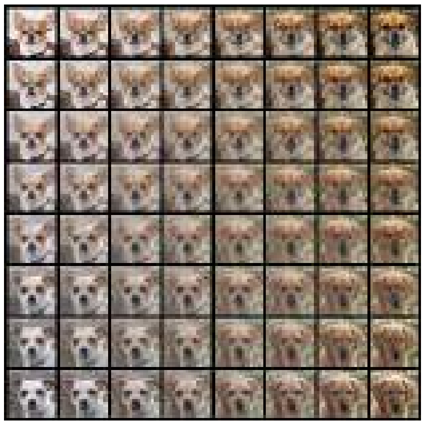

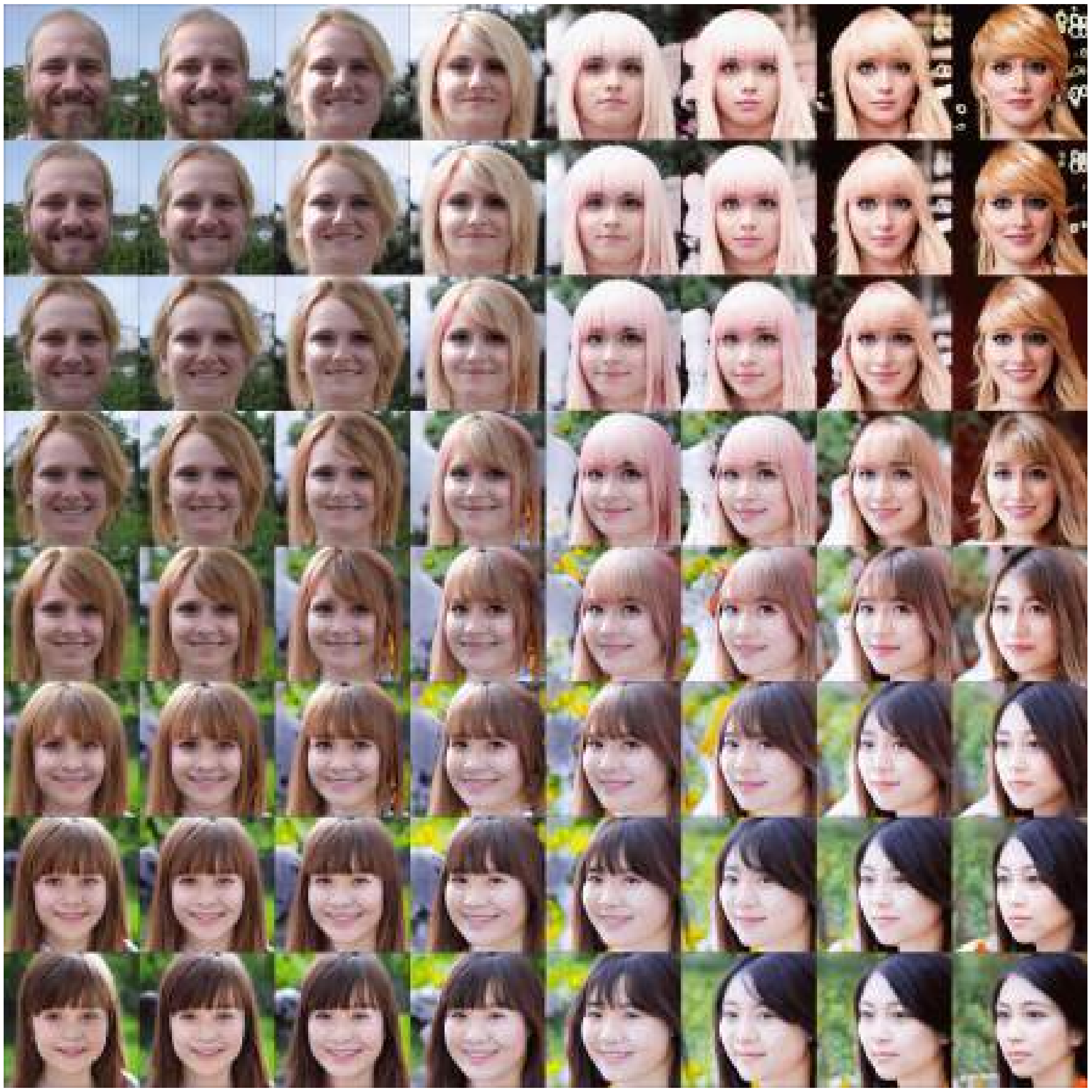

Figure 46. Interpolations on the FFHQ images generated by the Spider StyleGAN2-ADA, trained on AFHQ-Dogs. The inputs to the Spider StyleGAN are linear interpolates computed on the AFHQ-Dogs images. We observe that the proposed Spider variant generates smooth and gradual transitions with fine-grained facial features allowing for superior control of the image generation.

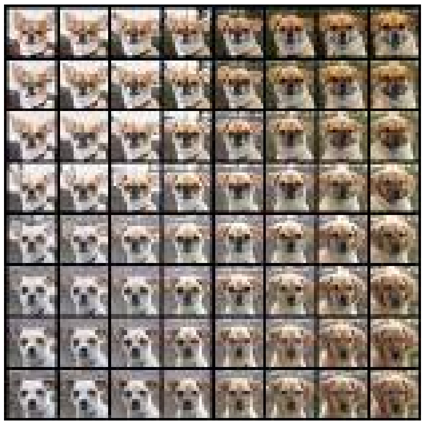
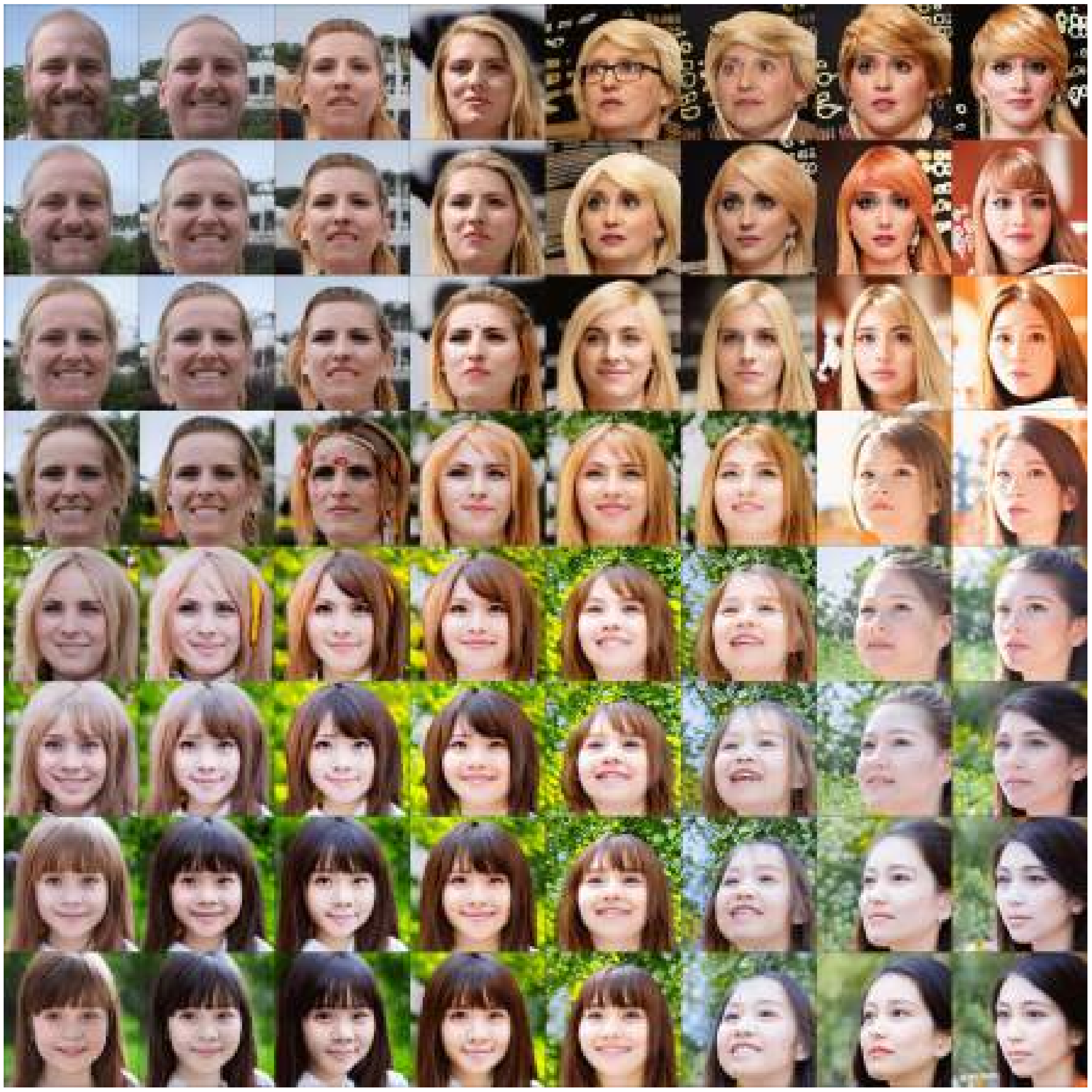

Figure 47. Interpolated FFHQ images generated by the Spider StyleGAN2-ADA, trained on AFHQ-Dogs. Interpolation is performed in the Gaussian space of the input-stage StyleGAN, which generate a set of AFHQ-Dogs images, which in turn serve as the input to the Spider StyleGAN2-ADA. We observe discontinuous transitions in the hair, color, and other features of the generated images. Some images are also noisy, as they correspond to inputs drawn from outside of the training manifold.

E. GitHub Repository and Code Release

The codebase for implementing Spider GAN, Spider PGGAN, Spider StyleGAN and SID has been included as part of the Supplementary. The baseline non-parametric prior [16] was implemented using the publicly released *.mat* file. PGGAN [27] and StyleGAN2 and StyleGAN3 were implemented using publicly available GitHub repositories, with modification included to implement their respective *Spider* variants.

The implementation for CSID$_m$ and SID are based on the Inception features provided by the Clean-FID [10] library. In order to maintain uniformity, SID can also be computed by providing the path to existing source and target image folders, akin to FID and KID.

An implementation of SID atop the Clean-FID [10] backbone, with associated animations of the experiments presented in this manuscript are available at `https://github.com/DarthSid95/clean-sid`. The TensorFlow-based source code for Spider GANs built atop the DCGAN architecture, and associated pre-trained models are available at `https://github.com/DarthSid95/SpiderDCGAN`. The PyTorch-based source code for implementing the *Spider* variants of PGGAN, StyleGAN2, StyleGAN2-ADA and StyleGAN3, with the corresponding pre-trained models are available at `https://github.com/DarthSid95/SpiderStyleGAN.` Images in the *Main Manuscript* and *Supplementary Document* have been compressed to meet the file-size limits of the venue. The GitHub repositories also include the full-resolution versions of the images provided in the *Main Manuscript* and *Supporting Document*.

References

[1] F. Camastra and A. Staiano, “Intrinsic dimension estimation: Advances and open problems,” *Information Sciences*, vol. 328, pp. 26–41, 2016.

[2] M. Hein and J.-Y. Audibert, “Intrinsic dimensionality estimation of submanifolds in R^d,” in *Proceedings of the 22nd International Conference on Machine Learning*, pp. 289–296, 2005.

[3] E. Facco, M. d’Errico, A. Rodriguez, and A. Laio, “Estimating the intrinsic dimension of datasets by a minimal neighborhood information,” *Scientific Reports*, vol. 7, Sep. 2017.

[4] P. Campadelli, E. Casiraghi, C. Ceruti, and A. Rozza, “Intrinsic dimension estimation: Relevant techniques and a benchmark framework,” *Mathematical Problems in Engineering*, vol. 2015, pp. 1–21, 10 2015.

[5] C. Davis and W. M. Kahan, “The rotation of eigenvectors by a perturbation. iii,” *SIAM Journal on Numerical Analysis*, vol. 7, no. 1, pp. 1–46, 1970.

[6] Y. Yu, T. Wang, and R. J. Samworth, “A useful variant of the Davis—Kahan theorem for statisticians,” *Biometrika*, vol. 102, no. 2, pp. 315–323, 2015.

[7] T. Liang, “How well generative adversarial networks learn distributions,” *Journal of Machine Learning Research*, vol. 22, no. 228, pp. 1–41, 2021.

[8] N. Schreuder, V.-E. Brunel, and A. Dalalyan, “Statistical guarantees for generative models without domination,” in *Proceedings of the 32nd International Conference on Algorithmic Learning Theory*, vol. 132, pp. 1051–1071, Mar 2021.

[9] A. Block, Z. Jia, Y. Polyanskiy, and A. Rakhlin, “Intrinsic dimension estimation,” 2021.

[10] G. Parmar, R. Zhang, and J.-Y. Zhu, “On buggy resizing libraries and surprising subtleties in FID calculation,” *arXiv preprint, arXiv:2104.11222*, vol. abs/2104.11222, April 2021.

[11] T. Karras, M. Aittala, J. Hellsten, S. Laine, J. Lehtinen, and T. Aila, “Training generative adversarial networks with limited data,” in *Advances in Neural Information Processing Systems 33*, 2020.

[12] T. Karras, M. Aittala, S. Laine, E. Härkönen, J. Hellsten, J. Lehtinen, and T. Aila, “Alias-free generative adversarial networks,” in *Advances in Neural Information Processing Systems*, June 2021.

[13] M. Khayatkhoei, M. K. Singh, and A. Elgammal, “Disconnected manifold learning for generative adversarial networks,” in *Advances in Neural Information Processing Systems 31*, pp. 7343–7353, 2018.

[14] A. Radford, L. Metz, and S. Chintala, “Unsupervised representation learning with deep convolutional generative adversarial networks,” in *Proceedings of the 4th International Conference on Learning Representations*, 2016.

[15] Y. Kilcher, A. Lucchi, and T. Hofmann, “Semantic interpolation in implicit models,” in *Proceedings of the 6th International Conference on Learning Representations*, 2018.

[16] R. Singh, P. Turaga, S. Jayasuriya, R. Garg, and M. Braun, “Non-parametric priors for generative adversarial networks,” in *Proceedings of the 36th International Conference on Machine Learning*, vol. 97, pp. 5838–5847, June 2019.

[17] M. Arjovsky, S. Chintala, and L. Bottou, "Wasserstein generative adversarial networks," in *Proceedings of the 34th International Conference on Machine Learning*, pp. 214–223, 2017.

[18] L. Mescheder, A. Geiger, and S. Nowozin, "Which training methods for GANs do actually converge?," in *Proceedings of the 35th International Conference on Machine Learning*, vol. 80, pp. 3481–3490, 2018.

[19] D. P. Kingma and J. Ba, "Adam: A method for stochastic optimization," in *Proceedings of the 3rd International Conference on Learning Representations*, 2015.

[20] M. Abadi *et al.*, "TensorFlow: Large-scale machine learning on heterogeneous distributed systems," *arXiv preprint, arXiv:1603.04467*, Mar. 2016.

[21] A. Paszke *et al.*, "PyTorch: An imperative style, high-performance deep learning library," in *Advances in Neural Information Processing Systems 32*, vol. 32, 2019.

[22] M. Heusel, H. Ramsauer, T. Unterthiner, B. Nessler, and S. Hochreiter, "GANs trained by a two time-scale update rule converge to a local Nash equilibrium," *arXiv preprints, arXiv:1706.08500*, 2018.

[23] C. Szegedy, V. Vanhoucke, S. Ioffe, J. Shlens, and Z. Wojna, "Rethinking the inception architecture for computer vision," *arXiv preprint, arXiv:1512.00567*, Dec. 2015.

[24] J. Deng, W. Dong, R. Socher, L.-J. Li, K. Li, and L. Fei-Fei, "ImageNet: A large-scale hierarchical image database," in *Proceedings of the IEEE/CVF Conference on Computer Vision and Pattern Recognition*, 2009.

[25] M. Bińkowski, D. J. Sutherland, M. Arbel, and A. Gretton, "Demystifying MMD GANs," in *Proceedings of the 6th International Conference on Learning Representations*, 2018.

[26] I. O. Tolstikhin, O. Bousquet, S. Gelly, and B. Schölkopf, "Wasserstein auto-encoders," in *Proceedings of the 6th International Conference on Learning Representations*, 2018.

[27] T. Karras, T. Aila, S. Laine, and J. Lehtinen, "Progressive growing of GANs for improved quality, stability, and variation," in *Proceedings of the 6th International Conference on Learning Representations*, 2018.

[28] P. Esser, R. Rombach, and B. Ommer, "Taming transformers for high-resolution image synthesis," in *Proceedings of the IEEE/CVF Conference on Computer Vision and Pattern Recognition (CVPR)*, June 2021.

[29] J. Yu, X. Li, J. Y. Koh, H. Zhang, R. Pang, J. Qin, A. Ku, Y. Xu, J. Baldridge, and Y. Wu, "Vector-quantized image modeling with improved VQGAN," in *Proceedings of the 10th International Conference on Learning Representations*, 2022.

[30] A. Brock, J. Donahue, and K. Simonyan, "Large scale GAN training for high fidelity natural image synthesis," *arXiv preprints, arXiv:1809.11096*, Sep. 2018.

[31] M. Kang, W. Shim, M. Cho, and J. Park, "Rebooting ACGAN: Auxiliary classifier GANs with stable training," in *Advances in Neural Information Processing Systems 34*, 2021.

[32] P. Zhong, Y. Mo, C. Xiao, P. Chen, and C. Zheng, "Rethinking generative mode coverage: A pointwise guaranteed approach," in *Advances in Neural Information Processing Systems*, 2019.

[33] I. O. Tolstikhin, S. Gelly, O. Bousquet, C.-J. Simon-Gabriel, and B. Schölkopf, "AdaGAN: boosting generative models," in *Advances in Neural Information Processing Systems*, 2017.

[34] X. Chen, Y. Duan, R. Houthooft, J. Schulman, I. Sutskever, and P. Abbeel, "InfoGAN: Interpretable representation learning by information maximizing generative adversarial nets," in *Advances in Neural Information Processing Systems 29*, pp. 2180–2188, 2016.

[35] A. Odena, C. Olah, and J. Shlens, "Conditional image synthesis with auxiliary classifier GANs," in *Proceedings of the 34th International Conference on Machine Learning (ICML)*, 2017.

[36] A. Sauer, K. Schwarz, and A. Geiger, "StyleGAN-XL: Scaling StyleGAN to large diverse datasets," *arXiv.org*, vol. abs/2201.00273, 2022.